UNIVERSIDAD DEL PAÍS VASCO
EUSKAL HERRIKO UNIBERSITATEA

PHD THESIS

Exploring the Frontiers of Ferromagnetic Insulator/Superconductor-Based Devices: Surface Science Developments to explain Mesoscopic Properties

---

Carmen González Orellana

Supervised by:
Dr. Maxim Ilin and **Dr. Celia Rogero**

May 2023

A mis padres

Contents

Agradecimientos

Diría que, sin duda, esta es la parte de la Tesis que más me ha costado resumir, porque me sobran las palabras de agradecimiento hacia todos vosotros. Sois muchísimos los que habéis contribuido de manera directa o indirecta a esta Tesis. Tened por seguro que, diga lo que diga, me habré quedado corta dándoos las gracias. Espero que entendáis que es porque estoy tan emocionada que ya ni siquiera soy capaz de leer la pantalla.

En primer lugar, y como no podía ser de otra forma, quería dar las gracias a mis directores: Max y Celia, por darme la oportunidad de hacer el doctorado con vosotros, en un entorno tan enriquecedor y en el que he crecido tanto, no solo científicamente, sino también como persona. Gracias Max por estar mano a mano conmigo en el labo. Por no dudar en remangarte para ayudarme siempre que lo he necesitado, por tomarte tu tiempo para explicarme las cosas y por enseñarme tanta ciencia. Gracias también por añadir risas a los *bake-outs*, reparaciones y turnos de noche en los beamtimes. Tengo que hacer también una mención especial a tus soluciones locas siempre que falla cualquier cosa en el laboratorio; creo que, gracias a lo que he aprendido de ti, podría ser electricista, fontanera o mecánica. Celia, gracias por ser la parte menos visible, pero tan necesaria. Por velar para que todo salga bien, por estar en mil cosas y no descuidar ninguna. Gracias sobre todo por esta última etapa, vaya currazo te has pegado con las correcciones que, aunque me han roto los esquemas en muchas ocasiones, me han ayudado muchísimo. Te agradezco mucho tu empatía cada vez que te he contado que estaba agobiada (que no han sido pocas veces), me he sentido muy respaldada y comprendida. Gracias también por abrirme las puertas de tu soci y presentarme a tanta gente, entre los que destaco a Mole y Txiki.

A todas las personas que han pasado por el labo, con los que las horas se han hecho mucho más cortas. A Pablo, por todo el tiempo que hemos compartido en el laboratorio, sobre todo arreglando cosas. Gracias por no perder nunca la sonrisa ni la paciencia. To Sebastien, I have enjoyed our discussions and for sure the time we have shared during your visits. We have built such a nice team. A David y Samuel, que han sido un soplo de aire fresco en el laboratorio. Espero haberos allanado aunque sea un poquito el camino y que este "librito" os sirva de ayuda en vuestra tesis.

Gracias en general a todo el grupo de Nanophysics Lab: Kike, Martina, Khadisha, Rubén, Dimas, Amitayush, Andrew, Laura, Paula, Alejandro, Rodrigo y muchos más, por estar disponibles para echarme un cable cuando me hacía falta.

Muchísimas gracias también a Sebas, por tu entusiasmo y tu sabiduría. Nunca olvidaré tu alegría y emoción cuando funcionaron las primeras muestras de Superted. Gracias también a Mikel y Alberto, por darme el punto de vista teórico que he necesitado en varias ocasiones.

To all the people in superted project: working with you has been such a nice pleasure. Meeting people with the same interests and different approaches has been a super rewarding experience. I have to specially thank Elia, Maria and Francesco, for greeting me in Pisa and guiding me with the tunneling measurements. Grazie mille for the fruitful discussions that made me understand better the results. And also I appreciate the nice lunches that we have shared in Ristoro Pisano and the afterwork aperitivi.

Gracias Marco por ayudarme con las medidas de las barreras y por los beamtimes que hemos compartido, siempre con tanta paciencia y dulzura, da gusto trabajar contigo.

Thanks to Mihail Ipatov, for the countless measurements you have performed in my samples. An important part of the results comes from the analysis of the VSM and ac-susceptibility data.

A Nacho Pascual, gracias por acogerme con los brazos abiertos en tu grupo siempre que me ha hecho falta, me has hecho sentir una más de tu equipo. Por los ratos que hemos compartido también en la soci, por tu sentido del humor y tu cercanía. A los chicos de su grupo: Javi, Andrea, Stefano y Jon, ha sido un gusto trabajar con vosotros, os deseo que todo os vaya genial. Special thanks to Djuro, who I started the 2D-TMDH project with. You have taught so much about STM. And, for sure, thanks for the time we have shared during the beamtimes. Grazie mille to Danilo, for the discussions we have had about the molecules.

A Fèlix Casanova, Sara, Montse, Juanma y Witold, he aprendido mucho colaborando con vosotros.

Le agradezco mucho a la gente del ALBA todo lo que he aprendido con ellos. A Pierluigi por tus muchísimos consejos durante los beamtimes en BOREAS, siempre dispuesto a aconsejar, discutir los datos y ayudarnos cuando algo no iba bien. A todos los de CIRCE, con los que pasé tres meses muy fructíferos. A Michael, Jordi, Carlos, Nacho, Anna y, en especial, a Lucía. Gracias por preocuparos por mi experimento, por enseñarme desde cero ese microscopio tan lleno de lentes, y por todo lo que disfruté comiendo y charlando con vosotros al solecito en la terraza cada día.

Gracias Dani M. Tong por ayudarme con las medidas de AFM, explicarme la técnica con tanto detalle y tomarte tu tiempo para que lo comprendiera todo. Espero no haberte dado mucho la lata.

Gracias a todas las personas que hacen que trabajar en el CFM sea más fácil: Marta, Ane, Mari Jose, Joanes, Aitor y Gotzon, entre otros. Gracias Idoia por todas las actividades que organizas para acercar la ciencia a la gente, son muy necesarias y las he disfrutado mucho. Y muchísimas gracias a Juan, eres imprescindible en este centro, no solo por tu buen saber hacer, sino por tu carisma y tu entrega.

Y, por supuesto, infinitas gracias a los amigos que me brindó esta aventura. Habéis hecho que me sienta siempre muy respaldada y bien rodeada. Cuantísimos recuerdos me llevo de estos años. Carlitos, mi hermano, gracias por preocuparte siempre por mí y por hacerme sentir que soy una prioridad en tu apretada agenda. A Fer, tu increíble sentido del humor y el corazoncito que se esconde debajo me dan la vida. Qué suerte que siempre te sienta cerca, ya sea en la habitación de al lado o a miles de kilómetros. Eres la Sonia de mi Selena. Migui, mi bebesito, nuestra complicidad es increíble. Gracias por enseñarme con tu ejemplo que ningún problema es demasiado grande como para hacernos sentir pequeños. Marina, mi compi de todo. Gracias por todas las penas y alegrías que hemos compartido. Ya estoy guardando energías para celebrar tu tesis por todo lo alto. Rosel, qué suerte el día que apareciste para ver el piso, estos años sin ti no habrían sido ↑↑↑. Gracias por estar para lo bueno y lo malo, y por enseñarme a dar segundas oportunidades. Álvaro, mi amigo más antiguo de la ciudad (y el más guapo), gracias por ser el pegamento de este grupo. Cris M., qué orgullo de amiga. Gracias por estar ahí siempre que me ha hecho falta y darme en muchos momentos la calma que necesitaba. Txemikel, mi amigo querido, todos tus consejos valen oro, estoy súper orgullosa de la persona en la que te has convertido. Te espero pronto en Cádiz. Martinsito, tienes un corazón enorme y vales muchísimo, créetelo más. Gracias porque siempre te preocupas mucho por mí. JonLa, el vasco más gaditano. Me encantan tu ternura y la entereza con la que te enfrentas a todo en la vida. Iker, qué gran fichaje, amistad a primera (o segunda) vista. Cris S., empezaste siendo ”la que no queremos” para convertirte en una amiga muy importante. Eres un cordero con piel de arpía, a mí no me engañas. Jorge, gracias por ejercer de hermano mayor con tus consejos. Ojalá todos vieran la ciencia y la vida con la misma perspectiva que tú. Muchísimas gracias a los dos porque, especialmente estos últimos meses, he sentido que podía contar con vosotros en cualquier momento. Adri, no sé cómo lo haces para que me ría tanto siempre. La perrota no te olvida. Auguste, eres la dulzura hecha persona, gracias por todas tus muestras de cariño, por tus chistes malos (que me encantan) y por aguantar mis nervios escalando. Y gracias a muchísimos otros con los que he compartido millones de momentos: Jorgito, Sofi, Antonella, Joseba, Tamara, Ion, Edurne, Jose, Ana, Antton, María, Thomas, Bruno, Josu, Mikel, Raulillo y Miriam, entre otros.

Gracias a Natillas y Gise, con vosotras tuve un verdadero flechazo. De mi estancia en Barcelona me llevé dos grandes amigas. Gracias también a mi largui y a Susín, qué guay tener un trocito de Cádiz en la otra punta del país. Ojalá repetir esos tres meses con todos vosotros llenos de vermú, risas y planes.

A Diana y las chicas de Nortefitt, gracias por enseñarme a despejarme a través del deporte y por el grupo tan bonito que hemos formado. Mis leyendas del fitness, la sororidad que se respira en este grupo me emociona mucho.

A mis amigos de Sevilla, nos debemos muchas ferias. Ay Carmen, lo que daría por volver a compartir 24 horas al día contigo, eres un apoyo muy grande. Gracias por los podcasts que nos mandamos para ponernos al día, me hacen sentirte muy cerca. Javito, empezaste siendo un bebesín de laboratorio y mírate ahora, estoy muy orgullosa de ti, todo lo que tienes de buena persona lo tienes de currante. Cris, nuestra doctora, qué bonito haber formado parte de tu etapa en Sevilla. Ana, Ángela y Rosalía, gracias por haberme enseñado tanto sobre ciencia. A mis amigos de Física Shore, con los que de verdad aprendí a trabajar en equipo. La USED es de las mejores cosas que me han pasado (siempre por debajo de las noches en Bandalai, por supuesto). Sevilla siempre será un sitio muy especial para mí y eso es principalmente por vosotros. Marina, qué bonito que hayamos llevado caminos tan paralelos, ahora toca la recompensa a tantísimos esfuerzos.

A mis amigos de Cádiz, que me han enseñado que la distancia no hace el olvido. Esta tesis tiene mucho de vosotros, porque sin vuestro apoyo creo que no habría sido capaz. En nada estamos brindando con unos margaritas y cantando Andy y Lucas para celebrarlo. O en Rosita, que nunca falla. Aunque la vida adulta nos lo ponga más difícil para vernos, hay vínculos que nunca se rompen. Didi, te quiero más que a las gallinas. Gracias por apoyarme a diario y estar tan pendiente de cómo estoy. Voy preparando el bikini para ir a ver Love Actually en tu casa. Ade, mi amiga incondicional, no se me ocurre ni un solo momento en que no haya podido contar contigo. Ana Rodri, lo que unió la biblioteca ya no lo separa nadie. Nuestras charlas profundas que acaban en lágrimas y risas son un tesoro. Estoy orgullosísima de mis amigas médicas (que no doctoras). Anita Rosety, gracias por escucharme y aconsejarme siempre tan bien. Ve preparando bares de tapas para este verano. Fersito, qué afortunada me siento siempre que me recoges en mi casa y nos abrazamos, aunque normalmente te haga esperar y te abrace con la basura colgando. Mis pesadilla, ese grupo heterogéneo y con tantísimas cosas en común. Para la próxima quedada tenemos mucho que celebrar juntos y agradecer a la vida, espero que nos cueste un poco menos elegir una fecha. María, mi amiga desde siempre, cuántos recuerdos bonitos tenemos juntas. No sabes lo afortunada que me siento de haber crecido contigo. Ana Belén, te quiero a pesar de las clases de Física y Matemáticas. Lo que hemos cambiado desde la adolescencia (y menos mal), pero siempre manteniendo esta amistad. Por cierto, nos quedan muchas noches de bohemia. Guille, eres un corazón con patas. Gracias por cómo afrontas todo en la vida, con alegría y optimismo, me haces relativizar mucho. También por organizarnos siempre los mejores planes, creo que con las provisiones que llevas para un día en la playa podríamos sobrevivir un mes. ¡Ah! se me olvidaba: te quiero y de nada. Y qué suerte más grande que un viaje a Francia me regalara a dos amigos tan importantes. A Julia, mi otro yo, somos muy diferentes en algunas cosas pero muy parecidas para lo importante. Ojalá tenerte cerquita muy pronto (y que me avises de que coja el paraguas). Y a Juanca, un abrazo tuyo me alegra el día, la semana o el mes. ¿Os acordáis de cuando...? Hay cosas que nunca cambian, y nuestra amistad es una de ellas.

Millones de gracias a mi familia. Me habéis cuidado y educado siempre desde la ternura y el respeto. No podría estar mejor rodeada. Perdón por los numeritos que monto llorando siempre que nos despedimos. Mamá, gracias por dejar que me desahogue contigo, sigo sin entender el don que tienes para saber siempre cómo estoy, solo con decirte ”hola” por teléfono. No sabes lo feliz que me siento cuando me dicen que me parezco en lo más mínimo a ti. Eres el mayor ejemplo de superación que conozco. Papá, cuánto me gustaría compartir este momento (y muchos otros) contigo y ver cómo se te cae la baba, aunque intentaras hacerte el duro por fuera. Gracias por enseñarme a volar del nido y enfocarme en mis objetivos, aunque te preocupara que estudiase tanto, también he salido disfrutona como tú. A mis hermanas, siempre me apoyáis y me aconsejáis. Loreto, siempre me dices que de pequeña quieres ser como yo, pero soy yo la que tiene que aprender más de ti: a ser tan positiva, soñadora, empática y tierna. En nada estoy invadiendo tu espacio personal otra vez. Elo, gracias por abrirme las puertas de tu casa cuando lo necesité, que no fueron pocas veces. Qué suerte tenía de contar contigo en Sevilla y pasar un finde cualquiera juntas. Rocío, mi pegatina, me gusta que seamos inseparables desde siempre. En la etapa que se viene ahora, espero que más que nunca. Gamero, gracias por cuidarme y darme tanto cariño (normalmente en forma de comida). A mis sobrinas: Laila, Lydia y Malena. Me habéis enseñado una forma de querer que no conocía. Sacáis mi lado más tierno sin vosotras ser conscientes. Lo más duro de estar fuera, sin lugar a dudas, ha sido veros crecer desde la distancia. Espero que siempre sintáis que podéis contar conmigo.

Y, por supuesto, muchísimas gracias a Julen, eres la persona más buena que conozco. Quién me iba a decir cuando me mudé aquí que conocería a un vasquito que me enamoraría bailando la gasolina, y mírame ahora, que soy incapaz de imaginarme un futuro sin ti. Aún no me creo la suerte que tengo contigo, haces que me sienta en casa en cualquier rincón del mundo, solo por estar a tu lado. Ya lo sabes, *zuretzat ilargia lapurtuko nuke gauero*, o cualquier otra cosa con tal de que seas feliz. Contigo me siento capaz de cualquier cosa, me haces reír muchísimo y me das mucha paz. No se me ocurre mejor combinación para construir una relación tan bonita. Pero, si tengo algo que destacar entre otras cosas, es cómo me has cuidado y soportado durante estos últimos meses, ayudándome a despejar la mente siempre que lo necesitaba y entendiéndome mejor que yo misma en muchas ocasiones. Creo que necesitaría varias vidas para devolverte la mitad de todo lo que me das. Pero si son contigo, las quiero todas, viviendo un millón más de aventuras a tu lado, llenas de risas flojas y mirándonos con cara de tontos, como hasta ahora. Gracias también a tu familia y amigos, que me han acogido como a una más desde el primer momento, incluyéndome en sus planes.

Resumen

En las últimas décadas, la física cuántica se ha convertido en una de las áreas de investigación más activas. Más concretamente, desde la aparición de las tecnologías cuánticas, este campo está cobrando una gran relevancia, ya que estas tecnologías prometen revolucionar la forma actual de procesar, almacenar y transmitir información, basando su funcionamiento en efectos cuánticos tales como la superposición, el entrelazamiento o el confinamiento cuántico. Estas tecnologías encuentran su aplicación en campos como la criptografía cuántica, la computación cuántica, la espintrónica o la metrología cuántica.

Sin embargo, el desarrollo de las tecnologías cuánticas no solo implica la investigación en el campo de la física cuántica, sino que requiere del desarrollo y estudio en el área de la física de materiales, abarcando un amplio rango de sistemas, desde materiales electrónicos convencionales, hasta materiales más exóticos como los superconductores o los semiconductores magnéticos.

Para ello, la física de superficies, con sus técnicas de síntesis y caracterización, es una potente herramienta que permite el control, a escala nanométrica, de los materiales y sus propiedades. Muchos de los efectos necesarios para la realización de las tecnologías cuánticas ocurren en la interfaz entre dos materiales, como por ejemplo en el caso del efecto de proximidad, del que se hablará con detalle en esta tesis. Este efecto ocurre en la interfaz entre un superconductor y un ferromagnético aislante. Para ello, controlar la composición química y la estructura de las interfaces es primordial. Gracias a las técnicas de ultra alto vacío, es posible obtener interfaces planas y libres de contaminantes, potenciando el efecto deseado y, por tanto, mejorando el funcionamiento de los dispositivos que se basen en esas bicapas.

En concreto, esta Tesis se enmarca en el proyecto europeo superted, cuyo objetivo es la realización de un sensor de radiación electromagnética basado en el efecto termoeléctrico gigante. Dicho efecto fue predicho teóricamente en 2017 por A. Ozaeta y colaboradores y tiene un paralelismo con el efecto termoeléctrico convencional. En el efecto termoeléctrico se produce un desequilibrio entre electrones y huecos en la unión de dos conductores que se encuentran a diferente temperatura, produciéndose una corriente eléctrica, proporcional a la diferencia de temperatura y a constantes propias de los conductores. Dicho efecto puede utilizarse para fabricar termopares, comúnmente utilizados para medir temperaturas con precisión. En el caso del efecto termoeléctrico gigante, el desequilibrio ocurre entre los estados de espín arriba y espín abajo de un superconductor, cuando es sometido a un campo magnético o puesto en contacto con un ferromagnético. Este efecto puede ser utilizado para medir radiación electromagnética, suponiendo un gran avance en el campo de los sensores criogénicos. Estos sensores, basados en materiales superconductores, están formados por varios píxeles, cada uno de los cuales requiere de líneas de alimentación para su funcionamiento. Para aumentar la resolución de los sensores, la estrategia común es aumentar el número de píxeles, aumentando a su vez el número de líneas de alimentación. Esto acarrea dos problemas principales: por un lado, la complejidad de fabricar las líneas de alimentación y, por otro, el calentamiento asociado a las corrientes que circulan por dichas líneas de alimentación, que pueden llegar

incluso a producir la transición de superconductor a metal normal, impidiendo el funcionamiento del sensor. Para ello, el sensor de radiación propuesto en superted supone una gran ventaja, puesto que es autoalimentado, funcionando únicamente con la radiación que le llega y ha de medir y evitando, asimismo, la implementación de líneas de alimentación.

El desequilibrio en la densidad de estados, en función del estado de espín, del superconductor aluminio ha sido demostrado al ponerse en contacto con el ferromagnético aislante EuS, pero en presencia de campo magnético externo. Es por ello, que el punto de partida de este trabajo han sido las bicapas Al/EuS, que se han empleado para construir uniones de tipo túnel para demostrar el efecto de proximidad. Gracias al control de las propiedades de dichos materiales y su interfaz tanto a escala nanométrica como mesoscópica, estudiando cómo afectan las condiciones de preparación a dichas propiedades y adaptándolas a los requerimientos de la aplicación, se ha demostrado el efecto termoeléctrico gigante, incluso sin aplicar campo magnético externo.

A lo largo de este trabajo se presentarán estudios detallados del crecimiento de los materiales ferromagnéticos islantes explorados (EuS, $NiBr_2$ y $FeBr_2$), combinando técnicas de caracterización en ultra alto vacío y *ex situ*. Además, se estudiará la fabricación de las uniones de tipo túnel, necesarias para la realización del sensor basado en el efecto termoeléctrico gigante, estudiando las capas que lo conforman, así como las condiciones del experimento que pueden modificarse para mejorar su respuesta eléctrica (medida a través de espectroscopía de efecto túnel, en cuatro puntos). Y se introducirán otras aplicaciones en las que se han implementado estos ferromagnéticos aislantes.

Por lo tanto, esta tesis pone de relieve la importancia de controlar las propiedades nanométricas de los materiales, entendiendo cómo se ven afectadas por las condiciones del experimento, observando una mejora de la respuesta de los dispositivos fabricados en ultra alto vacío con respecto a los publicados anteriormente, y un aumento de la reproducibilidad de los resultados.

Abstract

In the last decades, quantum physics has become one of the most active areas of research. Specially, since the emergence of quantum technologies, this field is gaining interest, since these technologies promise to revolutionize the present way of processing, storing, and transmitting information, based on quantum effects such as superposition, entanglement, or quantum confinement. These technologies find their application in fields such as quantum cryptography, quantum computing, spintronics, or quantum metrology.

However, the development of quantum technologies involves not only research in the field of quantum physics but also requires development and study in the area of material physics, covering a wide range of systems, from conventional electronic materials to more exotic materials such as superconductors or magnetic semiconductors.

For this purpose, surface physics is a powerful tool that allows the control, at the nanometer scale, of materials and their properties by mean of the synthesis and characterization techniques. Many of the effects necessary for the realization of quantum technologies occur at the interface between two materials, as in the case of the proximity effect, which will be discussed in detail in this thesis. This effect occurs at the interface between a superconductor and an ferromagnet insulator. For that purpose, controlling the chemical composition and structure of interfaces is crucial. Thanks to ultra-high vacuum techniques, it is possible to obtain flat and contaminant-free interfaces, enhancing the desired effect and, therefore, improving the performance of devices based on those bilayers.

In particular, this thesis is part of the European project superted, which aim is the realization of an electromagnetic radiation sensor based on the giant thermoelectric effect. This effect was theoretically predicted in 2017 by A. Ozaeta and co-authors and has a similar to the conventional thermoelectric effect. In the thermoelectric effect, there is an imbalance between electrons and holes at the junction of two conductors that are at different temperatures, producing an electrical current proportional to the temperature difference. This effect can be used to make thermocouples, commonly used to measure temperatures with precision. In the case of the giant thermoelectric effect, the imbalance occurs between the spin up and spin down states of a superconductor when a magnetic field is applied or it is in contact with a ferromagnet. This effect can be used to measure electromagnetic radiation, representing a great advance in the field of cryogenic sensors. These sensors, based on superconducting materials, are formed by several pixels, each of which requires bias lines to operate. To increase the resolution of the sensors, the common strategy is to increase the number of pixels, also increasing the number of bias lines. This entails two main problems: on the one hand, the complexity of manufacturing the bias lines, and on the other hand, the heating associated with the currents that circulate through those bias lines, which can even cause the transition of the superconductor to normal metal, impeding the sensor to work. Therefore, the radiation sensor proposed in superted overcome this limitations, as it is self-powered, working only with the incoming radiation that has to measure, thus also avoiding the implementation

of bias lines.

The imbalance in the density of states, depending on the spin state, of the superconductor aluminum has been demonstrated when in contact with the ferromagnetic insulator EuS, but in the presence of an external magnetic field. Therefore, the starting point of this work has been the Al/EuS bilayers, which have been used to build the tunnel junctions to demonstrate the proximity effect. Thanks to the control of the properties of these materials and their interface both at the nanometric and mesoscopic scale, studying how the preparation conditions affect these properties and adapting them to the requirements of the application, the giant thermoelectric effect has been demonstrated, even in the absence of an applied magnetic field.

Throughout this work, detailed studies of the growth and characterization of ferromganetic insulators (EuS, $NiBr_2$ and $FeBr_2$) will be presented, combining characterization techniques in ultra-high vacuum and *ex situ*. In addition, the fabrication of the tunnel junctions needed for the realization of the sensor based on the giant thermoelectric effect will be studied, examining each layer and their interfaces, as well as the experimental conditions that can be modified to improve its electrical response (measured through four-probe tunneling spectroscopy). Moreover, other applications of these ferromagnetic insulators will be introduced.

Therefore, this thesis highlights the importance of controlling the nanometric properties of materials, understanding how theexperimental conditions affect them, observing an improvement in the response of the devices fabricated in ultra-high vacuum compared to those previously reported, and an increase in the reproducibility of the results.

Chapter 1

Introduction

Quantum technologies are a rapidly growing field that implies the application of quantum mechanics to create new technologies with enhanced capabilities. The emergence of these quantum technologies requires the discovery and synthesis of novel materials with specific quantum properties. The study of materials for quantum technologies encompasses a wide range of disciplines, including quantum mechanics, condensed matter physics, materials science, and engineering. Among other applications, quantum computing [1, 2], quantum communication or quantum sensing stand out. This Thesis will be mainly focused on cryogenic radiation sensors, where the materials explored along the manuscript find application.

In the past years, cryogenic radiation detectors, which are based on superconducting materials, such as the transition edge sensor [3] and the kinetic inductance detector [4] have been extensively explored. These sensors are some of the most sensitive detectors of electromagnetic radiation, finding application in various fields ranging from astrophysical observations to security imaging and materials characterization. The present tendency in this field is to increase the number of sensor pixels to allow for a simultaneous imaging and spectroscopy in the video rate of the measured object. However, since the detectors are based on the changes on the impedance, each pixel needs bias lines to feed it. Thus, increasing the number of pixels is hampered by the technical difficulty of fabricating and controlling the bias lines next to each pixel, along with the heating problem associated with them. Since the detectors are made out of superconductors, they work at cryogenic temperatures and a small increase in the temperature could lead to the transition from superconducting to normal metal state.

To overcome these limitations, a new type of sensor which is self-powered by the measured radiation is proposed. In the framework of the SUPERTED project [5] we have been working to develop this detector, which working principle is the thermoelectric conversion of the radiation signal to electrically measurable one, based on the newly found giant thermoelectric effect, predicted theoretically by A. Ozaeta and coworkers. This effect takes place in superconductor/ferromagnet heterostructures [6] and was experimentally confirmed in 2016 [7], in an excellent quantitative agreement with the theory. The working principle of the giant thermoelectric effect exhibits a big parallelism with the conventional thermoelectric effect, in which a temperature difference between two metals (or semiconductors) produce an electron-hole imbalance, generating a voltage. In the case of the giant thermoelectric effect, the imbalance is between the spin-up and spin-down states. For that purpose, the density of states of the superconductor has to be spin-splitted via exchange field and in turn coupled via a spin filter to another electrode. The presence of the spin splitting leads to a strong electron-hole asymmetry of the spin-resolved density of states. By means of the spin filter, the asymmetry can be driven across the detector, being a thermoelectric current.

The spin-splitting in the density of states of the superconductor can be achieved by placing a ferromagnet in contact, due to the magnetic proximity effect. The magnetic proximity effect is the phenomenon where the magnetic properties of a material are affected by its proximity to another magnetic material [8]. Specifically, when a non-magnetic material is brought into contact with a magnetic material, the magnetic field penetrates the non-magnetic material, influencing the spin of the electrons. The magnetic proximity effect has been observed in a variety of materials systems, including ferromagnetic/non-magnetic metal interfaces, ferromagnetic/semiconductor interfaces, and superconductor/ferromagnet hybrids. The latter case is particularly interesting because it gives rise to new and unique phenomena. For example, when a superconductor is placed in contact with a ferromagnetic insulator, the spin polarization of the electrons in the ferromagnetic material can penetrate into the superconductor, leading to a spin-dependent superconducting state. This state is often referred to as a "spin-triplet" state, in contrast to the conventional "spin-singlet" state found in most superconductors [9–11]. In principle, ferromagnetism and superconductivity are antagonists: while the former tends to align all the electronic spins, the latter is produced by Cooper pairs, which are quasiparticles formed by to electrons coupled with opposite spin. However, if the ferromagnet is insulator, ferromagnetism and superconductivity can coexist. The presence of proximity effect even in the absence of external applied magnetic field has only been demonstrated by the group of J. Moodera in Massachusetts Institute of Technology (MIT) in an EuS/Au bilayer [12], with a lack of reproducibility of results.

My role in the superted project has been to investigate the best combination of materials leading to an optimized giant thermoelectric effect, as well as to establish a relation between the properties at the macro and nanoscale of the materials and the interfaces, with the performance of the devices.

The superconductor/ferromagnetic insulator bilayer that showed magnetic proximity effect was, as aforementioned, Al/EuS bilayer [7], but this heterostructure required for the application of an external field to exhibit spin splitting. Thus, Al/EuS bilayer was chosen as the starting point to fabricate the junctions, in order to optimize the I-V characteristic and obtain the thermoelectric effect even without applied magnetic field. For that purpose, the surface science approach was needed to correlate the growth conditions with the chemical, structural and magnetic properties of the materials and their interfaces and, in turn, these properties with the mesoscopic behaviour of the junctions. This would lead to a better knowledge of the properties of the materials that have an impact on the performance of the junction and to an enhance of the reproducibility of the results. Once the devices based on Al/EuS bilayer have been proven, new materials, the bidimensional transition metal dihalides, were studied for their subsequent implementation in tunnel junctions.

Therefore, this manuscript is organized as follows: after introducing the objectives of the work in the present chapter, the techniques employed for the growth, fabrication and characterization of the materials and junctions, as well as the experimental setup implemented for this purpose, are presented in chapter 2. Chapter 3 contains the reported properties of the ferromagnetic insulators, which are the material class that most affect the response of the junctions. The detailed study of the thin layers of EuS, by a combination of *in situ* and *ex situ* characterization techniques, relating these results with the growth conditions can be found in chapter 4. The implementation of EuS in the tunneling junctions of the superted project, in addition to an optimization of the rest of materials and interfaces along the junctions is in chapter 5. But, EuS have been implemented in other spintronic devices, which are introduced in chapter 6. As aforementioned, in the second part of this thesis the growth of 2D-transition metal dihalides down to the monolayer regime was investigated, and the interaction with superconductors was explored in chapter 7. To end with, the main messages of the manuscript are summarized in chapter 8.

Chapter 2

Characterization techniques

In this Thesis, the main work has been performed under Ultra High Vacuum (UHV) conditions, with a base pressure below 10^{-9} mbar. Thin films of materials have been evaporated and characterized *in-situ* chemically, structurally and magnetically without breaking the vacuum. The devices that were explored in SUPERTED project were also manufactured in this chamber, as will be explained in detail below. In adittion, the layers and the devices have been characterized *ex-situ*, by AFM, in a Physical Properties Measurement System (PPMS) or by tunneling spectroscopy.

Later in this work, the importance of UHV will be highlighted, giving details about the control of the stoichiometry, the interfaces and the reproducibility of results with respect to other approaches. In this chapter, first, the system will be presented, then the *in situ* techniques will be explained to end with the *ex situ* characterization techniques.

2.1 Growth of materials

For the growth of EuS, the preferred technique is the sublimation from stoichiometric powder via e-beam evaporator, since the evaporation of sulphur via Molecular Beam Epitaxy (MBE) is technically difficult. The e-beam evaporator consists in a crucible surrounded by a filament. The crucible is made of a material that does not interact with the metal to deposit and with higher sublimation temperature than it (W in this case). The filament supplies a current of the order of the milliamps and a high voltage in the kV range. This filament delivers the necessary power to arise temperatures above a thousand centigrade. The evaporator is water-cooled during the process[13]. The sublimation temperature was estimated via the power vs temperature calibration curve available from the manufacturer. The growth rate was calibrated (before and after every evaporation) using a quartz microbalance, and monitored during the growth via the embedded flux monitor. The absolute values of the layer thickness were cross-checked by means of X-ray reflectivity (XRR) and used as a correction for the calibration of the microbalance.

At the beginning of the thesis, e-beam evaporator was employed also to evaporate Al. This kind of evaporators are useful for sublimating metals with elevated sublimation temperature. However, Al is a material that tends to wet the inner surface of the crucible and flow out. It is observed as an increment of the pressure in the chamber and a drastic drop in the flux current of the evaporator, indicating that there is no more material in the crucible. As a consequence, the UHV chamber has to be vented, opened, the evaporator has to be refilled and the chamber needs a bake out. This problem was solved by employing another type of evaporator: cold lip effusion cell. It consists in a big crucible of PBN (Pyrolytic Boron Nitride) that is heated up by radiation, with a wire filament and PBN rings for insulation. The top of the crucible presents a reduced heating system, to avoid the escape of the Al. This part is the cold lip[14]. It allows the sublimation of Al by increasing the temperature up to 1400 ºC. The temperature in the bottom part (hot) of the crucible is measured with a thermocouple and it is kept constant during the deposition.

The insulating barrier was produced by oxidizing the Al wire. In a separated chamber, an oxygen plasma with a pressure of 3-4 10^{-3} mbar was created with the help of a radio-frequency inductively-coupled plasma source. In contrast to the works aimed to make the barriers for the magnetoresistive tunneling devices, the plasma was extracted without using the acceleration voltage, thereby avoiding the sputtering effect of the O-ions on the surface of the Al wires.

2.2 *In-situ* surface science characterization techniques

2.2.1 X-Ray Photoemission Spectroscopy

X-Ray photoemission spectroscopy, XPS, is a surface sensitive technique for chemical characterization, having its basis on the photoelectric effect, introduced by Albert Einstein. This effect consists in the emission of electrons of a solid when shined with photons (light). As represented in Fig. 2.1 a), when a photon beam of energy $h\nu$ reaches the sample, excites an electron that escapes the material. The kinetic energy of this electron when arrives to the detector is measured (as observed in Fig. 2.1 b).

The relation between the energy of the incoming photons and the kinetic energy (KE) of the outcoming photoelectrons is:

$$h\nu = E_{KE} + E_{BE} + \phi$$

with BE the binding energy of the photoelectrons (the energy of the electron-nuclei bond) and ϕ the workfunction of the surface.

The binding energy is specific not only for each element, but for each species. The position and shape of the peaks allow not only for the determination of the composition of a material but for the chemical environment of a given element.

In XPS, the intensity of the emitted electrons (photoelectrons) is recorded as a function of their kinetic energy. However, due to its specificity, the common representation is intensity vs binding energy, as shown in Fig. 2.1 c, where the overview XPS spectrum of a monolayer of $NiBr_2$ on $NbSe_2$ is shown. But XPS spectra can be acquired at a given core level, obtaining detailed information about the oxidation state and the bonding of the atoms. In Fig. 2.1 d, the XPS spectra

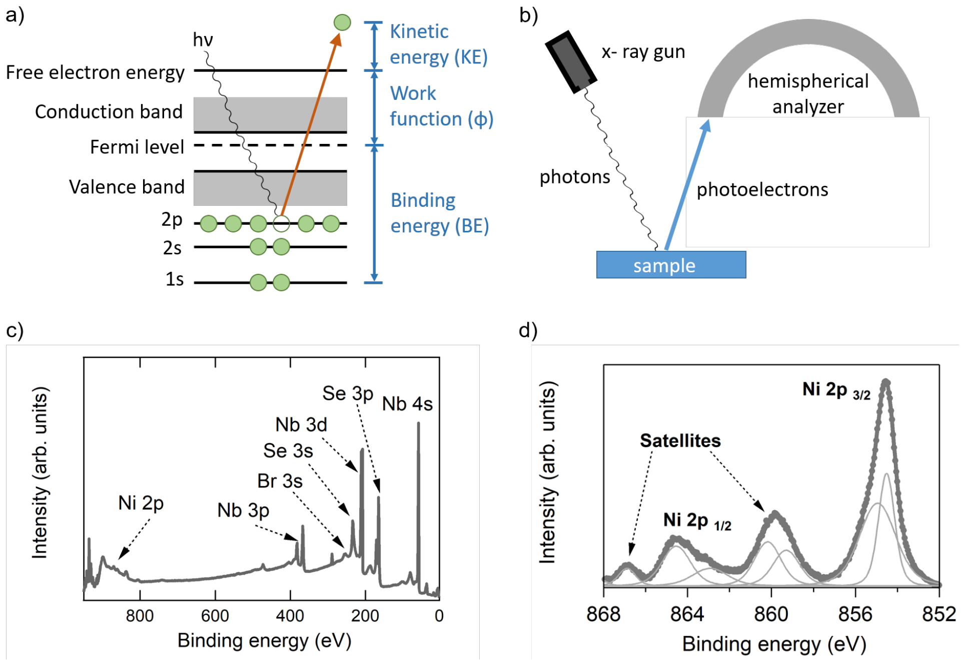

Figure 2.1: a) Scheme of the basis of the x-ray photoelectron spectroscopy technique. b) Representation of the set up of XPS. c) Example of an overview spectrum of XPS. d) Example of a XPS spectrum at the Ni 2p core level.

of the same sample at Ni 2p core level is displayed. It can be observed that the 2p energy level is splitted into two contributions ($2p_{3/2}$ and $2p_{1/2}$) due to the spin orbit coupling (SOC). In turn, the peaks can be deconvoluted, giving more information about the species. XPS spectra are formed by several classes of peaks. The most relevant peaks for this study are:

- Multiplet splitting. The final states can be splitted if there are unpaired electrons in the valence level. The unpaired electron left in the core-level after the photoionization can couple its orbital and spin momenta to the momenta of the unfilled valence levels in different ways, giving rise to different final states[15]. This multiplets appear in XPS spectra as a deconvolution of the principal peaks.

- Shake-up peak. The finite probability of an ion to remain in an excited state (few eV above the ground state) due to the excitation by the outgoing photoelectron, produces a decrease in the kinetic energy of this photoelectron, resulting in a "shake-up" peak at higher binding energy[16].

- Satellite peak. The interactions between the ejected photoelectron and the remaining electrons in the material leads to the creation of new energy states. These peaks can provide additional information about the electronic structure of the material. An important class of satellite peaks are shake-up peaks, where the outgoing photoelectron makes an electron promote to an excited state, leaving a hole in a lower energy level. The energy required for this transition produces a decrease in the kinetic energy of the photoelectron, which translates to a characteristic peak in the XPS spectrum, at higher binding energy than the main peak.

Moreoever, it is possible to perform a quantitative analysis of the XPS spectra and calculate the stoichiometry of a surface, and the thickness of a deposited thin layer. Given a material composed by two elements, the relation between them is:

$$\frac{n_1}{n_2} = \frac{I_1/S_1}{I_2/S_2} \tag{2.1}$$

where I is the number of photoelectrons per second in a specific spectra peak and S is the atomic sensitivity factor. This number is specific for each transition in an element and depends on multiple factors:

$$S = f\sigma\theta y\lambda AT \tag{2.2}$$

with f the x-ray flux (photons/cm^2·sec), σ the cross-section for the atomic orbital (cm^2), θ the angle between the photon path and the detector, y the efficiency in the photoelectric process for formation of photoelectrons of the normal photoelectron energy, λ the mean free path of the photoelectron in the sample, A is the area from which photoelectrons are detected and T the detection efficiency for electrons emitted from the sample.

The method that resulted in the most accurated results for the stoichiometry has proven to be taking the area of a well defined peak as the value of I in Eq.2.1.

In the present work, XPS was used to study chemical properties such as oxidation state and stoichiometry of thin layers as well as the interface with other materials.

2.2.2 Low Energy Electron Diffraction

Low-energy electron diffraction (LEED) was a pioneer technique in modern surface science. It is based on the electron scatering experiment on Nickel by Davidsson and Germer in 1927, where the wave nature of electrons was proben. In LEED, a beam of electrons with low kinetic energy (20-500 eV) incides perpendicularly to the surface, and the electrons that are elastically back-scattered by regions of high-localised electron density produce a diffraction pattern[17, 18].

This pattern is obtained due to the similarity in the wavelength of the incident electrons and the inter-atomic distances in the studied material (in the order of $\mathring{A}$). The de Broglie wave-particle duality stablishes that the electron beam can be regarded as a succesion of electron waves with a wavelength dependent of the moment of electrons:

$$\lambda = \frac{h}{p} \tag{2.3}$$

The penetration depth of the electrons is very small due to their low energy, being the LEED a surface sensitive technique.

To analyze a diffraction pattern, it is neccesary to work at reciprocal space, using the reciprocal lattice vector:

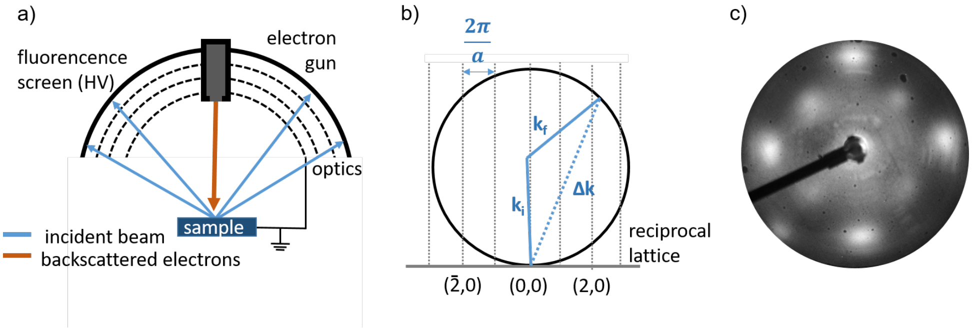

Figure 2.2: Low Energy Electron Diffraction: a) representation of the set-up of the experiment, b) Ewald sphere with the Laue condition for the existance of a diffracted beam and c) LEED pattern of 4 nm of EuS grown on InAs(001), acquired at 61 eV.

$$\overrightarrow{g_i} = \frac{2\pi(\overrightarrow{a_j}\ x\ \overrightarrow{n})}{|\overrightarrow{a_i}\ x\ \overrightarrow{a_j}|}; \qquad i,j = 1,2 \tag{2.4}$$

To obtain a diffraction pattern, the Laue conditions has to be satisfied:

$$\left(\overrightarrow{k_i}\ x\ \overrightarrow{k_f}\right)\overrightarrow{a_i} = 2\pi k; \qquad i = 1,2 \tag{2.5}$$

The conservation of the energy requires $|\overrightarrow{k_f}| = |\overrightarrow{k_i}|$. The Ewald construction, represented in Fig. 2.2 b), summarizes both conditions. A sphere with a radius of $|\overrightarrow{k_i}|$ contains all the possible $|\overrightarrow{k_f}|$ momentum vectors that fullfil the conservation of the energy. In the points where the dashed lines cross the Ewald sphere, the Laue condition is satisfied, obtaining a diffraction maximum.

The diffraction pattern provides the relationship between the substrate's reciprocal lattice and the superstructure's reciprocal lattice, leading to determine the superstructure's unit cell in real space.

2.2.3 Scanning Tunneling Microscopy

The scanning tunneling microscopy (STM) is a technique able to resolve surfaces down to the atomic scale. It was developed by Gerd Binnig and Heinrich Rohrer in 1981[19].

In this microscopy, a sharp, metallic tip scans the surface of a conducting material at such small distance (3-5 $\mathring{A}$) that the wavefunction of the tip and the sample overlap. The exponential decay of these wavefunctions enter in the junction gap. When a bias voltage is applied between the sample and the tip, the quantum mechanical tunneling occurs and a tunneling current (in the order of nA) appears. This tunneling current is proportional to the applied voltage, to the average barrier height (ϕ) and to the gap width, s, as writen in Eq. 2.6. The mechanism is represented in Fig. 2.3.

$$J_T \propto V_T exp(-A\ \phi^{1/2}\ s) \tag{2.6}$$

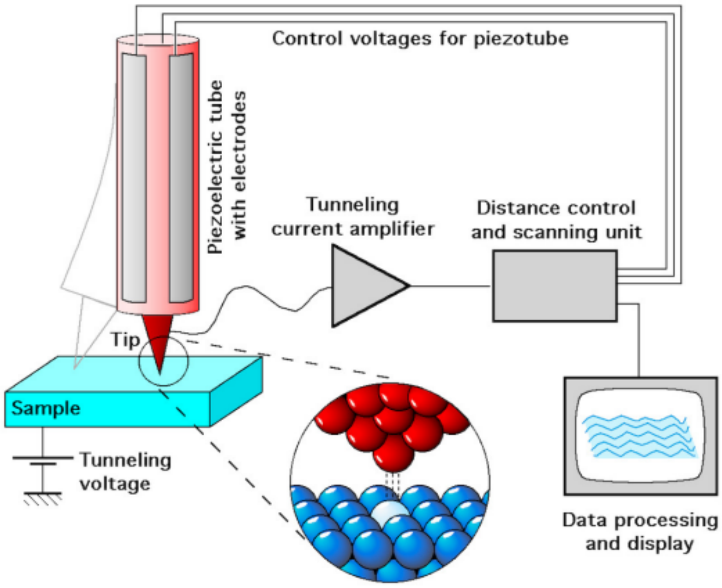

Figure 2.3: Schematic representation of the working principle of scanning tunneling microscopy (STM): the current is kept constant as the tip moves across the surface, experiencing voltage drops over bumps. The voltage is converted into a topographic image [20].

Both the occupied and unoccupied states can be studied by STM, by changing the polarization of the bias voltage, enabling the current to flow from the tip to the sample or vice versa.

2.3 Synchrotron techniques

The synchrotron light is of importance in the investigation of materials due to its capability of deliver much more photons than a laboratory source, with a higher resolution. It provides a continuous, wide spectrum, with the possibility of tunning the energy of the photons to the resonance of a certain element of the material and a well defined polarization.

2.3.1 X-Ray Absorption Spectroscopy

To obtain information about the empty states of the atoms in a material, X-Ray Absorption Spectroscopy (XAS) is employed.

The principle of XAS is similar to XPS: using photons to study a material. In the case of XAS, the excited electron does not escape the atom, but promotes to an empty state of the material when shined by photons. When the electron relaxes, emits photons that excite other electrons that escape the material. The total number of emitted electrons when the material relaxes (total yield) is registered as a function of the energy of the incoming photons, obtaining information about the empty states of a material [21].

If the incoming radiation is polarized, it is possible to study the geometry of empty orbitals of a material or its magnetic properties.

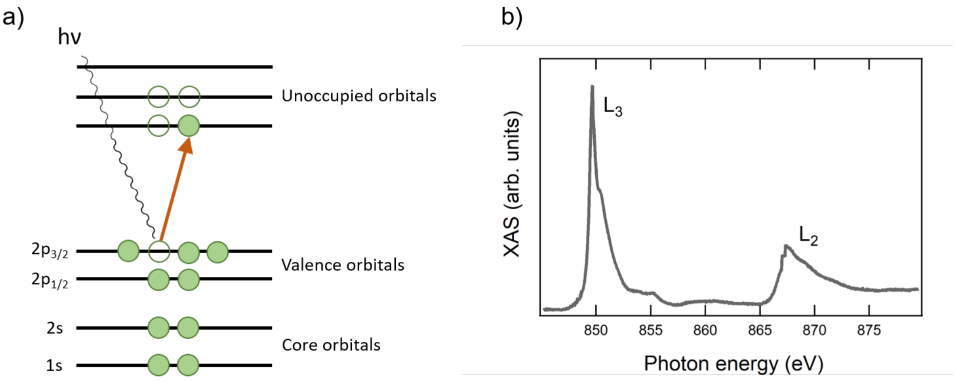

Figure 2.4: X-ray Absorption Spectroscopy: a) schematic representation of the process and b) XAS spectrum of Ni $L_{2,3}$.

X-Ray Magnetic Circular Dichroism

For the case of magnetic materials, the cross section of the absorption depends on the polarization of the light, obtaining different absorption spectra for left and right circularly polarized light. This difference in XAS is known as X-Ray Magnetic Circular Dichroism, XMCD[22].

The XMCD technique provides element specific magnetic information, since the energy of the photons is chosen to be in the range of a given transition between energy levels.

Hysteresis loops can be measured by means of XMCD, by sweeping a magnetic field while acquiring the absorption at the energy of the XMCD maximum.

For the quantification of the momenta, separating the orbital and spin contributions, the sum rules were introduced in 1992. A dichroic signal is obtained from the difference of two spectra measured with opposite polarization, while the so called whiteline is the average of them. If we call the possitive and negative circularly polarized spectra μ_+ and μ_-, respectively, the whiteline (μ) and the XMCD signal

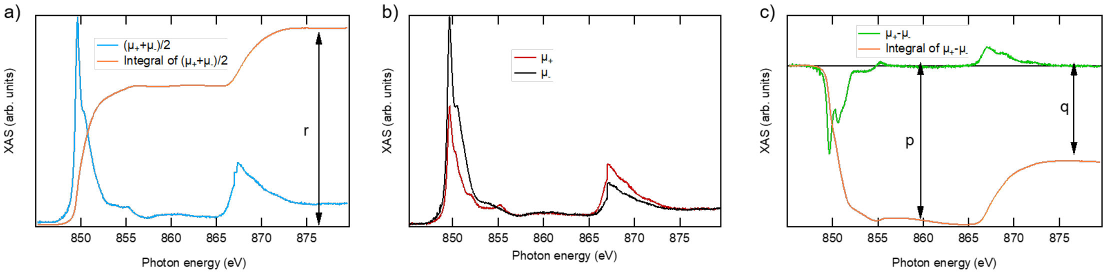

Figure 2.5: XAS and XMCD spectra at $L_{2,3}$ edge of Ni: a) whiteline with integration b) XAS spectra for positive and negative polarizations (red and black, respectively) and c) XMCD spectrum with corresponding integration.

(μ_{XMCD}) will be:

$$\mu = \frac{\mu_+ + \mu_-}{2} \tag{2.7}$$

$$\mu_{XMCD} = \mu_+ - \mu_- \tag{2.8}$$

Taking the integral over the whiteline and the XMCD spectra, the r, p and q parameters are obtained. For the case of $L_{2,3}$ edges, the sum rules method relates the orbital and the spin moment with these parameters. Following the notation of Chen et al. [23] the orbital and spin moments, in μ_B/atom, can be calculated as:

$$m_{orb} = -\frac{2}{3}\frac{q}{r}N_h \tag{2.9}$$

$$m_{spin} = -\frac{3p - 2q}{r}N_h\left(1 + \frac{7 < T_z >}{2 < S_z >}\right)^{-1} \tag{2.10}$$

with N_h the number of holes, $< T_z >$ the expectation value of the magnetic dipole operator and $< S_z >$ the expected value of z component of spin. For bulk materials as well as for cubic geometries $< T_z >$ is negligible.

X-Ray Linear Dichroism

In the case of linear polarization of the incident light, geometrical information about the material can be obtained. This is a consequence of the dependence of the selection rules on the dipolar distribution of the orbitals. The most prominent resonances in XLD at the energy of the $L_{2,3}$ transitions are related to the promotion of electrons from the s orbital (with no preferential orientation) to the p orbitals that are non uniform. The difference in the signal between the in plane and out of plane polarizations is the linear dichroism[24].

The polarization dependence of the absorption can be expressed as a function of the angle between the electric field vector and the direction of the bond.

2.3.2 Low Energy Electron Microscopy and Photoemission Electron Microscopy

Low energy electron microscopy, LEEM, is an imaging tool where back-scattered electrons form an image of 10 nm lateral resolution. The working principle is similar to LEED: electrons with low energy incide the sample and escape the material. In this case, the ellastically back-scattered electrons provide an image in real space and real time, with structural constrast[27].

In photoemission electron microscopy, PEEM, the surface is shined with photons and the emitted photoelectrons lead to the formation of the image[28, 29], providing chemical contrast, also with spatial resolution in real time.

Everything is represented in Fig. 2.6.

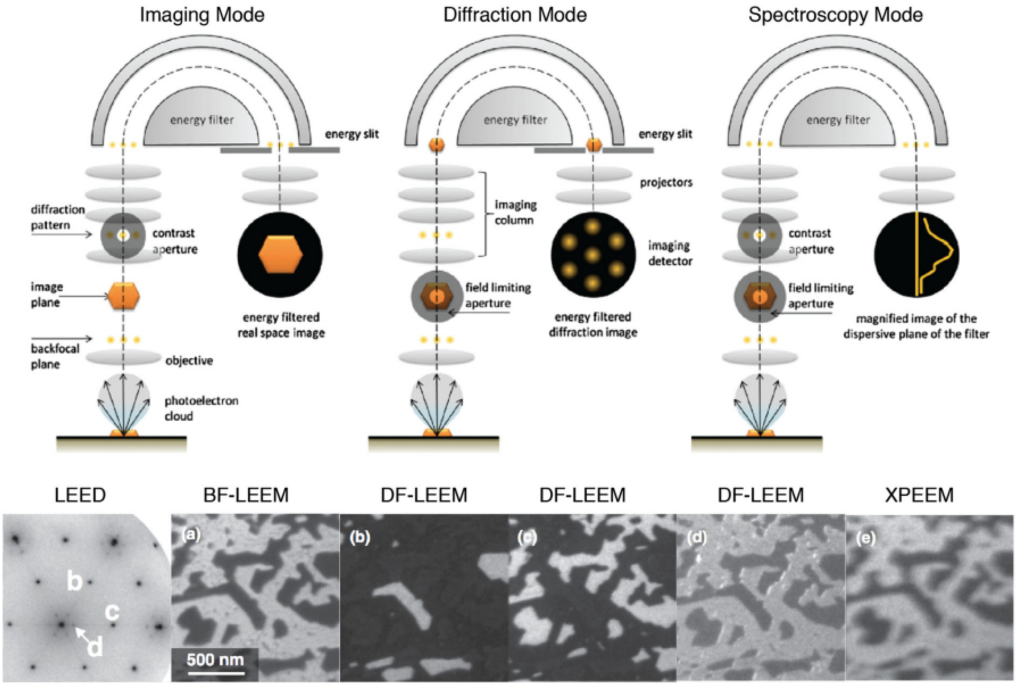

Figure 2.6: Schematic of the operational modes of LEEM/XPEEM: imaging, diffraction, spectroscopy. LEED pattern of Fe3O4/Pt(111) and (A) bright-field LEEM, (B–D) dark-field LEEM, and (E) XPEEM [25, 26].

2.4 Ex situ material characterization

2.4.1 Atomic Force Microscopy

Atomic force microscopy, AFM, is an scanning probe technique that allows to image surface structures. The main difference between this technique and STM is that AFM does not require extreme conditions, as low pressure or low temperature. Moreover, its is posible to perform AFM measurements in isolating samples[30, 31].

The working principle consists in a sharp tip integrated at the end of a cantilever, which is flexible. When scanning the surface, the tip finds features with variable height and the cantilever is deflected. This deflection is registered by a laser beam reflected from the back side of the cantilever.

There are two principle working modes in AFM: contact and tapping mode. In the first mode, the tip is always in contact with the surface during the scanning while in the latter, the AFM cantilever oscillates around the resonance frequency and the tip touches the surface at the lowest vertical position [30]. This is displayed in Fig. 2.7.

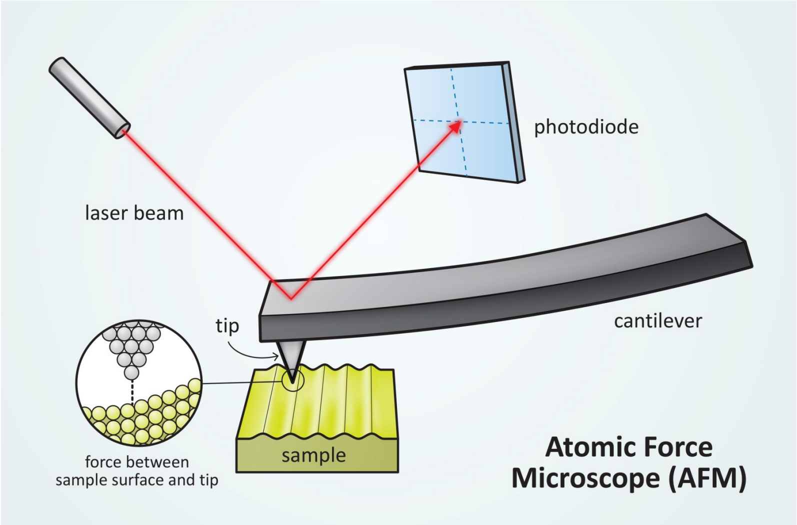

Figure 2.7: Schematic representation of an atomic force microscope [32].

2.4.2 Magnetic characterization by Physical Properties Measurement System

The Physical Properties Measurement System (PPMS) is a variable temperature/field system, designed to perform numerous different measurements, including heat capacity, resistivity, magnetometry and thermal transport, by adapting the conditions of the experiment. Fig. 2.8 shows the system. For this work, PPMS has been used to measure the magnetic loops of thin films and determine their magnetic moment and Curie temperature. For that, two different configurations were employed: vibrating sample magnetometry and ac-susceptibility.

Vibrating Sample Magnetometry

The basis of this technique is in Faraday's law, where an electromotive force is induced in a conductor by a variable magnetic flux. In VSM, the sample viabrates sinusoidally with small, fixed amplitude with respect to the stationary coils, under a homogeneous magnetic field.

The change in the magnetic field at a point (r) in the coil induces a voltage which is given by:

$$V(t) = \sum_n \int_A \frac{\partial \mathbf{B}(t)}{\partial t}\, d\mathbf{A} \tag{2.11}$$

with A, the area vector of a turn of the coil and the summatory of the n turns of the coil. **B**(t) is given by the dipolar approximation, assuming that the dimension of the magnetized sample is small compared to its distance from the detection coils[34].

Ac-susceptibility

The working principle of ac-magnetometry is similar to VSM: producing an electromotive force in the coil that can be detected and related to the magnetization

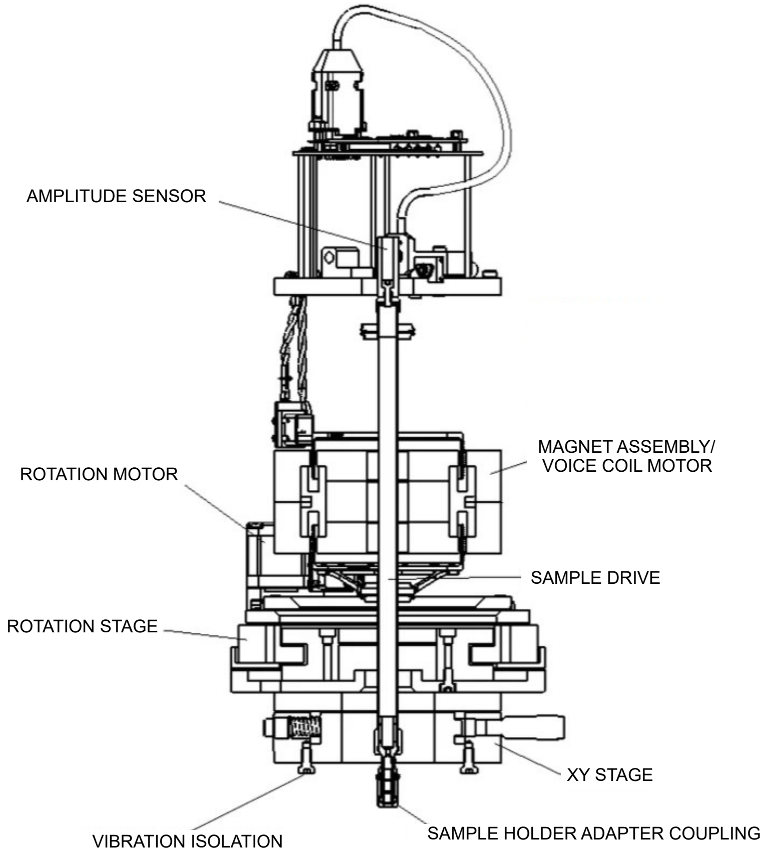

Figure 2.8: Sketch of a physical properties measurement system[33]

in the sample. In this case, the sample is static, and the magnetic field is a superposition of the dc field and an ac magnetic field. The latter leads to oscillating magnetic moments in the sample. By analyzing the amplitude and phase of the magnetic response as a function of frequency, it is possible to extract information about the magnetic properties of the material, such as the magnetic susceptibility, the magnetic anisotropy, and the magnetic relaxation behavior[35, 36].

In this Thesis, this technique will be used to measure the susceptibility, so hereafter I will refer to this technique as ac-susceptibility. This measurement technique can be used to determine the Curie temperature (T_C) of a material by measuring the temperature dependence of the magnetic susceptibility at a fixed frequency. By plotting the magnetic susceptibility as a function of the temperature of the sample, the maximum in the curve corresponds to the temperature at which the magnetic moments in the material become disordered and the material undergoes a phase transition from a ferromagnetic or ferrimagnetic state to a non-magnetic state, i.e. the Curie temperature.

2.5 The experimental setup for the growth and *in situ* characterization

With the aim to grow and characterize the FI/S interfaces and devices based on them, a new preparation chamber was implemented in the ultra high vacuum (UHV) chamber to allow to fabricate the devices without exposing it to air and using the growth and characterization techniques common in Surface Science. Hence, the complete machine consists on four UHV chambers (with base pressure of 10^{-9}-10^{-10} mbar) connected by valves, as can be observed in Fig. 2.9. This leads to the possibility to grow every layer, as well as to carry out the material characterization without breaking the vacuum. This is an important approach since the chemical composition of the layers and their interfaces are preserved during the whole process. The chambers for the characterization are the LEED and XPS chambers, where structural and chemical analysis are performed (more details about the techniques in sections 2.2.2 and 2.2.1, respectively). For the growth of the materials, a preparation chamber and an oxidation chamber are employed.

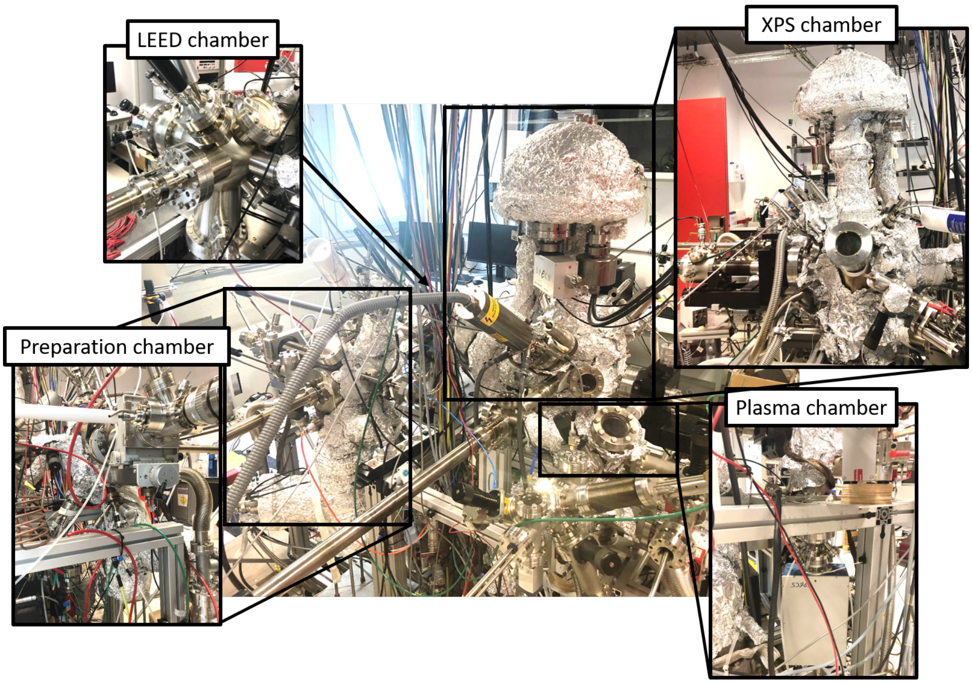

Figure 2.9: Ultra High Vacuum (UHV) system for the preparation and material characterization of devices.

The preparation chamber, shown in Fig. 2.10, contains several ports where evaporators can be placed. Those evaporators point to the center of the chamber. A quartz microbalance (QMB) to measure the rate of the deposition of material is also installed. For the cleaning of surfaces, the chamber has a sputter gun with Ar microcan for Ar^+ sputtering.

At the beginning of this thesis, a new manipulator for the preparation chamber was designed and installed. The novelty of this manipulator is the presence of three vertical slots to insert mask, enabling the growth of thin wires of materials in UHV suing shadow mask technique. From bottom to top, those slots are designed to insert: i) the heating filament to perform annealing or degassing of the samples, ii) the samples and iii) the shadow masks. The implementation of shadow masks in the machine allows the manufacture of devices, preserving the vacuum and, therefore, the quality of the interfaces. As shown in Fig. 5.2, some layers consist in metallic wires of 100 μm wide, with pads for measuring with probes. By evaporating a metal through the shadow mask (Fig. 2.10 d), the wire is obtained. The manipulator can be heated up to 1200 ºC (by resistive or sputter heating) and cooled down to liquid N_2 temperature. Fig. 2.10 b) contains the details of the calculations made for the proper design of the geometry of the manipulator, and the distance mask-to-sample, to ensure that the 5 mm long deposited wire will fit in the substrate and the width will not differ much from the nominal 100 μm of the mask.

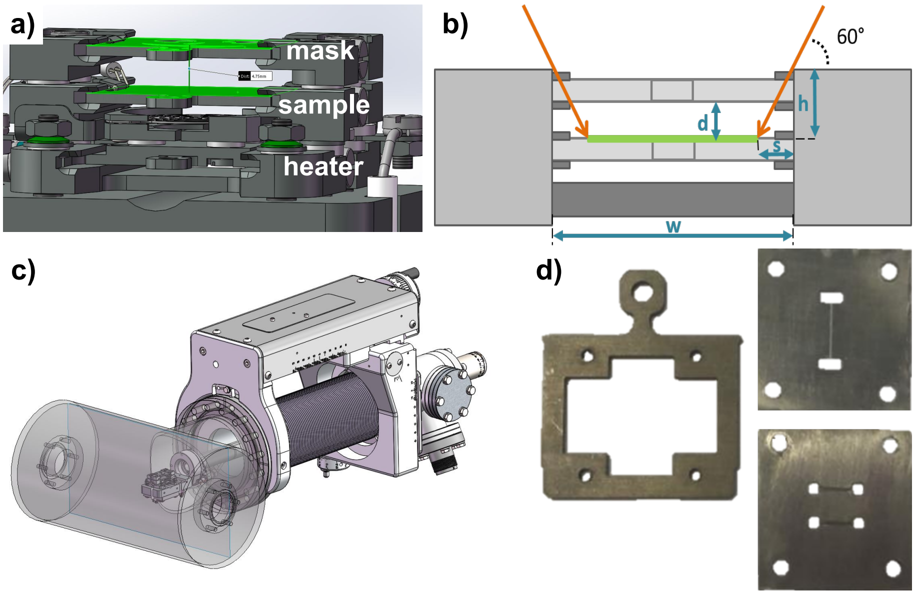

Figure 2.10: a) Representation of the manipulator with three slots for shadow mask, sample and heater. b) Schematic representation of the manipulator to calculate the proper distances to provide the full coverage of the sample during the deposition. c) Integration of the manipulator in the preparation chamber. d) Shadow masks.

Taking into account that the distance slot-slot is d=5 mm, the distance from the top most part of the manipulator to the slot for the sample is h=6 mm, and the angle of the cone of the deposited material entering the manipulator is 60 °, the following calculations for the uncovered part of the sample (s) and the covered part (w) were performed:

$$s = h\ tan(30^\circ) = 3.5\ mm \tag{2.12}$$

$$w = 15 - 2s = 8\ mm \tag{2.13}$$

The process of the manufacture of a device consisted in a multiple steps procedure that implies the evaporation of EuS and Al, the formation of the AlOx barrier and subsequent Co evaporation, followed by a protective layer deposition.

For the growth of EuS, the preferred technique is the sublimation from stoichiometric powder via e-beam evaporator, since the evaporation of sulphur via Molecular

Beam Epitaxy (MBE) is technically difficult. The e-beam evaporator consists in a crucible surrounded by a filament. The crucible is made of a material that does not interact with the metal to deposit and with higher sublimation temperature than it (W in this case). The filament supplies a current of the order of the milliamps and a high voltage in the kV range. This filament delivers the necessary power to arise temperatures above a thousand centigrade. The evaporator is water-cooled during the process[13]. The sublimation temperature was estimated via the power vs temperature calibration curve available from the manufacturer. The growth rate was calibrated (before and after every evaporation) using a quartz microbalance, and monitored during the growth via the embedded flux monitor. The absolute values of the layer thickness were cross-checked by means of X-ray reflectivity (XRR) and used as a correction for the calibration of the microbalance.

At the beginning of the thesis, e-beam evaporator was employed also to evaporate Al. This kind of evaporators are useful for sublimating metals with elevated sublimation temperature. However, Al is a material that tends to wet the inner surface of the crucible and flow out. It is observed as an increment of the pressure in the chamber and a drastic drop in the flux current of the evaporator, indicating that there is no more material in the crucible. As a consequence, the UHV chamber has to be vented, opened, the evaporator has to be refilled and the chamber needs a bake out. This problem was solved by employing another type of evaporator: cold lip effusion cell. It consists in a big crucible of PBN (Pyrolytic Boron Nitride) that is heated up by radiation, with a wire filament and PBN rings for insulation. The top of the crucible presents a reduced heating system, to avoid the escape of the Al. This part is the cold lip[14]. It allows the sublimation of Al by increasing the temperature up to 1400 $^{\text{o}}$C. The temperature in the bottom part (hot) of the crucible is measured with a thermocouple and it is kept constant during the deposition.

The insulating barrier was produced by oxidizing the Al wire. In a separated chamber, an oxygen plasma with a pressure of 3-4 10^{-3} mbar was created with the help of a radio-frequency inductively-coupled plasma source. In contrast to the works aimed to make the barriers for the magnetoresistive tunneling devices, the plasma was extracted without using the acceleration voltage, thereby avoiding the sputtering effect of the O-ions on the surface of the Al wires.

Chapter 3

Properties of the ferromagnetic insulators

Ferromagnetic insulators are a class of materials that exhibit magnetic ordering even in the absence of external field while the flow of current is impeded. Thanks to these unique properties, they are appealing materials for fundamental research and technological applications. They have been used to study physical phenomena as magnetic phase transitions, spin waves, magnon trans- port or spin currents [37–39]. They have been found multiple applications in a wide range of fields, being extensively used in magnetic memory storage devices [40], spin filters and spin polarizers in devices such as magnetic tunnel junctions (MTJs) [41, 42] or spin valves [43], and exhibiting potential for applications in quantum computing, to create and manipulate qubits [1, 2]. In the present chapter, the chemical, structural and magnetic properties of the ferromagnetic insulators employed in this thesis, reported for bulk, will be introduced.

3.1 Bulk properties of ferromagnetic insulator EuS

Since the discovery of ferromagnetism in EuO in 1961[44], the research in Eu chalcogenides was developed. The importance of semiconducting ferromagnets for applications in data storage motivated the investigation in this family of materials. Out of this class of materials, EuO and EuS are ferromagnetic, EuTe is antiferromagnetic and EuSe presents both phases[45].

Europium is a lanthanide, with 63 as atomic number and an electronic configuration of [Xe]$4f^7 6s_2$. When forming the EuS compound by bonding to sulfur, Eu shares the 2 6s electrons with S, resulting in an +2 oxidation state, with a half-filled 4f shell with a spin of 7/2.

EuS crystallizes in a cubic rock salt structure, with a lattice constant of 5.968 $\AA$, as displayed in Fig. 3.1.

As opposed to transition metal compounds, where the magnetism arises from the $3d$ orbitals, the magnetic properties of EuS, as in the rest of the europium chalcogenides, come from the 4f-shell of Eu. The 4f-shell is spherical and more tightly bound to the nucleus of the atom than the 3d orbital. For that reason, the electrons that are responsible of its magnetism are shielded by the electrons in the $5s$ and $5p$ orbitals, so the 4f electrons do not participate in the chemical bonding

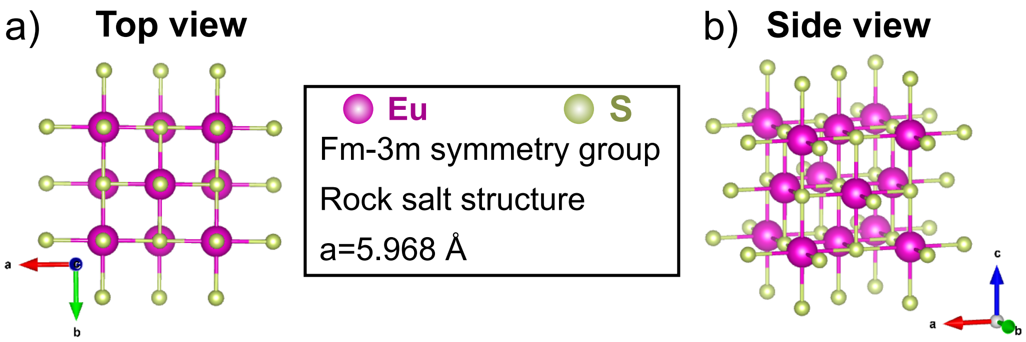

Figure 3.1: Crystal structure of EuS: a) top view and b) side view.

between the atoms. The magnetic moment is $7\mu_B$/Eu atom, since the 7 electrons in the 4f orbital are aligned, following the Hund's rules, being pure spin moment, without orbital component. The ferromagnetism of EuS comes from the positive exchange interaction between the Eu^{2+} ions in EuS, that are aligned below the Curie temperature (16.8 K). Since the electrons that take part in the magnetism of EuS are highly localized in an orthogonal orbital, it can be considered as a Heisenberg ferromagnet, and the effective exchange energy (H_{ex}) can be described as:

$$H_{ex} = -2\sum_{i<j} J_{ij}\hat{S}_i\hat{S}_j \tag{3.1}$$

where $S_{i(j)}$ is the spin angular momentum operator at site i (j), and J_{ij} is the exchange constant.

3.2 Layered van der Waals dihalides: NiBr2 and FeBr2

The field of bidimensional materials is growing fast in the last two decades, since the exfoliation of graphene in 2004 [46]. The new intringuing physical properties that come up when the dimensionality of materials is decreased lead to potential applications. Among other applications, the possibility of substituting silicon by van der Waals heterostructures in the complementary metal-oxide-semiconductor switches for lower power consumption has increased the number of publications in this field. With that aim, investigation of the properties of those heterostructures, both on the microscopic and mesoscopic level, reaching the length scale relevant for possible low-dimensional applications is required.

There are plenty of theoretical studies predicting magnetism in monolayered materials[37, 47–53], but only a few intrinsic 2D ferromagnets were experimentally found. [54–65] The most explored magnetic 2D materials are trivalent halides MX_3 (M=metal, X=halide), that were first mechanically exfoliated and recently found to be grown by Molecular Beam Epitaxy (MBE) in ultra high vacuum (UHV)[66]. Bulk divalent halides (MX_2) are known to be magnetic, but there were not studies in the limit of a single layer[67, 68].

$NiBr_2$ is a van der Waals semiconducting material, with a Ni plane embedded between two Br planes. Its in-plane lattice constant is 3.7 $\mathring{A}$, and the interlayer distance, 3.24 $\mathring{A}$[65]. The oxidation state of Ni atoms is 2+, since they use 2 valence electrons to bond to the Br atoms. The Ni^{2+} ions are octahedrally coordinated, with a $3d^8$ electronic configuration with a filled t2g and a half-filled eg levels. The nominal magnetic moment of Ni ions is 2 μ_B, which only contribution comes from the spin moment, while angular momentum is quenched. For the bulk material, the ordered magnetic state consists in ferromagnetic slabs stacked antiferromagnetically along the crystallographic c-axis, with a Curie temperature of 52 K [67]. The theoretically predictions for bidimensional $NiBr_2$ suggest a ferromagnetic ground state with a net magnetic moment between 1.57 and 1.88 μ_B [55, 65]. For the Curie temperature of a monolayer of $NiBr_2$, a calculated value of 136–140 K has been reported. This value is rather higher than the T_C of 2D trivalent halides (below 45 K) [55, 65].

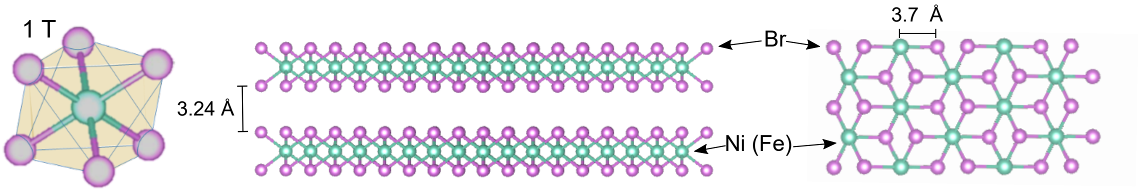

Figure 3.2: Schematic representation of the $NiBr_2$ structure. Side (left) and top (right) view.

Chapter 4

Ferromagnetic insulator EuS thin films

In the previous Chapter (3.1), the properties of bulk EuS were presented. However, in this thesis, EuS is implemented in devices as thin films, where properties strongly depend on the thickness, the composition and the structure. And all this parameters are determined by the film deposition. Thus, in the present chapter the aim is focus on the evaporation of EuS thin films and how the preparation process unveiled strong variation of the chemical composition. The thermodynamics of the sublimation process were studied in detail by Smoes and coworkers in [69], showing that EuS powder decomposes during evaporation and the ratio Eu:S in the gas phase varies with increasing temperature, from nearly 1:1 ratio at 1100 ℃to the Eu-rich mixtures at temperatures above 1700 ℃.

The study of the properties of the thin layers made out of this ferromagnetic insulator, which are necessary for applications in devices, have been focused principally in the epitaxial growth on substrates that are not suitable for many applications. The poor reproducibility of the performance of the devices and a lack of understanding of the causes motivate this study.

In this chapter, are discussed the properties of thin EuS films sublimated in UHV conditions. First, thin films of EuS were grown on InAs(100) to explore the epitaxial growth on this semiconductor. Next, the impact of the parameters of the deposition (pressure, thickness, sublimation temperature) on the chemical and magnetic properties of this layers of EuS are presented.

The EuS was evaporated from stoichiometric powder using a electron beam evaporator, varying the thickness or the power supplied to the evaporator depending the case. The chemical properties were explored by XPS, the structural characterization was performed by a combination of LEED, AFM, STM and TEM, and the magnetism was studied via XMCD, VSM and ac-susceptibility.

4.1 Polycrystalline epitaxial growth on InAs(100)

Single-crystal magnetic materials exhibit enhanced magnetic behaviour with respect to polycrystals. Thus, the implementation of an epitaxial layer of a magnetic material in a device, allows for the performance at higher temperature, due to its higher T_C with respect to the amorphous material.

The research on the epitaxial growth of EuS started long time ago and several substrates have been employed for that purpose. Chen and Zeitman reported the first attempt in 1964 [70], where the epitaxial growth of EuS on MgO, CaF_2, NaBr and NaCl were reported as well as the formation of polycrystalline films on Cu, Si, Ge and mica. In 1973, Reichelt and Viehweg achieved the epitaxial growth of EuS on mica [71], and in the 80s Zinn et al. proved it on Si [72–74]. Some of these outcomes are striking, given the significant discrepancy between the lattice of EuS and materials such as MgO or Si. In order to explain their results, the authors determined that the substrate temperature during the crystallinity growth of EuS films was a determining factor. Thus, Zinn et al. reports that below 900°Ca polycrystalline EuS layer is produced on Si while single crystal films grow above this temperature. More recent works focus on PbS and BaF_2 substrates, and determine that the most ordered films were deposited at a substrate temperature ranging from 200 to 400 °C[75, 76]. Most recently, Goschew et al. [77] demonstrated the epitaxial growth of EuS on PbS and InAs. Both materials present a zinc-blende crystalline structure with a lattice constant of 5.869 and 6.058 Å, respectively, that compared to the lattice parameter of EuS (5.968 Å), results in a mismatch of only 1.7 % and 1.5 %, respectively. InAs has also been shown as a good candidate to form nanowires where EuS is deposited epitaxially. Some of the facets were covered with EuS while in the others superconducting Al was grown. This hybrid structure was proven to exhibit exchange coupling in the absence of external applied field[78].

Given these results, InAs was chosen as the substrate for the epitaxial growth of EuS in this work. Indium arsenide is a semiconductor composed of indium and arsenic. The InAs (100) face can end in In or As. After the preparation under UHV conditions, in the absence of an As atmosphere, the InAs (100) typically shows a $c(4 \times 2)/(8 \times 2)$ surface reconstruction due to the formation of In rows. First step to achieve the epitaxial growth of EuS on InAs(100) is to obtain a clean, flat and ordered substrate. To find the optimal parameters to clean the InAs(100), a wafer with 10x10 mm^2 area was introduced in the UHV chamber and degassed prior to proceed with subsequent cycles of Ar^+ sputtering and annealing. The surface crystallinity was followed via LEED and RT-STM, and the most relevant results are presented in Fig.4.1.

For temperatures below 400°C (Fig.4.1a), the LEED pattern, although visible, presents a strong background, meaning that the surface is not well ordered. This is confirmed by STM that reveals a surface formed by very small grains. Increasing the temperature of the annealing (from 410 to 465 °C), Fig.4.1b-c, the surface roughness reduces and large terraces appear. The LEED pattern presents the 4x2/c(8x2) reconstruction expected for In-rich surface [79]. When the annealing temperature reaches 500°C, the LEED is still presenting the same reconstruction, but bubbles can be observed in the STM images (marked with green arrows in Fig.4.1d) meaning that an overheating of the surface has taken place.

Once the substrate preparation has been optimized, EuS is evaporated by electron beam sublimation, in UHV conditions (10^{-9} mbar), with the substrate at room temperature and maintaining the deposition rate around 0.1 nm/min. A thin layer of EuS was inspected via RT-STM, but the insulating character of the EuS hindered the acquisition of reliable images, hence, AFM images, as the ones shown in Fig.

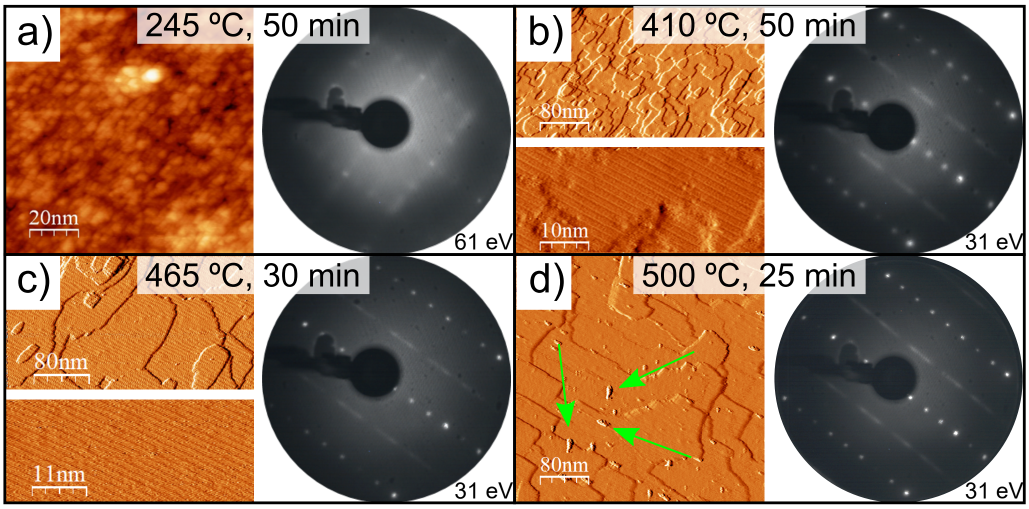

Figure 4.1: The evolution of the surface ordering of InAs (100) with the preparation cycles.

4.2, were measured. Five micrometer size image shows a quite smooth layer formed by small crystals (Fig. 4.2a), as confirms the high magnification image on Fig. 4.2b.

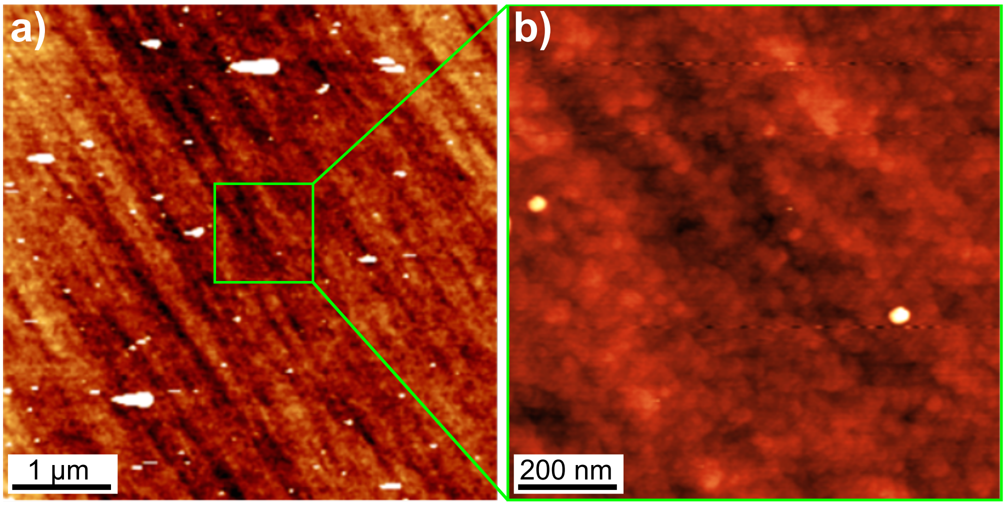

Figure 4.2: AFM images of an EuS layer grown on InAs (100) at different scale a) 5x5μ^2 and b) 1x1μ^2

A thicker EuS layer (≈40 nm) was produced and covered with $approx$5 nm of Al to prevent the oxidation outside the UHV chamber. The structural characterization of the sample was performed via a combination of Transmission Electron Microscopy (TEM), X-Ray Diffraction (XRD) and X-Ray Reflection (XRR), as represented in Fig. 4.3. The cross section of the sample was inspected via TEM and the images are presented in Fig. 4.3 a-c. TEM confirms the ordering in the InAs substrate that was already observed by LEED and STM in Fig. 4.1. The EuS layer also shows ordering, specifically along the (200) axis, as XRD displays the (200) and (400) EuS peaks at 30° and 62.0°, respectively. This ordering may result contradictory regarding the results from AFM images (Fig. 4.2) where a polycrystalline textured growth of EuS was presented. However, at the interface between EuS and InAs, a different phase is observed. As aforementioned, the mismatch between EuS and InAs lattices of ≈ 1 % permits the epitaxial growth of EuS/InAs bilayers but Liu and coauthors[63] find at the interface a region with around two monolayers thickness with a 10% lattice compression. In Fig.4.3a, the interface is around 5 nm thick, and this extra thickness is attributed to the In atoms diffusion into the EuS phase, caused by the In-terminated surface obtained during the preparation of the substrate, and the absence of temperature of the substrate during the deposition of EuS, which is highlighted in previous works[72–74, 77]. Despite this could be regarded as a disappointing result, given the thick interlayer between the two materials, the fact that ordered EuS can be produced at room temperature is positive for the application in devices, where sometimes EuS has to be evaporated onto patterned substrates that cannot be heated up, and also it is easier for a possible scale to industry. The microscopic result from TEM is confirmed also by a macroscopic technique, XRR, which shows the exact same 5 nm interface between EuS and InAs (Fig.4.3 e).

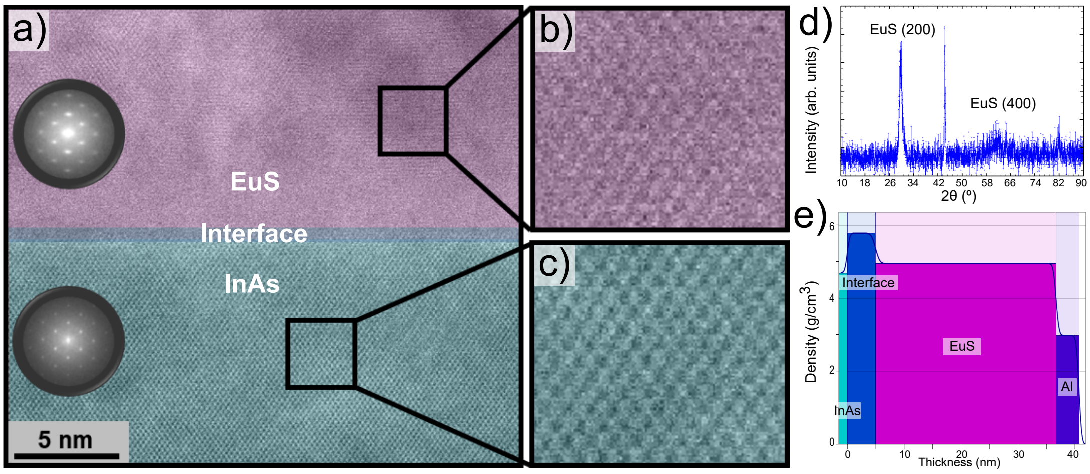

Figure 4.3: TEM image of the cross section of 40 nm on InAs, with three different areas (from top to bottom): ordered EuS, interface and InAs substrate. (b-c) Zoomed TEM image of EuS and InAs, respectively. d) XRD with the EuS peaks, showing the (200) orientation of the layer. e) Schematic representation of the sample based on the XRR results, confirming the presence of a 5 nm interface between EuS and InAs, with higher density than the ordered EuS.

The disordered interface was proven by means of a different approach: two EuS layers were grown on InAs(100), each of them with different thickness. The first layer was 1 nm thick, which is below the thickness of the interface, and the second layer was 5.5 nm, a value right above the interface. The LEED patterns of both were collected and presented in Fig. 4.4. For the case of the thinnest sample, no pattern was observed, confirming that the surface is composed of multiple small crystal aranged in random orientations. By contrast, the 5.5 nm sample exhibits the 1x1 LEED pattern, typical for a rock salt structure, revealing that the surface is epitaxial, as indicated in Fig. 4.3. Nonetheless, the diffraction spots are quite broad, indicating the presence of defects, such as dislocations.

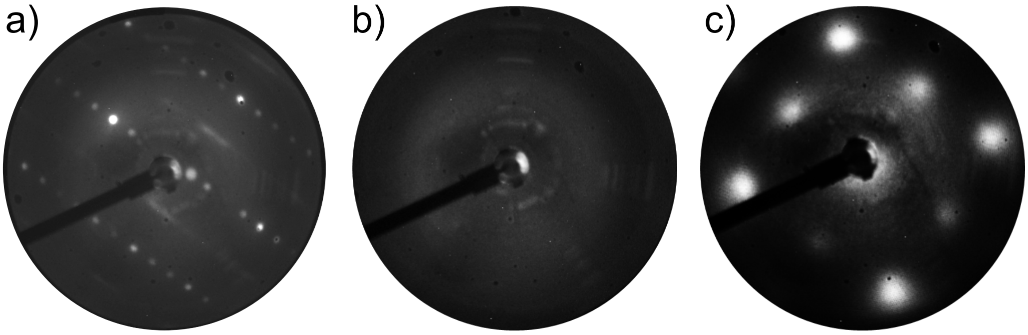

Figure 4.4: LEED patterns measured at 65 eV of a) pristine InAs (100), b) 1 nm and b) 5.5 nm of EuS grown onto it.

In order to determine magnetic domains of the grown EuS layer, a sample with ≈10 nm thick EuS was measured using Magnetic Force Microscopy (MFM). A comparison of the topography and magnetic response at zero and 10000 Oe is presented in Fig. 4.5. In this configuration, the applied magnetic field is perpendicular to the sample, which may not affect the appearance of MFM images with and without the field. Moreover, the images at zero field were acquired after the magnetization of EuS.

Not clear magnetic contrast is observed neither in absence nor in the presence of magnetic field. The maximum contrast is obtained around a defect (at the left top corner of the images), which was used by the AFM tip as reference. This means that the samples in this study are single domain, in contrast with the P. Tischer et al. work[80], that showed magnetic domain walls in an EuS layer with 40 nm thickness at a similar scale, using a Lorentz microscope.

In summary, the deposition of EuS layers on clean, ordered and flat InAs(100) surface at room temperature leads to the formation of an ordered, crystalline EuS layer, with an interface of 5 nm thickness caused by the diffusion of In atoms on EuS.

4.2 Chemical and magnetic properties

The production of thin films of EuS is a challenging process that with significant implications in a vast range of fields. Despite EuS is the most characterized material of its family, Eu and S can form other compounds as di-, tri- and tetrasulfides of Eu. Moreover, europium has a strong affinity for reacting with oxygen to form oxides and sulfates (compounds that contains Eu, S and O). Some of them, as EuO, are magnetic materials, but most of them are paramagnetic.

The stability and properties of these materials depend of the synthesis conditions and composition. Therefore, its is crucial to study how the growth conditions affect the chemical composition and the magnetic properties of the thin films. Thus, in this section, a combination of XPS, VSM, ac-susceptibility, and XMCD techniques was used to elucidate the parameters that control the chemical composition and, consequently, the magnetic properties.

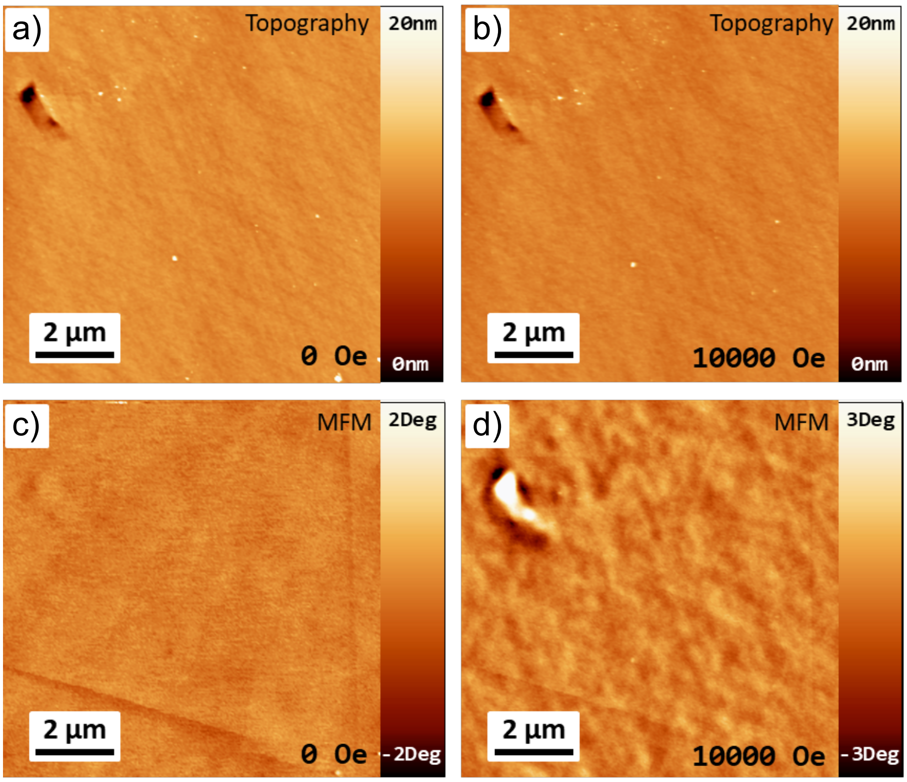

Figure 4.5: MFM images of 11 nm of EuS on InAs (100): topography (top) and magnetic contrast (bottom), in the absence of field (left) and with a perpendicular applied magnetic field of 10000 Oe (right). Images were acquired at 10 K.

For a better understanding of the XPS results that will be discussed in this thesis, and specially in this section, an example of the Eu $3d$ core level XPS spectrum of thin film of EuS is presented in Fig. 4.6. This core level is presented after a background substraction. First, the photoemission spectrum is composed by two main peaks associated to the spin orbit components: Eu $3d_{3/2}$ and Eu $3d_{5/2}$ centered at 1154.14 eV and 1124.95 eV, respectively ($\Delta E = 30 \pm 1$ eV between them). Second, this core level presents several shake-up and satellite peaks, as labelled in the image. The shake-up components are originated by the non-monochromatic character of our XPS lamp (at 9.8eV lower B.E. w.r.t. the core level). The satellite, located at 1133.1 eV and 1161.1 eV, coincide with the previous assessment of the Eu^{2+} oxidation state[81]. Finally, in order to properly fit the entire core level, two additional peaks, centered at around 1134.03 eV and 1163.03 eV, are necessary. They are associated to a small contribution from Eu^{3+} phase according to previous works [82–84].

Now that the XPS spectrum has been introduced, the impact of the growth conditions on the chemical and magnetic properties will be studied.

4.2.1 The importance of Ultra High Vacuum

For the fabrication of devices containing EuS, groups are commonly working in the High Vacuum regime, with a base pressure of approximately 10^{-7}-10^{-6} mbar.

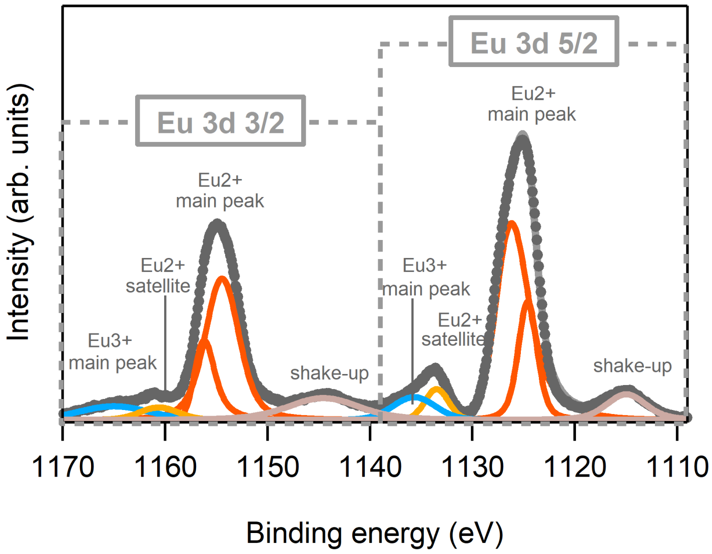

Figure 4.6: Example of a XPS spectrum of EuS at the Eu 3*d* core level, with the contributions labelled.

Under this condition, the residual gas in the vacuum chamber typically contains O_2, H_2O, and CO_2. In order to probe whether these gases affect the chemical composition of the deposited layers, EuS was sublimated under different pressure conditions. Figure 4.7a shows the Eu 3*d* core level measured for 3 nm EuS layers grown with the same parameters on SiO_2/Si, under three different vacuum conditions: Ultra High Vacuum (UHV), 10^{-9} mbar, and High Vacuum (HV) 10^{-7} mbar and 10^{-6} mbar. The intensity of all the spectra have been resized to make all the S 2*s* spectra have the same height, and are presented after subtracting a Shirley background.

For the sample prepared under UHV conditions, the main contribution comes from the Eu^{2+} component, matching the reports from Eu^{2+} oxidation state[81]. For the sample prepared under 10^{-7} mbar, as opposed to UHV conditions, the intensity of the Eu^{3+} component is significantly larger, being even the most important for 10^{-6} mbar, suggesting that samples are oxidizing due to the presence of residual gas. For a better understanding of what is happening, Fig. 4.7b-c, shows the S 2*s* and O 1*s* core levels acquired for the UHV (black) and the HV (10^{-6} mbar) (green) samples

In the S 2*s* spectra (Fig. 4.7b) the same chemical state for sulphur is observed, regardless the pressure during deposition, while the amount of oxygen in Fig. 4.7c dramatically increases when the pressure is high. Thus, Eu is bonded to O as Eu^{3+} state, forming Eu_2O_3. Note that the small contribution to the O 1s core level observed on the UHV sample is due to the oxygen in the SiO_2 substrate.

Hence, the residual gas in the chamber and, therefore, the pressure of the system plays an important role on the chemical composition of EuS, highlighting the importance of working under UHV conditions to obtain the proper 2+ oxidation state of Eu in EuS.

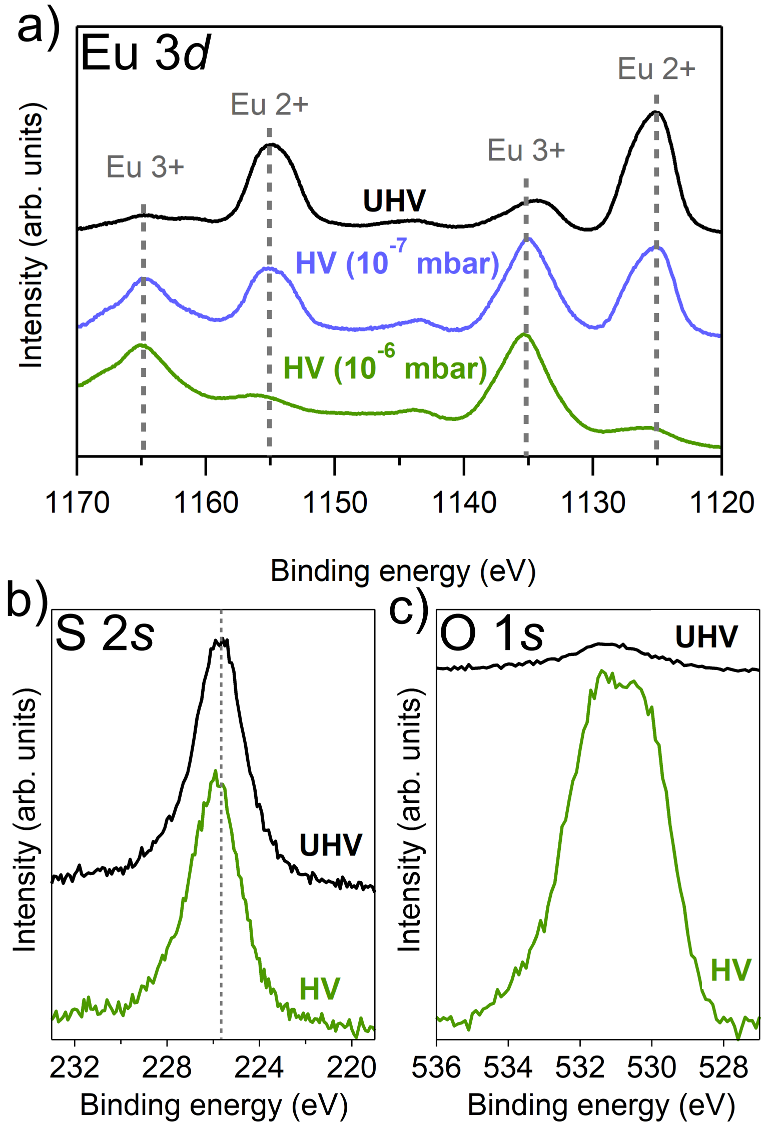

Figure 4.7: XPS spectra at Eu 3*d* core level of EuS grown under different pressures: 10^{-9} (black), 10^{-7} (blue) and 10^{-6} (green) mbar.

4.2.2 The role of sublimation temperature

In order to increase the thickness of a deposited material there are two possible strategies: extending the time of the evaporation and increasing the deposition rate. Since in some materials, principally metals, an increase of the evaporation time causes the oxidation of deposited layer, the usual approach is to maintain a constant time and increase the deposition rate, which directly depends on the power supplied to the evaporator, i.e., the sublimation temperature. In the case of EuS, to maintain a constant deposition rate between evaporations, it is necessary to increase the flux and, therefore, the sublimation temperature. At the beginning of this Thesis, when studying the properties of EuS thin films prior to its implementation in devices, multiple evaporations were performed and a lack of reproducibility on the results was observed. For that reason, a systematic study of the chemical properties of

EuS layers deposited at different sublimation temperatures was performed. EuS layers with 11 nm thickness were grown under UHV conditions, onto a SiO_2(100 nm)/Si substrate, varying the sublimation temperature among the samples. This sublimation temperature was estimated via the power vs temperature calibration curve provided by the evaporator manufacturer.

The chemical composition of these samples was studied via XPS. Fig. 4.8 summarizes the photoemission spectra acquired at the Eu $3d$ (left) and S 2s (right) core levels to make the comparison. The shape of the Eu $3d$ and S $2s$ spectra do not change significantly, except the peak B (in Eu $3d$), that narrows when the sublimation temperature increases. The changes in the intensity are not reliable in these spectra, since they are not normalized.

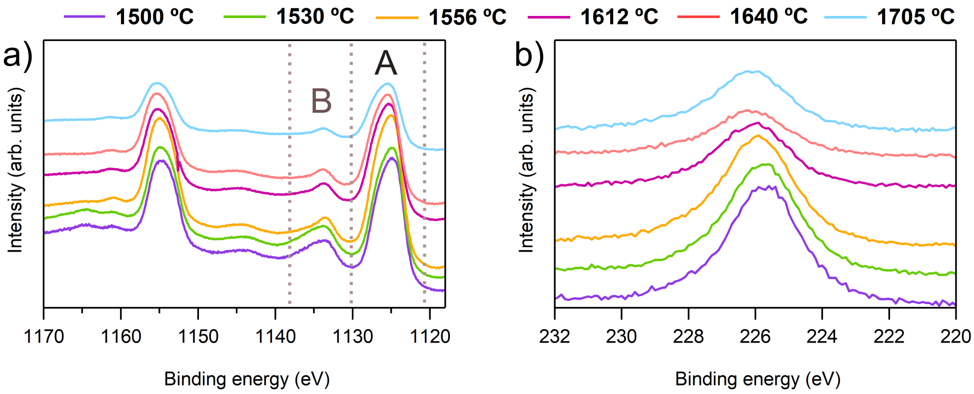

Figure 4.8: XPS spectra of 11 nm thick EuS films on SiO_2 deposited with variable sublimation temperature at a) Eu $3d$ and b) S $2s$ core levels.

Since the aforementioned differences in the spectra are subtle, it is difficult to quantify the chemical changes just by observing the figure. In order to do so, an alternative representation for the chemical composition data was performed. The XPS Eu $3d$ spectra were normalized to the area of the corresponding S $2s$ peak, and a Shirley background was subtracted. Then, the evolution of the Eu $3d$ peaks as a function of the sublimation temperature was plotted as a colour scale graph. Thus, in Fig. 4.9a, the x axis corresponds to the binding energy (in eV), the y axis is the sublimation temperature and the z axis represents the intensity of the Eu $3d$ spectra. The main Eu_{2+} peaks at the Eu $3d$ XPS spectra become more intense as the sublimation temperature increases, meaning that the amount of europium grows with respect to the sulphur for higher temperatures. To have a more accurate estimation of this effect, the ratio Eu:S was calculated with Eq. 4.1:

$$Ratio(Eu:S) = \frac{\frac{A}{SF}|_{(Eu3d)}}{\frac{A}{SF}|_{(S2s)}} \tag{4.1}$$

In this formula, the area of the peaks is normalized to the sensitivity factor, S.F., a coefficient that depends on the angle between the X-Ray gun and the detector and the cross section and the inelastic mean free path (IMFP) of the electrons of a given element in a defined energy level. Hence, for a given angle between the X-ray gun and the detector, this parameter is unique for each transition and element, being in this case 14.00 for Eu $3d_{5/2}$ and 1.44 for S $2s$ [85]. The tendency, displayed in Fig. 4.8b, is clear: the amount of Eu with respect to S increases with the sublimation temperature, doubling from around 0.7 for 1500 °Cto≈1.4 for 1700 °C. Note that the error in the estimation of the ratio Eu:S from the XPS data is ≈20-25 %. The sample deposited with highest sublimation temperature has a Eu:S ratio of 1.4, 40 % higher than the nominal value for EuS.

In addition, the evolution of the percentage of Eu^{3+} phase was extracted from the XPS spectra. The Eu $3d$ XPS peaks were deconvoluted, in the same manner as displayed in the example spectra in Fig. 4.6. However, as previously discussed, it is difficult to establish a proper relation between Eu^{2+} and Eu^{3+}, since the peaks located at a binding energy of ≈1163.03 eV and ≈1134.03 eV come from two contributions: the Eu^{3+} main peak and the satellite peaks of the Eu^{2+}. The analysis of the data is not accurate enough to give an exact proportion between the two phases, because the area of the two contributions inside this peak strongly depends on the fitting parameters. For that reason, and taking into account that the shape of B peak in Fig. 4.8 differs between the light blue curve and the rest, it will be assumed that at the highest temperature the contribution from Eu^{3+} phase is negligible and, therefore, the peak B comes exclusively from the satellite peaks of Eu^{2+}. Subtracting the peak B from the light blue curve to the rest (after imposing that all the Eu $3d$ curves have the same area), and dividing by the area of Eu $3d_{3/2}$, the proportion of Eu^{3+} phase is estimated. The results are presented in Fig. 4.9 c, where a Eu^{3+} phase percentage about 1-2% is observed, with a slight trend to decrease.

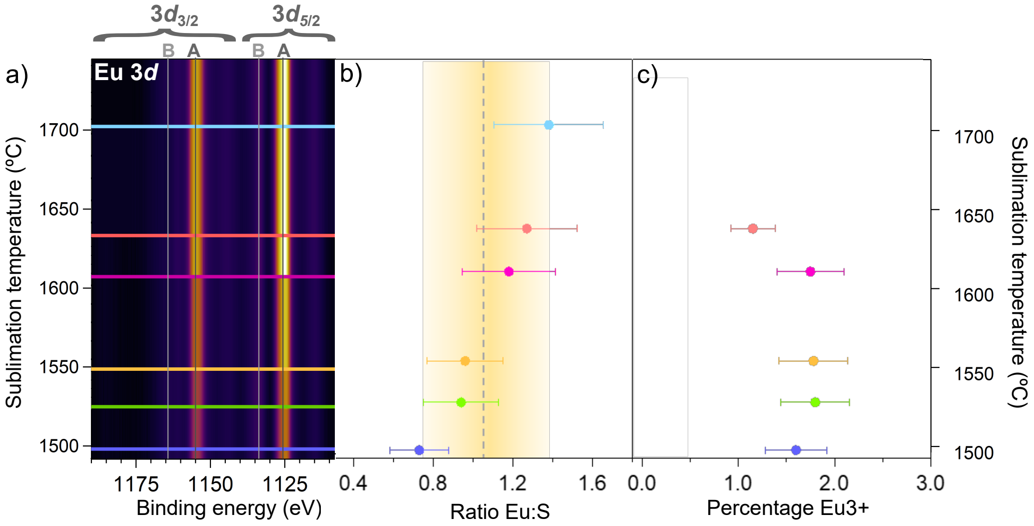

Figure 4.9: XPS study of the chemical composition of an EuS 11 nm thick layer with variable sublimation temperature. a) Evolution of the Eu $3d$ peaks (normalized to S $2s$) with the sublimation temperature. b) Ratio between Eu and S, extracted from the areas of the XPS and calculated with Eq.4.1. c) Ratio between Eu3+ and Eu2+ oxidation states. The error of XPS data is assumed to be ±20 %.

The poor reproducibility of the tunnel junctions that will be presented in next chapter motivated this study. Now that it has been shown that the material changes when the sublimation temperature varies, the impact of this change in the magnetic properties has to be checked. These magnetic properties were first explored via a combination of *ex-situ* techniques, as ac-susceptibility and VSM. All the samples were covered with 7 nm CaF_2 protective layer, to prevent the oxidation of the EuS, which has been proven to be sensitive to the presence of oxygen. A small piece of the sample was cut and introduced in a PPMS machine. Fig. 4.10 contains the main results of the experiments done for the magnetic characterization.

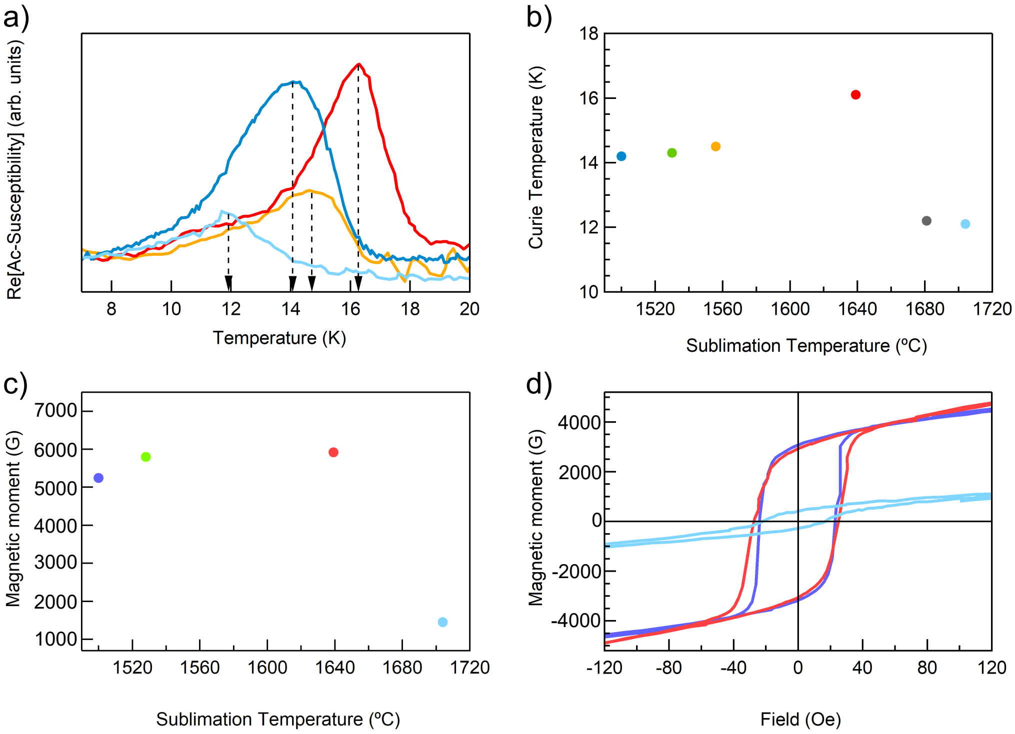

Figure 4.10: Dependence of the magnetic properties of EuS on the sublimation temperature: a) real part of the ac-susceptibility, under an applied field of ≈ 1 Oe, b) Curie temperature extracted from the ac-susceptibility measurements, c) magnetic moment at 200 Oe and 5 K and d) magnetization loops measured via VSM at 5 K.

In order to determine the Curie temperature of the thin EuS layers, the susceptibility was measured under an ac-signal. The measurements were done recording the XXXXX at a temperature range between 5 and 20 K. and the results of the real part, as a function of the sublimation temperature, are displayed in Fig. 4.10 a. Although the imaginary part of the signal tends to be more sharp, in this case is more noisy, thus, the real part was selected to extract the Curie temperature from. The maximum in these curves corresponds to a transition from ferromagnetic to paramagnetic material, i.e. the Curie temperature of the layer. The extracted value of T_C was represented as a function of the sublimation temperature in Fig. 4.10b. It can be observed a tendency to increase the Curie temperatures with the sublimation temperature, reaching a maximum in T_C of ≈17 K for a sublimation temperature of 1640 ℃, and subsequently, a decrease until ≈12 K for higher sublimation temperatures.

The magnetic moment from the VSM measurements measured with a 200 Oe parallel applied field, at 5 K, is shown as a function of the sublimation temperature in Fig. 4.10c. The moments were measured in emu and converted to G by means of the volume of the piece introduced in the PPMS. The same behaviour as for Curie temperature is observed, an almost constant value for the magnetic moment at 200 Oe around 6000 G is observed for all the samples, until the sublimation temperature reaches the highest value (light blue dot), exhibiting a moment of ≈1500 G.

The magnetization loops (Fig. 4.10 d) were obtained by VSM, at 5K, with a sweeping parallel applied field of ± 200 Oe. It can be observed that for sublimation temperatures between 1500℃ and 1650℃ (dark blue and red loops), the changes in the response of the magnetization to the applied field are negligible: both curves show a coercive field of ≈24 Oe, with a squared shape typical from a ferromagnetic material. For the sample grown at the highest sublimation temperature (light blue), the magnetic moment is lower, almost six times smaller, and the shape is less squared. However, these values are far from the moment for bulk EuS of ≈16050 G[1] and, moreover, the films need high fields, around a few Tesla, to saturate.

This result could be attributed to the existence of a different phase of Eu. Therefore, XMCD measurements were carried out at Boreas beamline, in ALBA synchrotron. A 5.5 nm thick layer of EuS, was measured at 2 K, under two different geometries, normal incidence (NI) and grazing incidence (GI), under an applied magnetic field ±6 T, recording the dichroism at the Eu $M_{4,5}$ edge (normalized to pre-edge), as displayed in Fig. 4.11, showing a saturation magnetization of about 7 μ_B, as predicted theoretically.

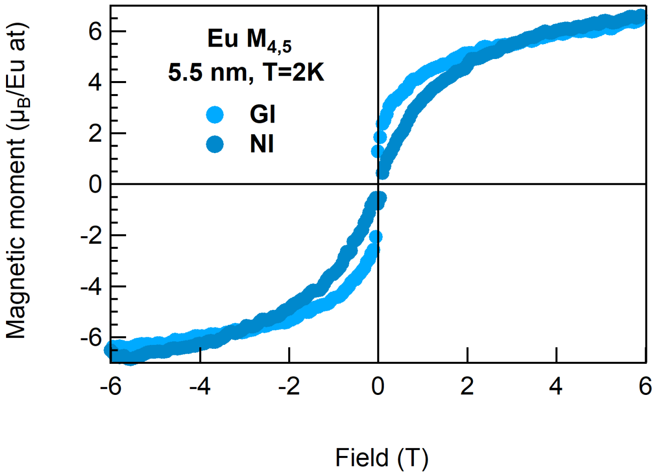

Figure 4.11: Magnetization loops of EuS at the Eu $M_{4,5}$ edge, for a 5.5 film of EuS, at 2 K, for two different geometries: grazing incidence, GI (70°, light blue) and normal incidence, NI (0°, dark blue).

The main difference in the results from VSM and XMCD is that VSM accounts for the magnetic response of the sample, while the loops measured in XMCD are element-specific. From the comparison of the loops from both techniques it can be concluded that Eu is in the proper phase, exhibiting a saturation moment ≈7 μ_B/Eu atom, but the moment of the layer is reduced with respect to the reported value for

---

[1] Value calculated from the nominal 7 μ_B/Eu at

the bulk. It implies that the polycrystalline EuS film includes a certain amount of superparamagnetic grains, weakly coupled to the main film. The relatively small value of the coercive field corroborates this observation. Indeed, for the magnetization reversal dominated by the domain walls movement, the coercive field increases with the size of the magnetic irregularities. Therefore, fine polycrystalline structure results in lower coercive fields[86]. Comparing the magnetization loop presented in Fig. 4.10d with the data reported in Ref. [86], it is clear that the coercive field in these samples is similar to the coercive field of thin EuS films grown at 77 K which were found to have grains with 4.4 nm diameters. Since EuS has no magnetocrystaline anisotropy, it is reasonable to expect very low values of the blocking temperature for the small superparamagnetic grains [87]. In the PPMS, it was not possible to measure the magnetization loops below 1 K. However, since the EuS films were implemented in tunneling junctions (more details in next Chapter), as shown in Fig. 4.12. The dependence of the bottom Al layer's resistance interfaced with EuS film on the magnetic field provides indirect confirmation of this conjecture.

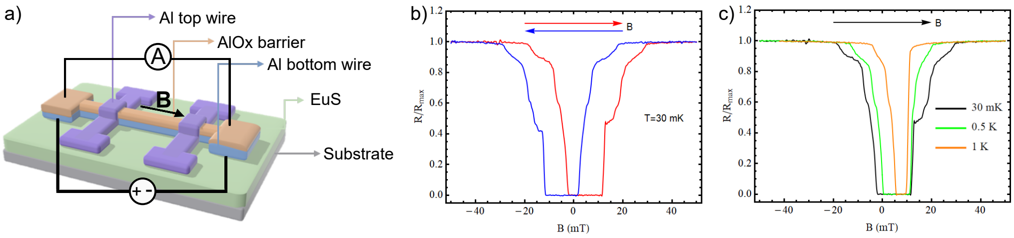

Figure 4.12: a) Schematic representation of the tunneling junction used to study the magnetic response of EuS at 30 mK, via the dependence of the resistance of the Al bottom layer on the applied magnetic field. The stacking structure is CaF2 (7 nm)/Al(12 nm)/AlOx(5 nm)/Al(12 nm)/EuS (16.5 nm)/substrate. The configuration to measure along the bottom Al wire is included. b) The hysteresis of the resistance of the Al wire adjacent to the EuS layer at T=30 mK. c) The B-field dependence of the resistance of the Al wire adjacent to the EuS layer at different temperatures (30 mK, 0.5 K, 1 K).

At 30 mK, all superparamagnetic particles are in the blocked state. The R vs B curve shows distinctive jumps that can be interpreted as the magnetization reversal of the components with different magnetic anisotropy (Fig. 4.12). If the exchange coupling between the grains is weak, the orientation of their magnetic moments depends on the dipolar interaction with the rest of the film and with the coupling with the external field. Whereas the external field will try to align the particles' moment, the dipolar interaction tries to orient their moment in the direction opposite to the magnetic moment of the film. Considering a descending branch of the resistance (red curve in Fig. 4.12), it can be observed that all the moments are aligned at a high positive field, and the effective exchange field is high (no superconductivity). When the field decreases down to zero, the dipolar interaction dominates. The resistance decreases in steps that correspond to consecutive switching of the magnetization of the superparamagnetic particles. The average magnetic moment becomes smaller and leads to a decrease in the effective exchange field. This decrease allows the Al wire to become superconducting. The zero-resistance state remains up to small negative values of the field. Further increase of the negative magnetic field leads again to consecutive reversal of the particles' magnetic moments accompanied by the switching of the total magnetic moment. The effective exchange field is large again and quenches superconductivity. This gives rise to the increase of the resistance. The same measurements performed at a higher temperature (Fig. 4.12 c) show that the critical fields corresponding to the reversal of the superparamagnetic particle progressively disappear, showing the transition to the unblocked state.

4.2.3 The contribution of the interface EuS/InAs

Beyond the monolayer regime, more specifically in the nanometer range, as the samples studied in this chapter, the magnetic properties such as Curie temperature, coercive field or magnetic moment are independent of the thickness. Nonetheless, a 5 nm-thick interface between EuS and InAs was found (Section 4.1). This interlayer may exhibit a different magnetic behaviour with respect to the ordered EuS. In the present section, the impact of the interface EuS/InAs in the magnetic properties will be studied. For that, EuS layers of variable thickness, ranging from 2 to 20 nm, were grown on InAs(100), all at a similar sublimation temperature (≈1600 °C).

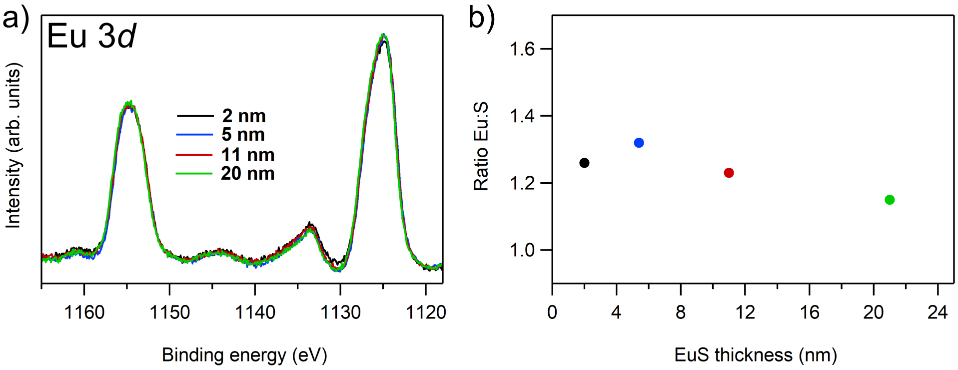

Figure 4.13: Chemical composition of EuS thin layers with variable thickness (from 2 to 20 nm). a) XPS spectra at Eu $3d$ core level, normalized to the area of this peaks. b) Calculated ratio Eu:S, calculated from the Eq.4.1, from the areas of Eu $3d$ and S $2s$, normalized to In $3d_{5/2}$, as a function of the thickness.

The chemical composition was measured by XPS *in situ*. As can be observed in Fig. 4.13 a, all the Eu $3d$ core level spectra present the same peaks, with the same proportion between them (note that the spectra have been normalized to 1 for a better comparison). This indicates that apparently all compositions are very similar, and that the In interdiffuses on the EuS, as discussed in Section 4.1. With respect to the ratio Eu:S, calculated from Eq. 4.1, the proportion between the two elements remains almost unchanged, taking into account the error from the analysis of the XPS spectra, being close to the expected 1:1 ratio for stoichiometric EuS.

Once the chemical composition has been proven to be constant in this series of samples, they were covered with an Al layer of ≈7 nm, to prevent the oxidation of EuS, and taken out the chamber to measure the magnetic properties via VSM and ac-susceptibility. In Fig. 4.14a the comparison of the magnetization loops measured via VSM is presented. The magnetic moments are normalized to the corresponding saturation magnetization (M_S). All the loops exhibit a shape compatible with a ferromagnetic material. The main difference between them is the coercive field, that increases with the thickness, ranging from 0.8 to 2.3 mT, when the contribution from the interface is overcome.

The Curie temperature was extracted from the ac-susceptibility, as in the previous section, and represented in Fig. 4.14b. It can be observed that the transition temperature grows with the thickness, tending to a constant value around 24 K, for the thickest sample. The results from both techniques confirm that the interface has an impact in the magnetic behaviour of EuS, shrinking the coercive field and the Curie temperature.

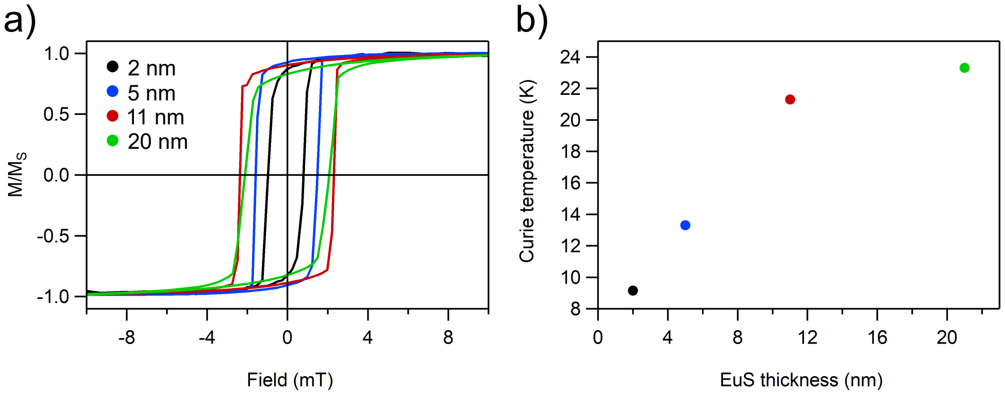

Figure 4.14: Magnetic properties of EuS as a function of the thickness. a) Magnetization loops at 5 K. b) Curie temperature.

Moreover, it is noticeable that the Curie temperature is higher for EuS/InAs bilayer than for EuS/SiO_2. To compare these results, the growth parameters have to be the same, so the samples to compare are the 11 nm EuS deposited at 1600 °C. Their Curie temperatures are 22 K for EuS/InAs and 16 K for EuS/Si_2, accounting that the ordering of the layer helps enhance the transition temperature.

The impact of the interdiffusion of In atoms into the EuS layer in the magnetism of this ferromagnetic insulator is also visible in the XMCD measurements. Fig. 4.15 shows the comparison of the magnetization loops of thin films of EuS on InAs, with two different thicknesses: one above the interlayer (5.5 nm) and the other, below (1 nm). The values of the magnetic moments, extracted from the sum rules analysis of XMCD spectra are presented in Table 4.2.3.

Since the samples were measured at different values of the applied field, to make a proper comparison between the magnetic moments, the values at H=3 T were extracted from the normalized magnetization loops of Fig. 4.15, and collected in Table 4.2.3, where a decrease of about 20-25% is observed for the thinnest sample.

Table 4.1: Coefficients from sum-rules analysis (r, p, q) to calculate the magnetic orbital moment (m_L), the spin magnetic moment (m_S) and the total moment, as a function of the thickness of EuS.

Thickness	**Conditions**	**Coefficients**			**Magnetic moment (μ_B/Eu atom)**		
		r	**p**	**q**	**mL**	**mS**	**Total**
5.5 nm	NI; 6 T	69.1	-27.5	-13.2	0.9	5.7	6.6
	GI; 6 T	86.5	-33.4	-14.9	0.8	5.7	6.5
1 nm	NI; 3 T	8.4	-2.5	-1.1	0.6	4.4	5.0
	GI; 1 T	8.0	-1.2	-0.6	0.4	2.1	2.5

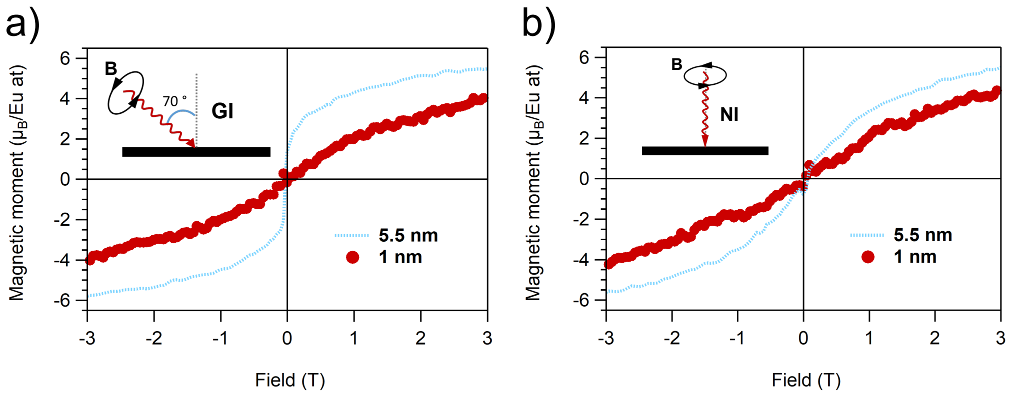

Figure 4.15: Comparison of the magnetization loops at the Eu $M_{4,5}$ energy, for EuS thin layers with variable thickness.

Table 4.2: Total magnetic moment (μ_B/Eu atom) extracted from magnetization loops in Fig. 4.15, for two different thicknesses.

Thickness	**Geometry**	**Magnetic moment (μ_B/Eu atom)**
5.5 nm	NI	5.5
	GI	5.5
1 nm	NI	4.4
	GI	4.0

Summary

In this first experimental chapter, by a combination of in-situ and ex-situ techniques, a structural, chemical and magnetic characterization of EuS thin layers was performed. First of all, the epitaxial growth of EuS on InAs at room temperature was shown. The substrate was prepared in ultra high vacuum, leading to an In-terminated surface. After the deposition of EuS, an interface of ≈5 nm appears, due to the diffusion of In atoms in the first EuS layers. Beyond this thickness, epitaxial growth of EuS is obtained.

Moreover, the importance of controlling the parameters during the evaporation of EuS has been highlighted. Working in ultra high vacuum, the desired Eu 2+ phase is deposited, while increasing the pressure to 10^{-7}-10^{-6} mbar the presence of Eu with 3+ oxidation state increases, as demonstrated via XPS. The sublimation temperature also plays an important role: observing a trend to Eu-richer phase for higher sublimation temperatures. This change in the chemical composition is reflected in the magnetic properties, with an increment in the magnetic moment and Curie temperature until a critical point (≈1650 ℃) is reached. From the VSM measurements, a magnetic moment $\sim \frac{1}{3}$ of the reported value for bulk EuS is found. The magnetic moment per Eu atom was measured via XMCD, with a saturation moment about 7 μ_B/Eu atom, as expected, confirming thus the presence of a superparamagnetic phase, as indicated via tunneling spectroscopy. The aforesaid interlayer between EuS and InAs has been shown to be less magnetic, with lower Curie temperature and magnetic moment.

This complete study of the evaporation of EuS thin films and the impact of the growth parameters on the chemical, structural and magnetic properties of the layers will enhance the applicability of EuS in devices, as presented in the following two chapters.

Chapter 5

Engineering the spin-split density of states in superconducting Al for spin-dependent tunneling devices

Once the properties of EuS and their dependence with the preparation conditions have been studied in detail, this ferromagnetic insulator can be implemented in devices.

As introduced at the beginning of this manuscript, this Thesis has been developed in the framework of the SUPERTED project [5] (Funding from the European Union's Horizon 2020 research and innovation program, grant agreement No 800923), which purpose is to develop a radiation sensor based on the giant thermoelectric effect predicted theoretically by A. Ozaeta and coworkers[6]. For the giant thermoelectric effect to occur, two conditions have to be fulfilled: the spin-splitting density of states of the superconductor and the spin filtering of the current through an insulating barrier. Despite several groups have shown the spin-splitting, only the group of Dr. J. Moodera has reported this effect in the absence of magnetic field[12, 88]. However, a detailed study on the conditions of the growth of the different layers, their chemical and structural characterization, and their impact in the properties still was undone.

From a surface science approach, this Chapter consists in the detailed study of the fabrication of the junctions, layer by layer, focusing mainly in the interface superconductor/ferromagnetic insulator and the insulating barrier, and the impact of the preparation conditions and properties of the elements on the performance of the devices, tested via tunneling spectroscopy.

5.1 The basis of the giant thermoelectric effect

Prior to discuss about the characterization of the materials and the devices, a short introduction to the giant thermoelectric effect has to be done. As already mentioned, there are two ingredients that lead to this effect:

i. The spin splitting of the density of states (DoS) of the superconductor. When a superconducting material is in the presence of a magnetic field, a broadening

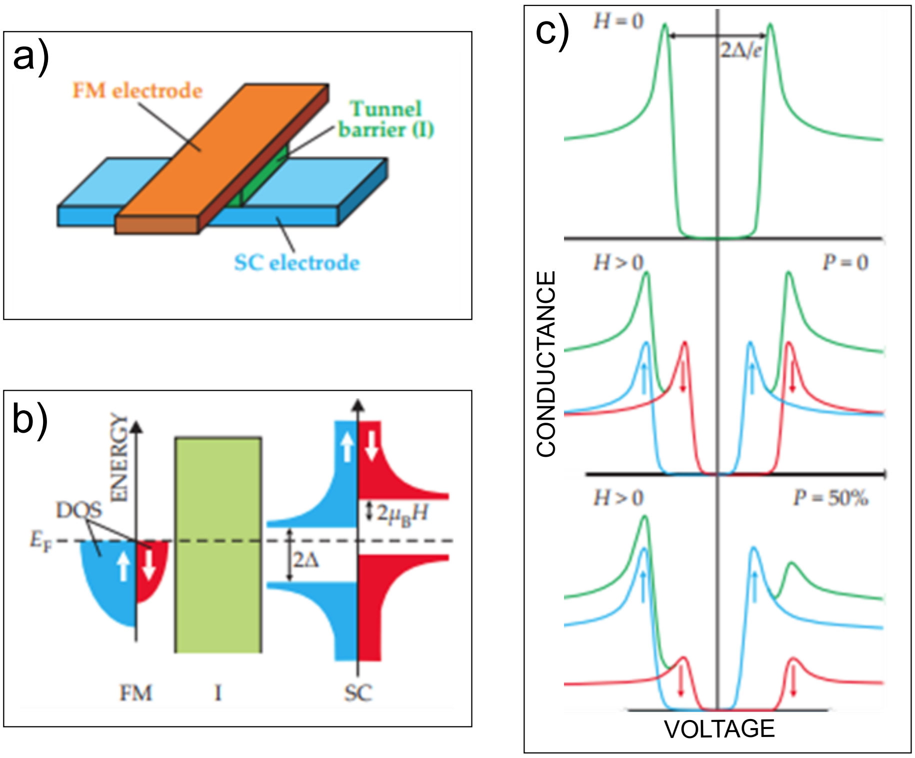

Figure 5.1: a) A tunnel junction consisting on an insulating barrier separating a ferromagnetic electrode and a superconducting electrode. b) Density of states of the FM and the SC, separated by the insulating barrier. On the left, the ferromagnetic, presenting a conduction band with uneven population of spin-up (blue) and spin-down (red) electrons at the Fermi level, that tunnel through the insulator (green). On the right, the energy gap (2Δ) in the DoS of the superconductor and the Zeeman splitting ($2\mu_B$H) in an applied magnetic field H. The tunneling spin polarization P is defined as the ratio of the relative number of up and down spin-polarized carriers (weighted by their mobility) to their total number. c) Tunneling conductance (green) as a function of bias voltage across the electrodes. At H = 0 (top), the conductance reveals only the SC energy gap. In an applied field, the Zeeman splitting lifts the degeneracy between the spin-up and spin-down states. If the counterelectrode is a normal metal (P = 0), the spin-up and spindown peaks are of equal strength (middle plot). In the case of a ferromagnetic counterelectrode (bottom), the nonzero spin polarization of tunneling electrons turns the conductance asymmetric[89].

of the DoS is observed, due to the orbital depairing. However, for Al thin films with parallel applied magnetic field, a spin splitting of the Bardeen-Cooper-Schrieffer (BCS) density of states has been reported[90]. It is the so-called Zeeman splitting, being the energy difference between the splitted peaks 2μH, μ the moment of the electron and H the applied field. The demonstration is simple: the Cooper pairs conserve their moments (k↑, -k↓) even in presence of an external magnetic field, but one is increased by μH and the other, decreased by -μH. The excited states remain separated from the paired states by Δ, so that in a tunneling measurement of the DoS, the peaks for different spin polarization appear at different values of the voltage. In Fig. 5.1 c, in the central pannel, the resulting DoS is shown. This effect has been confirmed by several experiments, even at zero field, by placing a ferromagnetic insulator material in contact with the superconductor. A combination of materials SC/FI that reported good results is Al/EuS [12, 91, 92]. In this case, the Zeeman splitting occurs due to the interfacial exchange interaction between the localized magnetic moments in the ferromagnetic insulator and the electrons in the conduction band of the superconductor.

ii. The spin filtering of the current through the insulating barrier. With the aim to create a net spin-polarized current through the barrier, an imbalance between the spin-up and the spin-down components has to be produced. Introducing a ferromagnetic material as the counterelectrode (as in Fig. 5.1 a) or as the barrier, its band structure is splitted by an amount called exchange energy, and the probability of tunneling the barrier changes for each polarization, as represented in Fig. 5.1 b) and the bottom panel of Fig 5.1 c).

In particular, in the project the proposed FI/Al junction to develop the sensor was based on EuS as FI and Al as Superconductor. In this chapter I will present the results on the implementation of the ferromagnetic insulator EuS thin films studied in the previous chapter (4) in heterostructures together with superconducting materials to produce a superconducting detector. I will present a detailed study on how the properties of the materials that take part of the devices can be tuned by modifying the growth conditions, and how this is reflected in the performance of the devices. For that, a combination of surface science techniques and tunneling spectroscopy measurements will be carried out.

5.2 Detailed preparation of the devices

Tunneling junctions as the represented in Fig. 5.2 were fabricated to measure the I-V curves via tunneling spectroscopy in a four probe configuration. Those junctions consist on a superconducting electrode, in contact with a ferromagnetic insulator and, in turn, separated from a ferromagnetic counterelectrode by a thin insulating barrier. The width of the electrodes is 200 μm. In this case, to increase the number of junctions to test and double check the results, the ferromagnetic top layer consists in two parallel wires, giving rise to two junctions in each device. The superconducting electrode and the ferromagnetic counterelectrodes present the same Fermi level at absence of any applied voltage. However, when a voltage is applied to one electrode, some current can flow through the barrier and reach the other electrode. The magnitude to measure is the current (or its derivative) as a function of the applied voltage. The set up for the four probe method is also displayed in the figure.

The first experiments, prior to develop the radiation detector with an spin-filtering junction, focused on demonstrating the spin-splitting of the devices and controlling the fabrication of the EuS/Al junction, as well as the insulating barrier, made out of AlOx. Hence, the first devices that we investigated were Al/AlOx/Al/EuS/silica.

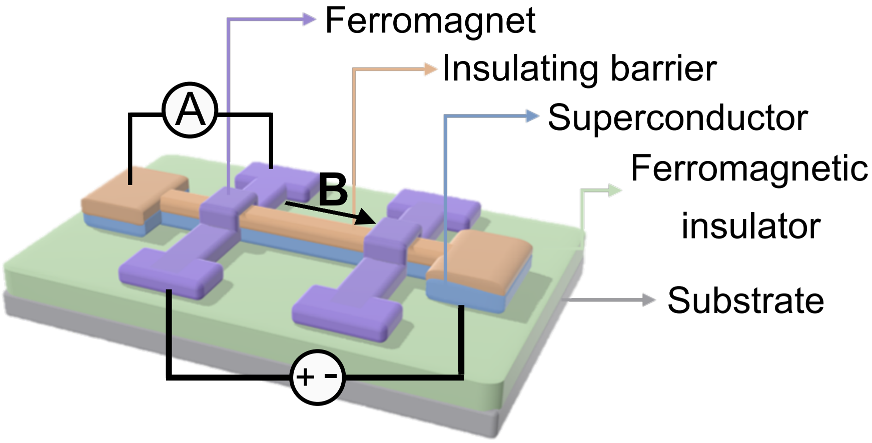

Figure 5.2: Schematic representation of the devices based on ferromagnetic insulator/superconductor junctions and the four probe tunneling spectroscopy measurement.

Once we understood how to relate the fabrication parameters and the tunneling spectroscopy curves, we moved to devices with spin-filtering, being Co/AlOx/Al/EuS/substrate, the combination of materials to probe.

All the employed substrates (SiO_2, silica, SiN) were cleaned *ex situ*, following the same routine: three minutes of ultrasound bath in acetone, three minutes of ultrasound bath in isopropanol and dried in N_2.

EuS continuous layers were evaporated from the stoichiometric powder as described in the previous chapter, and the deposition rate and chemistry were controlled to ensure the reproducibility of the results. Thanks to the understanding of the chemical changes in EuS due to the sublimation temperature, studied in the previous Chapter, it is possible to tune the exchange coupling strength superconductor/ferromagnetic insulator, via the control of the sublimation conditions of the latter, being one of the most relevant results of this work.

Once the EuS layer is deposited on the substrate, the Al electrode has to be produced. In the early works of Meservey, Tedrow and later of Moodera and coworkers, the *in situ* shadow mask evaporation was used to create the crossed-wire tunneling junctions in the high vacuum environment (10^{-8} mbar)[91, 93]. Although this method is simple and efficient, it did not allow to make the junctions smaller than $200{\times}200\ \mu m^2$ and was less convenient for developing more complex structures. Therefore, various attempts of lithography based nanofabrication were used to create the devices with exchange split DoS, especially based on the combination of Al and EuS. It was shown that the exposure of EuS to atmosphere before the deposition of the superconductor, occurring during the lithography process, does not allow maintaining the exchange splitting without external magnetic field even after the initial saturation of the magnetization below the Curie temperature of the EuS [94, 95]. These results imply that EuS was partially oxidized during the lithographic nanofabrication, which causes formation on the interface of the paramagnetic Eu-based compound with zero magnetic remanence. For this reason, the shadow mask evaporation was chosen as the method to deposit the aluminum electrode. In Chapter 2, more details about the preparation chamber and shadow masks can be found.

Next, the aluminum electrode was partially oxidized in oxygen plasma, with a pressure of 4 10^{-3} mbar and a power supplied to the cracker source of 180 W, enough to produce an AlOx barrier with a resistance on the order of the dozen of Ω in 5 h. More details on the plasma calibration process are given in Chapter 5.3.

Next step is the growth of the two parallel top metallic wires, that will act as counterelectrodes. They were made of Al or Co. Independent of the deposited material, evaporation through shadow mask was done. For Co evaporation, an e-beam evaporator was used, sublimating Co from a rod with 2 or 3 mm of diameter.

Before taking the samples out of the UHV chamber, the whole device was covered with a transparent, insulating material: CaF_2, with 7 nm thickness, to prevent the oxidation of the device, but allow for the measurement via tunneling spectroscopy.

The process followed after the optimization of all the layers is summarized in Fig. 5.3.

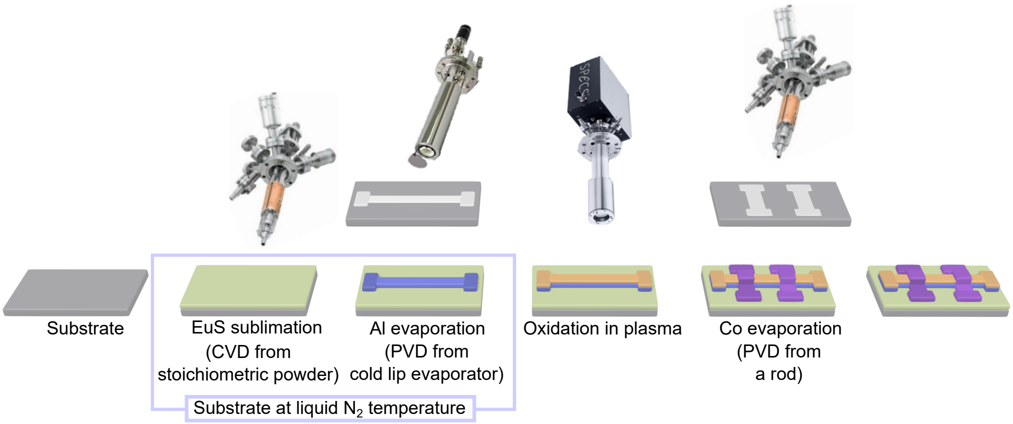

Figure 5.3: Schematic representation of the growth of the devices.

5.3 The insulating barrier: oxidation in plasma source

The operation of the devices that have come up with the recent development of quantum technologies[96–106] is based on Josephson junctions (JJs), magnetic tunnel junctions (MTJs) or metal-insulating-metal junctions in general, where a usual choice for the metal is Al, and for the insulator its oxide, AlOx. Although oxidation of Al has actively been explored over years[107–112], in the last decades the interest in this topic has increased, since the performance of such devices is affected by the tunneling through the oxide barrier[113–117], which depends on the barrier characteristics. Likewise, the uniformity of the oxide thickness and the quality of the oxide-metal interface are the most important factors which define the functionality of the AlOx barrier[118–120].

The fabrication procedure of the barrier determines its characteristics. The traditional method to grow the AlOx barrier is thermal oxidation, where aluminum is directly exposed to air (or pure molecular oxygen), at high temperature or even at room temperature. Some studies reveal that the first layers of oxides grown by thermal oxidation are amorphous, leading to a disordered interface, that can affect the final properties of the device[121]. During oxidation with molecular oxygen, subsequent processes take place: first, O_2 molecules adsorb in the substrate surface, then their bonds break and at the end, oxygen atoms penetrate into the sample. Theoretical calculations predict maximum oxide thickness of around 2 nm using molecular oxygen due to the decrease in adsorption energy of oxygen molecules[122].

Among alternative methods to produce tunnel barriers, the most popular is radio frequency plasma oxidation, that employs atomic oxygen for producing both thin and thick barriers in real short times[123]. Despite the reduction of the oxidation time can be considered as a advantage, the shorter the time is, the less control of the thickness. In addition to this inconvenience, this is an aggressive technique, where the oxygen atoms that arrive to the sample have high kinetic energy, giving rise to defects.

Low defect barriers are obtained by atomic layer deposition (ALD)[124], where volatile materials, called precursors, arrive to the surface, chemisorb and react producing the desired material[125]. However, the majority of ALD systems work in relatively high pressure (0.1–10 mbar), which implies the emergence of contaminants at the interfaces.

In this thesis, the selected method for the barrier fabrication was microwave plasma oxidation. Unlike radio-frequency plasma, times are longer and the oxygen atoms energy is lower thus, the oxidation is easier to control and the barrier presents less defects. The advantages of the proposed method are: 1) feasibility of obtaining thicker barriers than those obtained by thermal oxidation; 2) manage to obtain high quality tunnel barriers compared to those obtained by other plasma treatments; 3) the possibility of doing this in a highly controlled environment, compatible with ultra high vacuum[126].

Following the work methodology shown in the previous chapter, the first experiment carried out was the study, by XPS, of the chemical composition of the barrier to relate the exposure time to plasma with the thickness of the barrier. With that in mind, Al layers with ≈10 nm thickness were grown on silica and exposed to plasma oxygen for different times (1, 4.5 and 8 hours). The XPS spectra at the Al $2p$ and the O $1s$ core levels were measured before and after the oxidation and represented in Fig 5.4.

The Al 2p core level of the as deposited layer, centered at 72.2 eV can be fitted using 2 components, which corresponds to the two spin-orbit splitting components of the 2p core level[127]. With subsequent oxidations, this metallic component, decreases, while a component, associated with oxides grows. This component shifts from 75 eV to 74 eV with increasing oxidation time. The same increment of the oxide is measured for the O 1s core level. The O 1s core level was fitted using two component, one in the range of 530.5-531.3 eV, attributed to the oxide and another one at higher BE associated with chemisorbed oxygen, which does not bond to aluminum. This contribution has been assigned to contamination surface species, such as OH^- or O_2^{2-}[128, 129]. The small signal detected on the as deposited Al layer around the O 1s core level comes from the SiO_2 substrate. The proportion between

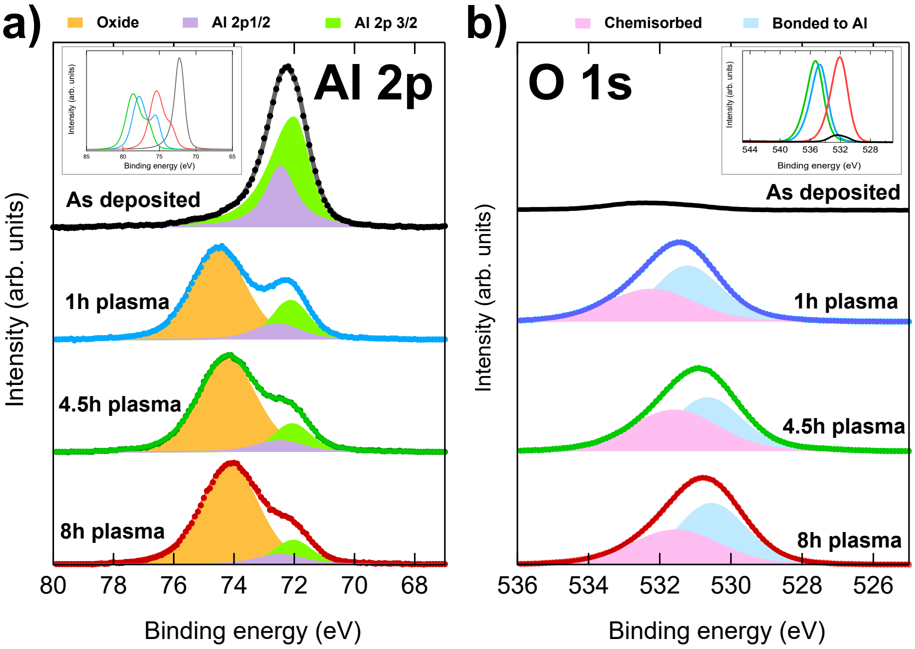

Figure 5.4: XPS spectra and fitting components at the energies of a) Al *2p* core level and b) O *1s* core level, before and after different exposure times to plasma oxygen.

Al and O was calculated in also the cases, with Eq. 4.1, with a sensitivity factor of 0.234 for Al 2p and 0.711 for O 1s, finding an Al:O ratio ≈0.56 %, which is in the error range of 20 %. It is important to mention here that the Al 2p core levels measured on the plasma exposed samples and shown in Fig 5.4 were rigidly shifted to maintain the metallic Al component aligned to the as deposited one. The same energy shift was imposed to the O 1s core level. The uncorrected spectra are shown in Fig. 5.4 as insets. The 1h and 4.5h oxidation time spectra show a progressive rigid shift due to a change in the workfunction, meaning that the sample is more insulating when the plasma exposure time increases, as expected. Surprisingly, the 8h oxidation time exhibits a lower shifting than expected. This is because, in XPS experiments, the measured states are excited states. If the oxide layer is thick, the screening process is slower, and the excited state that is measured has not decayed totally to the initial state when it is excited again[130].

To compare the oxidation via oxygen plasma with molecular oxidation in atmosphere an Al layer was exposed to air during 12 hours. The XPS spectra at Al 2p and O 1s core levels of this sample were measured and represented together with the spectra for the samples exposed for short times to oxygen plasma in Fig.5.5.

The oxidation in atmosphere during 12h produced a bigger oxide contribution in Al 2p, as well as higher O 1s peak, than short times in oxygen plasma (5-15 min), while 1 hour under oxygen plasma was enough to exceed the oxidation.

The average thickness of the AlOx barrier can be calculated from the ratio between the metallic and oxidic contributions in the Al 2p XPS, by means of the Strohmeier equation[107]:

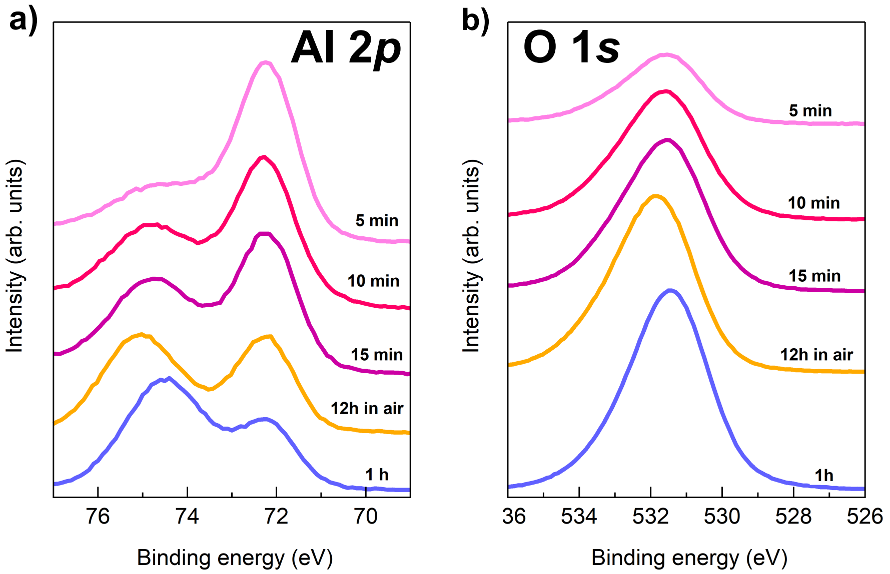

Figure 5.5: XPS spectra at the a) Al $2p$ core level and b) O $1s$ core level, for short times in plasma (5 min, 10 min, 15 min and 1h) and 12h exposed to air.

$$d_{ox}^{XPS} = \lambda_o \; sin\theta \; ln\left[\frac{N_m\lambda_m}{N_o\lambda_o}\frac{I_o}{I_m}+1\right] \tag{5.1}$$

The only parameters introduced in Eq 5.1 that changes from one to another case are the areas of the metallic and oxidic contributions to the Al 2p peak, I_m and I_o. The inelastic mean free path (IMFP) values were calculated with the TPP-2M method[131], with a kinetic energy of 1412 eV, resulting λ_m=3.11 nm and λ_o=3.28 nm. The ratio of the volume densities of Al atoms in metal to oxide $N_m/N_{ox} = 1.6$, was calculated using the densities 2.7 g/cm^3 and 3.1 g/cm^3 for the metal and oxide, respectively. θ=10, is the take-off angle with respect to the normal of the sample surface. Figure 5.6 shows, as blue points, the estimated thickness extracted from Eq. 5.1 as a function of the exposure time.

For thin films (< 20 nm), the kinetics of the oxidation of a metal follows the inverse logarithmic law that Mott and Cabrera established in 1949[132]. Initial linear oxidation is followed by a slow logarithmic reaction which rate depends on the oxide film crystallization to form grain boundaries. Thus, the thickness of the oxide barrier and the plasma exposition time are related as follows:

$$d_{ox} = k \; ln\left(\frac{t}{t_0}+1\right) \tag{5.2}$$

where k and t_0 are parameters to be fitted. From the fitting of the experimental data presented in Fig.5.6, the obtained values for the parameters are: k= 0.81±0.21 nm and t_0= 0.012 ± 0.016 h.

The oxide thickness extracted from XPS is an average value, but XPS gives no information about the presence of defects in the topography of the oxidized layer that can have important implications in the performance of devices. As already mentioned, when fabricating tunneling barriers for devices, defects such as pinholes or inhomogeneities can appear. Hence, for applications, the quality of the barrier, i.e. the absence of defects, has to be checked. Tunneling spectroscopy measurements in a dc four-probe setup were performed on Al/AlOx/Al/silica junctions at room temperature, as represented in Fig. 5.2. The differential conductance was evaluated via numerical differentiation of the obtained I-V curves at large bias voltage (10 μV), and the resistance of the barrier was calculated as the inverse of the conductance. The values of the resistance are collected in Table 5.1.

Table 5.1: Resistance of the barrier of the tunneling junctions.

Exposure time to plasma (h)	**Resistance (kΩ)**
1	0.1
2	4.8
2.5	8.2
3	7.7
3.5	7.3
4.5	15.4

From the extracted conductance, the effective thickness of the barrier, $d_{ox}{}^{TUN}$, can be calculated, using the linear approximation on Simmons' formula[133]. This is an analytic expression for the current density that relates the measured current-voltage I-V characteristic and the effective barrier thickness and width. If the bias voltage is big enough, as in this case, a linear behaviour is observed. The expression that relates the conductivity (G_n) with the thickness of the barrier (d_{ox}^{TUN}) is the following[112, 133–139]:

$$\frac{G_n}{S} = \frac{G_0 2\pi}{4 d_{ox}^{TUN} d_0}\, exp\left(-\frac{d_{ox}^{TUN}}{d_0}\right) \tag{5.3}$$

where S is the surface of the barrier (200x200 μm^2=4 10^{10} nm^2), and d_0 and G_0 are constants which values can be calculated from the following expressions:

$$d_0 = \frac{\hbar}{2\alpha(2m\phi_0)^{\frac{1}{2}}} = 0.18\ nm$$

$$G_0 = \frac{2q^2}{\hbar} = 4.9\ 10^{-4}\ S$$

where m and q are the electron mass and charge, respectively, α=1 is a correction function for nonlinearities and ϕ=1.835 eV[140] is the barrier height. Solving the equation introducing the value of the parameters, the expression for the thickness in terms of the conductivity is:

$$d_{ox}^{TUN}(nm) \approx 0.18\ W\left(\frac{9.5\ 10^8}{G_n}\right) \tag{5.4}$$

where W(G_n) is the Lambert function.

The comparison between the average values from XPS and the effective values of the thickness of the insulating AlOx barrier are displayed in Fig. 5.6. The difference

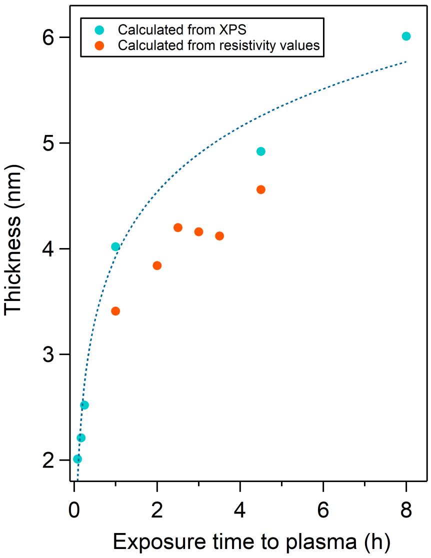

Figure 5.6: Calculated values of the barrier thickness from XPS (blue) and tunneling spectroscopy (orange) measurements. Logarithmic fitting of the XPS data (dotted blue curve).

between both thicknesses (average and effective) gives an estimation of the quality of the barrier, being better when they are more similar.

It has been demonstrated that the oxidation via oxygen plasma allows for the production of barriers with few nanometer thickness in relative short times, compared with the oxidation in air, as shown in Fig. 5.5. Although some works reported the use of acceleration voltage in the oxidation via plasma for the fabrication of magnetic tunnel junctions[141], their real short times (few minutes) represent a parameter difficult to control, decreasing the reproducibility of the barriers, in addition to the possible damages that could cause in the superconducting wire the bombardment with O ions.

Therefore, the production of the insulating barrier via the oxidation in plasma without acceleration voltage allows for uniform, few nanometer-thick barriers with resistances in the order of kΩ. Moreover, this method is compatible with UHV.

5.4 Chemical proof of intermixing layer at Al/EuS interface

The spin-splitting in the BCS density of states is due to the interfacial exchange field that penetrates the superconductor. This exchange field, as aforementioned, can be produced with an applied magnetic field, but also proximitizing the superconductor with a ferromagnet. The splitting decreases with increasing of the thickness of the superconducting film in close accordance with the predictions of the de Gennes' theory [142]. Yet, the quality of the interface is crucial to obtain reliable and reproducible amplitudes of the exchange splitting, since it has been shown that introducing a the thin insulating layer between the magnetic and the superconducting films can result in complete quenching of the exchange interaction[91, 143]. Furthermore, Al has been proven to react with chalcogenides when deposited onto them, forming compounds with the chalcogen [144].

Hence, the interface Al/EuS has to be studied in detail. For that, a 12 nm layer of EuS was grown onto a SiO_2 substrate, followed by the deposition of a 4 Ålayer of Al, and finally covered with 8 nm of Al. The sample was analyzed by XPS after each deposition. Fig. 5.7 collects the the Eu 3*d*, the S 2*s*, and the Al 2*p* core levels, showing the spectra of bare EuS in black and EuS covered with Al in light green. The 8 nm thick Al layer, in dark green, is shown as a reference.

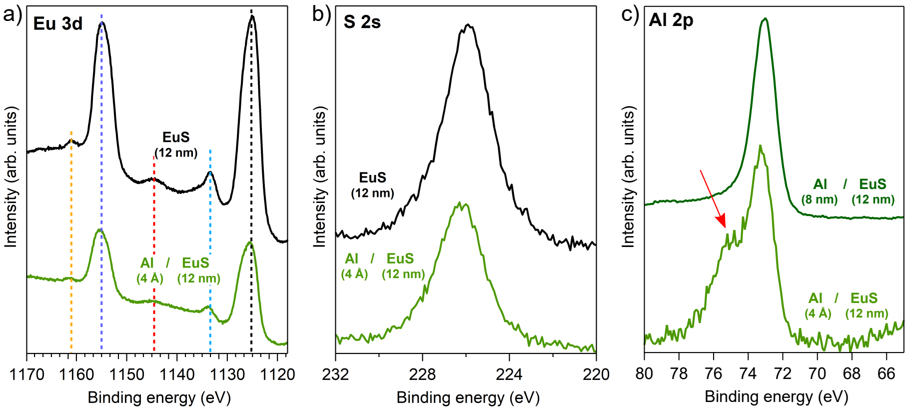

Figure 5.7: XPS spectra at different core levels for a complete layer of 12 nm EuS (black), covered with 4 $\AA$ of Al (light green) and 8 nm of Al (dark green). a) Eu 3*d* with dashed lines indicating the position of Eu 3+ 3*d* 3/2 (–), Eu 2+ 3*d* 3/2 (–), Eu 3*d* 3/2 satellite (–), Eu 3+ 3*d* 5/2 (–), Eu 2+ 3*d* 5/2 (–) and Eu 3*d* 5/2 satellite (–). b) S 2*s*. c) Al 2*p* normalized to the edge-pre edge height to observe the features. The red arrow points a secondary peak appearing at higher BE for the 4 $\AA$ Al case. As an inset, the spectra without normalization.

The Eu 3*d* and S 2*s* XPS spectra do not present any remarkable change upon deposition of the Al, except the reduction of the intensity due to the attenuation of the signal produced by the Al layer that is on top.

The Al 2*p* presents two peaks. The main one is centered at 72.2 eV and, as we discussed in the previous section, corresponds to metallic Al, as confirmed by the reference of 8 nm layer included in Fig. 5.7c). The extra peak in the Al 2*p* spectrum for thin Al layer (pointed with a red arrow in Fig 5.7 c), appears at higher binding energy, at the energy position attributed to +3 oxidation state of Al in Al_2S_3 [145]. This may be caused if some Al atoms reacts with the S atoms, leading to formation of Eu ions in the interface Al/EuS. This effect is not visible in the S 2*s* spectrum, since the EuS layer is much thicker than Al, thus the percentage of S ions bonded to Al is negligible with respect to the total amount of S.

5.5 Fabrication of spin-splitting tunnel junctions

The first tunnel junctions that were fabricated consisted in two electrodes of Al separated by an insulating AlOx barrier, and one of them proximitized by EuS, as shown in Fig. 5.8. From this series of samples, the splitting of the DoS of Al was demonstrated[146]

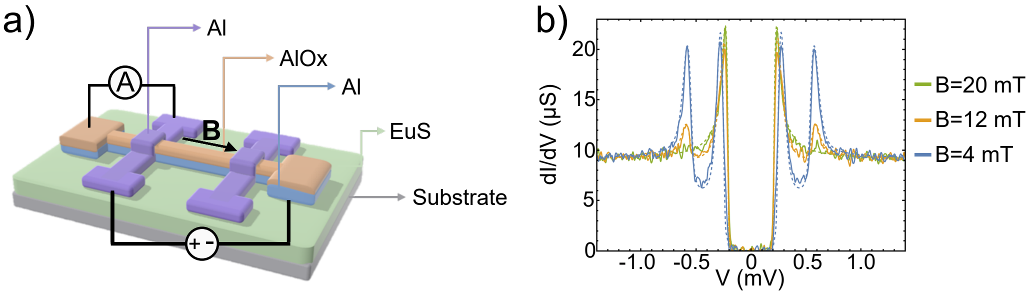

Figure 5.8: a) Schematic representation of the first tunneling junctions used to study the splitting of the density of states of superconducting Al. The stacking structure is CaF_2 (7 nm)/Al(12 nm)/AlOx(5 nm)/Al(12 nm)/EuS (16.5 nm)/silica. The four probe configuration for the tunneling measurements is included. b) Differential conductance (dI/dV) of this junction, with an in plane external magnetic field of 4, 12 and 20 mT, measured at 30 mK[146].

Although the superconducting gap of Al is predicted to be 200 μV, Fig. 5.8b shows a superconducting gap of 400 μV, due to the presence of two Al layers (the bottom and the top electrodes). It can be observed that this gap remains constant while changing the applied field. Due to the exchange coupling between Al and EuS, the population of spin-up and spin-down states is uneven, thus, secondary peaks appear at $\pm 2\mu_B H$, this is the so-called Zeeman splitting, introduced at the beginning of this Chapter. It can be observed that with increasing applied field, the peaks at higher absolute value of voltage decrase, increasing the degeneracy between spin up and down states.

The exchange coupling depends on the thickness of EuS and Al: in samples with very thin Al, the superconductivity is suppressed by the strong magnetism of EuS, whereas, in samples where Al is thick compared to EuS, the spin splitting is absent at distances away from the interface. In [146], a critical value for the thickness of Al, $d_c \approx 6$ nm was found, when the thickness of EuS was ≈15 nm.

The tunneling spectroscopy curves measured in this junctions confirm that no applied field is needed to split the density of states of Al in the presence of EuS. However, it was observed that EuS needed to be magnetized to make the spin splitting appear. This fact is represented in Fig. 5.9, where the comparison of the differential conductance before (black) and after (red) the magnetization of the junction in Fig. 5.8a is shown.

Before magnetizing the EuS layer, the DoS of Al displays two wide peaks at ±0.4 mV. The broadening of these peaks with respect to the expected shape for a superconducting material comes from the interaction with the ferromagnetic insulator. But this interaction is not strong enough to completely spin-split the DoS. This indicates that there are magnetic domains with sizes larger than the superconducting coherence length ξ_0 in the EuS film as described in previous works[12]. Domain sizes much below ξ_0 would lead to a vanishing average spin splitting. When an external magnetic field is applied, the magnetic domains of EuS start to align. When this

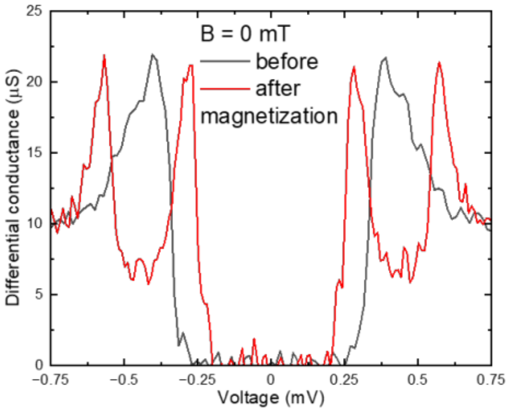

Figure 5.9: Differential conductance of Al/AlOx/Al/EuS/silica tunneling junction, in the absence of applied magnetic field, before and after the magnetization of EuS, measured at 30 mK.

field is suppressed, the spin-splitting is observed (Fig. 5.9, in red). These results confirm, therefore, the superparamagnetic behaviour of EuS.

The most relevant result on this section is that thanks to the exhaustive study on the deposition of EuS thin films of the previous Chapter, and the impact of the preparation conditions of the properties of the layers, it is possible to obtain tunnel junctions that are reproducible in terms of spin splitting of Al DoS. Once the parameters have been optimized, around 70 junctions have been produced and close to 100 % of them worked.

5.6 Spin-filtering tunnel barriers

As shown in the introduction of the Chapter, for the thermoelectric effect, in addition to the spin-splitting of the DoS of the superconductor, a spin asymmetry of the current through the barrier is needed. To obtain this non-reciprocal transport from a FI/S based tunnel junction a spin selective probe is required. This can be achieved in two different modes: (i) by using a FI as a spin selective tunnel barrier in S/FI/N [91, 147–150] or S/FI/S [86, 91, 150–152] junctions and (ii) by means of a ferromagnetic probe in F/I/S/FI [89, 147] and S/FI/F [153] configurations. For both configurations the non-reciprocity was visible in the asymmetry of the tunneling spectroscopy.

In this experiment, the selected configuration was F/I/S/FI due to the dependence of the properties of EuS on the preparation conditions, which would lead to a lack of reproducibility of the tunnel barrier. Thus, tunneling junctions substituting the top Al electrode by a Co electrode were produced, as displayed in Fig. 5.10.

Although the asymmetry of the I-V curve is observed, an increment of the zero bias conductance is accompanied by an increment of the zero bias conductance (from 0, in the case of Al/AlOx/Al/EuS to 400 μS for Co/AlOx/Al/EuS). In order to probe if it was caused by the magnetic interaction between EuS and Co, a tunnel junction without the EuS layer proximitizing the superconductor was explored and represented in Fig. 5.11. As expected, the spin splitting of the DoS of Al is not observed,

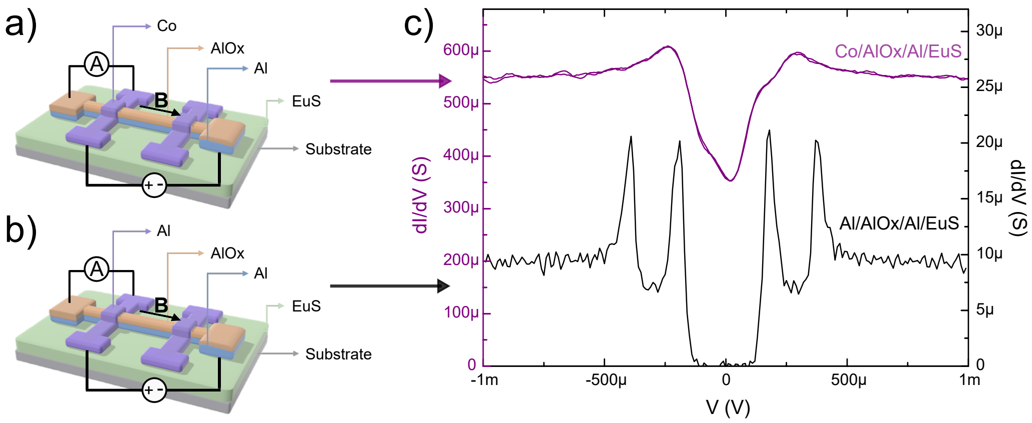

Figure 5.10: Comparison of tunneling spectroscopy measurements of a tunnel junction with two metallic (Al) electrodes (purple) and a junction with metallic (Al) bottom electrode and magnetic (Co) counterelectrode (black). Both samples were measured at low temperature (30 mK) and under a magnetic field of 4 mT (Al/AlOx/Al) and 20 mT (Co/AlOx/Al).

since the superconductor is not in contact with a ferromagnet. The conductance around V=0 has decreased from 400 μS (in the junction with EuS) to 35 μS, after the magnetization (without the EuS layer). However, it does not decrease to the expected value for a superconductor (G=0 at V=0), as it was shown in the case of Al/AlOx/Al/EuS.

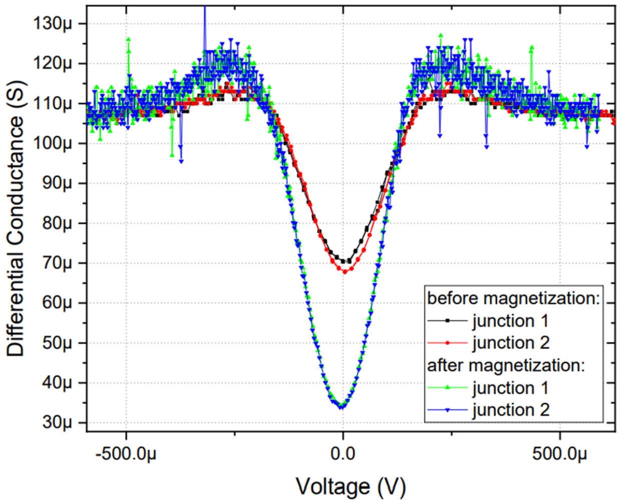

Figure 5.11: Differential conductance of Co/AlOx/Al tunnel junction, before and after applying a magnetic field, measured in the absence of field, at 30 mK.

The in gap conductance even in the absence of EuS leaded us to think whether the AlOx barrier was interdifussing in the Co stripes. This motivated a study in which a thin Al interlayer with variable thickness (0.8-2 nm) was grown between the AlOx barrier and Co, measuring the I-V response via tunneling spectroscopy, as presented in Fig. 5.12.

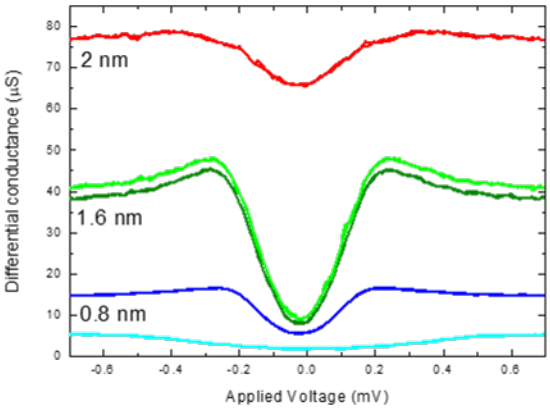

Figure 5.12: Differential conductance of tunneling junctions with stacking structure: CaF_2/Co/AlOx(X nm)/Al/EuS/SiO_2, where X=0.8 (blue), 1.6 (green) and 2 (red).

Although in principle the addition of the interlayer should decrease the in-gap states (ideally to zero), it can be observed that the thicker the interlayer, the higher the conductance at zero bias. And moreover, the sample with the thinnest interlayer (0.8 nm) exhibits a small ratio between normal and superconducting conductance (G_N/G_S). None of the samples show spin splitting nor spin filtering.

The origin of this subgap conductivity is still under debate, and further studies are needed.

5.7 The influence of the substrate temperature

Among others, one strategy to improve the performance of junctions has been to decrease the substrate temperature during the growth. It has been reported that the low temperature growth of Al/EuS bilayers allow for the application of lower magnetic fields due to a decrease of the coercive field of EuS when deposited onto a cold substrate (77 K). Via XRD it has been shown that the crystals are smaller for low temperatures [86, 154]. The growth of metals on cooled substrates has been proven to present several advantages, being a good strategy to reduce the thermal stress on the substrate and to improve the quality of the metal films by reducing the formation of defects, such as voids and grain boundaries. The main properties of the metals grown at low temperature, compared to room temperature growth, are the reduction of the grain size and of the surface roughness, both due to the reduced surface mobility of metal atoms [155, 156]. In this section, a comparison on the topology (measured via AFM) of Al and EuS for bilayers grown at room temperature and liquid nitrogen temperature (77 K) will be presented.

Prior to study the topology, the chemical composition of EuS was checked, since, as demonstrated several times along the previous chapter, the composition of this compound is sensitive to the preparation conditions. Two identical 11 nm EuS thin films were deposited on SiO_2 with a sublimation temperature $\approx$1600 ℃, varying the substrate temperature from room temperature to 77 K. The chemical composition was studied *in situ* via XPS, measured at the Eu 3*d* core level, as shown in Fig.

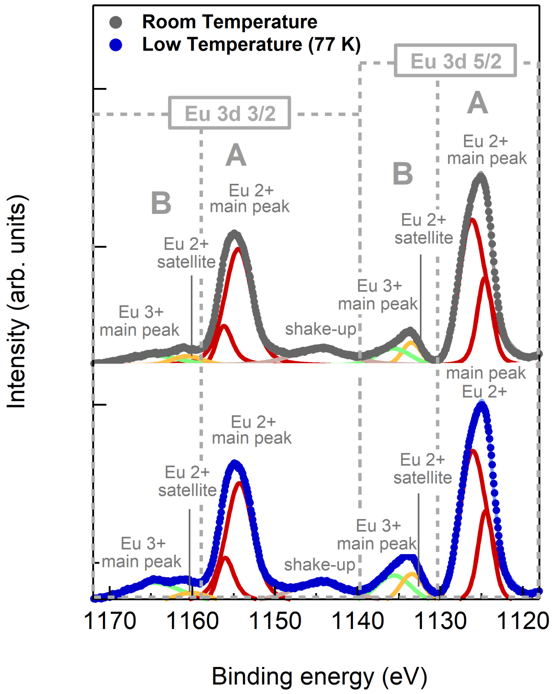

Figure 5.13: XPS spectra at Eu 3*d* core level of a 11 nm thick layer of EuS grown on SiO_2 at room temperature (top) and 77 K (bottom), with respective deconvolution of photoemission peaks.

5.13. A Shirley background was subtrated from the photoemission spectra and the peaks were deconvoluted as previously shown in chapter 4, to perform a quantitative analysis.

Table 5.2: Percentage of area of the analysis of the XPS spectra at Eu 3*d* core level, for room temperature (RT) and low temperature (LT, 77 K) of the substrate during the growth.

Eu 3d (% area)						
Prep	**3/2**		**5/2**		**Total**	
	A	B	A	B	A	B
RT	35.1	8.3	46.2	10.4	81.3	18.7
LT	33.3	9.6	45.4	11.7	78.7	21.3

As aforesaid, it is difficult to separate the contribution from Eu^{2+} and Eu^{3+}, since the peaks centered at 1134 eV and 1164 eV are formed by the satellite of Eu^{2+} and the main peak of Eu^{3+}, and the deconvolution is very fitting-dependent. So for the comparison of the chemical composition, the A and B peaks will be studied. The area percentage of each contribution is in Table 5.2.

Both spectra show the same peaks, located at the same binding energy, and the percentage areas in 5.2 do not show major differences, taking into account the error of measurement and analysis. Therefore, the chemical state of EuS remains the same when changing the substrate temperature from room temperature to 77 K. The ratio

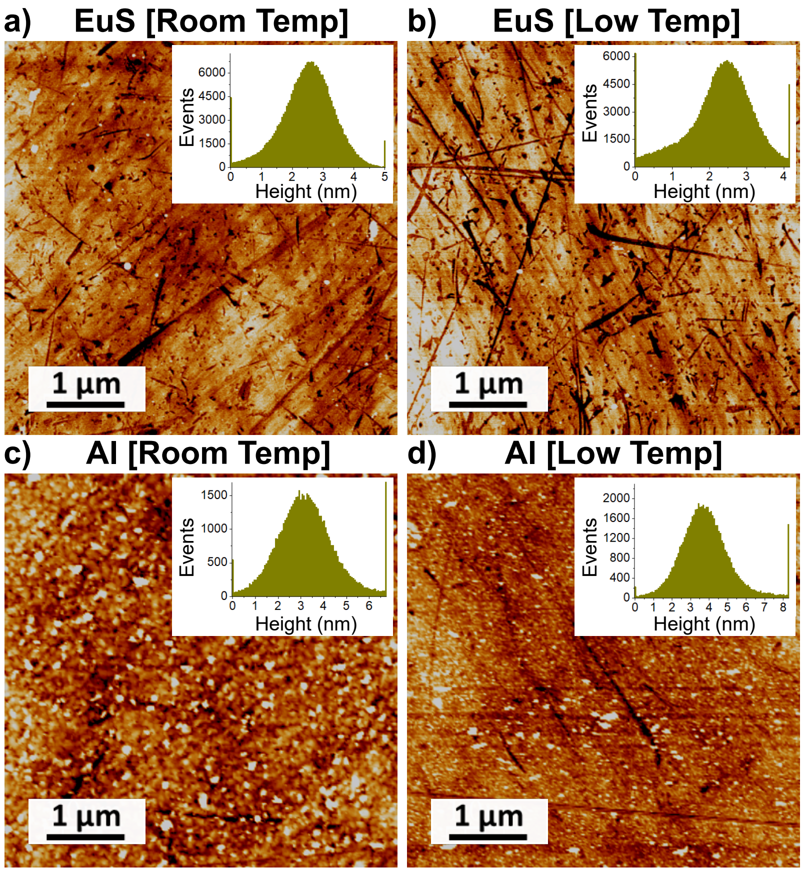

Figure 5.14: Atomic Force Microscopy images of EuS and Al grown at room temperature, (left) and at low temperature (77 K, right). The distribution of the heights is included as an inset.

Eu:S was also calculated, via Eq. 4.1, finding values around 1 for both cases. On the other hand, since aluminum is a metal, its chemical composition is not affected by the sublimation temperature, neither the substrate temperature during the growth.

Hence, the 12 nm thick Al wire (200 μm width) were grown also at room temperature and at 77 K. The topography of Al/EuS bilayers was examined via atomic force microscopy *ex situ* in order to see whether the surface roughness changes. This information is extremely useful from the standpoint of device fabrication because it reveals the shape of the interface between the grown materials and the substrate. Fig. 5.14 shows the topography of EuS (top) and Al(bottom), measured in air in tapping mode, for room temperature (left) and low temperature (right). An inset with the distribution of heights in included.

The AFM images of EuS do not show main differences when the substrate temperature is changed. Although more dark lines appear in the 77 K image, they come from the substrate, that seems to be scratched during the cleaning in ultrasound bath. However, the topography of the EuS remains the same: for both cases, the average height of the EuS layer is around 2-3 nm. In the case of Al, the topography is affected by the sustrate temperature, being more favorable the growth at 77 K, where a flatter surface is produced, decreasing the granular appearance with respect to the room temperature evaporation.

Table 5.3: Parameters extracted from atomic force microscopy (AFM) measurements, for the Al/EuS bilayers grown at variable substrate temperature (room temperature and 77 K).

Layer	Temperature	Roughness average (nm)	Average height (nm)
EuS	**RT**	1.31	4.81
	LT	1.04	3.32
Al	**RT**	0.69	3.55
	LT	1.07	3.89

The temperature of the substrate during the growth process affects the performance of the final device, improving the spin splitting of the EuS/Al heterostructure.

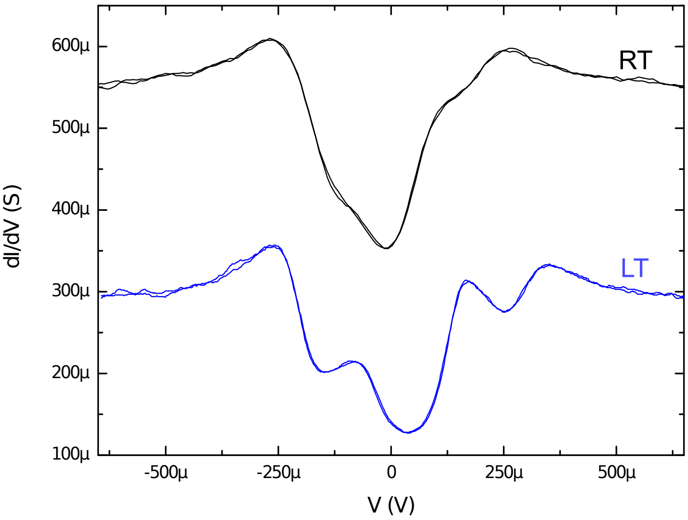

Figure 5.15: Comparison of differential conductance measured via tunneling spectroscopy in four probe configuration of tunneling junctions grown at room temperature (black) and 77 K (blue), measured with an external, parallel applied magnetic field of 20 mT. The stacking structure of the junction (top-bottom) is: CaF_2/Co/AlOx/Al/EuS/SiO_2. The temperature during the growth applies only for the Al and EuS layers. The measurements were performed at 30 mK.

Due to the better performance of the junctions when Al and EuS are grown in cold, for the production of electromagnetic sensors, all the junctions were fabricated with the substrate at 77 K during the deposition of these two materials.

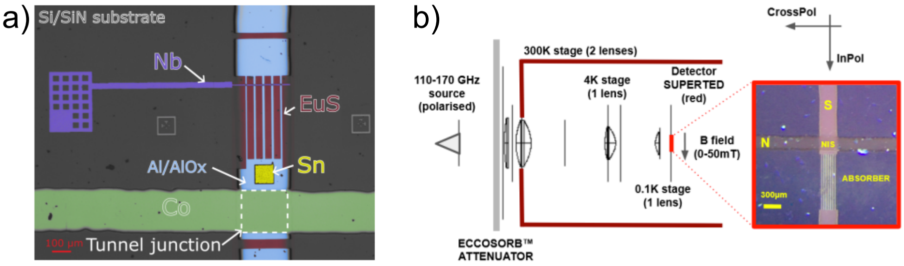

Figure 5.16: Electromagnetic radiation sensors fabricated from the tunnel junctions studied along the chapter: a) Fake-color optical micrograph of the processed junction for the X-Ray detector. b) THz detector testing setup and colored optical image of the processed junction. Figures taken from [157].

5.8 Implementation in radiation sensors

In addition to the study already presented in this Chapter, the collaborators of the project have implemented the devices in sensors, which can be observed in Fig. 5.16. On the one hand, in the group of I. J. Maasilta, Z. Geng investigated the implementation of the junctions in X-Ray detectors. For that purpose, an absorber has to be added. The absorber consists in a 350 nm thick superconducting Sn square, with an area of 100 μm × 100 μm, which contacts directly the superconducting Al electrode (with the insulating barrier AlOx removed chemically) and is placed laterally next to the junction area. On the other hand, in the group of F. Giazotto, E. Strambini and M. Spies were able to nanopattern an absorber in the Al wire via UV lithography, in order to enhance the sensitivity of the junctions to incoming THz radiation. It was proved that the junction detected photons at 150 GHz, being the first proof of thermoelectric effect in the THz range. With decisive optimisations, this detector might have the potential to compete with the existing cryogenic sensors operating at THz frequencies, such as Kinetic Inductance Detectors (KID), Transition Edge Sensors (TES), high-impedance bolometers and others. This data is the first demonstration of biasless superconductor-based radiation sensing. However, its analysis and optimization requires still further work.

Since the deposition of EuS thin films has been proven to strongly depend on the preparation conditions, the reproducibility of the data despite being possible, requires an exhaustive control. For that reason, a new class of ferromagnetic insulators was explored, in order to simplify the process.

Summary

Thanks to the control of the chemical composition of EuS by means of the power (sublimation temperature) of the e-beam evaporator, it is possible to tune its properties and obtain reproducible results in sense of exchange coupling with the superconductor Al. In the interface EuS/Al a chemical reaction Al-S seems to take place. The topology of the interface improves when the substrate is kept at low temperature, being translated into a better splitting of the DoS of Al.

The oxidation of aluminum via oxygen plasma leads to uniform AlOx barriers, with resistances in the order of kΩ. As a result of the addition of Co as the counterelectrode, the current across the junction is spin-filtered. As a result from the implementation of this junction in radiation sensors, the first proof of concept of the thermoelectric effect has been done.

Chapter 6

Beyond TED sensors: implementation of EuS in devices for spintronic application

The knowledge on the properties of EuS and the control of the magnetic response by means of the growth conditions opens up the possibility of implementing this ferromagnetic insulator in different heterostructures, which have application in spintronics. By adapting the characteristics of EuS to the requirements of each experiment, and collaborating with other research groups, EuS has demonstrated to be a useful material that serves to demonstrate quantum effects and discover new properties of other materials. In the current chapter, the applications of EuS apart from the superted sensors will be presented.

6.1 Superconducting spintronic tunnel diode

The same stacking structure explored in the superted project worked as a rectification diode. Diodes are non-linear and non-reciprocal circuits with a strongly direction-selective electron transport. The search for symmetry-breaking structures has focused on semiconducting and metallic junctions. However, the emerging cryogenic technologies require the work at sub-Kelvin temperatures. Semiconductors, due to their large energy gap, are not suitable at very low temperatures. This problem can be overcome by using low-dimensional materials, such as quantum dots [158, 159], but the impedance of these systems tend to be high, decreasing the rectified currents. Superconductors are good candidates, since they present intrinsically low impedance, and lower energy scales of the superconducting gap (∼meV) compared to semiconductors (∼eV). But, as aforementioned, the implementation of a superconducting diode requires breaking the spin-hole symmetry, being contradictory to the BCS superconducting state, which implies electron-hole symmetry. There are different approaches to break this symmetry, but this study focused on the FI/S heterostructures, as in the previous chapter, which combine the spin splitting and filtering. When these two effects are present it is possible to break the electron-hole symmetry of the system and generate direction-selective electron transport [11, 160]. Fig. 6.1 summarizes the rectification diode effect in the F/I/S/FI junctions.

Although the rectification effect has been also demonstrated in a different het-

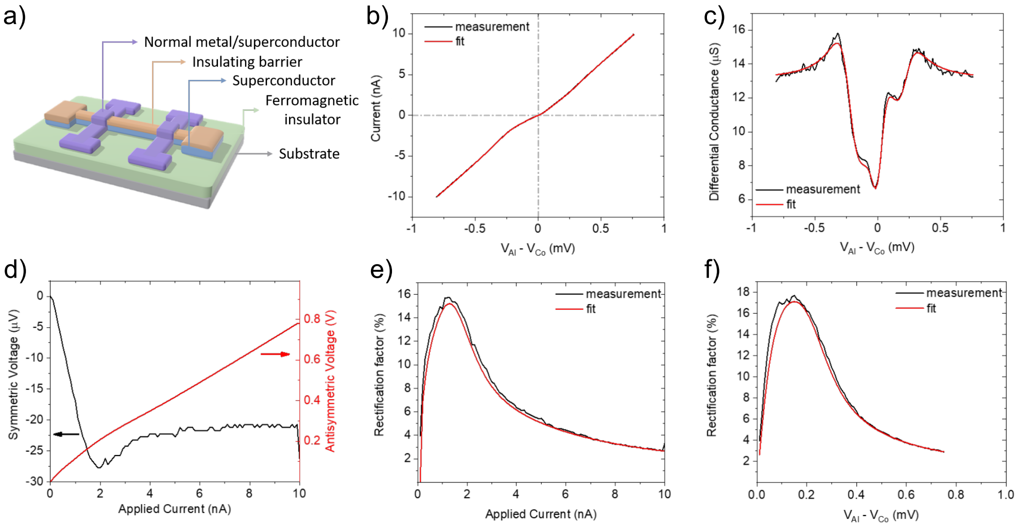

Figure 6.1: Rectification of a superconducting diode [147]. a) Schematic representation of the measured tunneling junctions with a stacking structure: CaF_2 (7 nm)/Al(12 nm)/AlOx(5 nm)/Al(12 nm)/EuS (16.5 nm)/SiO_2. b) Current-to-Voltage (I(V)) characteristic of the junction measured at T≈50 mK, B = 0 T. c) Differential conductance obtained from the numerical derivative of b. d) Symmetric and anti-symmetric parts of the I(V) characteristic in b showing a sizable symmetric component of the voltage. e) and f) Rectification coefficients evaluated from the I(V) characteristics in current and voltage bias, respectively (black line). The comparison of the rectification extracted from the full numerical model is also shown (red line). The details of the fittings are in [147].

erostructure consisting on S/FI/N, which presented higher rectification with respect to the F/I/SC/FI samples of this study, the latter has two main advantages: rectification of the current even at zero applied magnetic field (due to the presence of spin-splitting at B=0) and the possibility to invert the diode (just by changing the relative magnetization of EuS and Co, that can be parallel or antiparallel). These two characteristics convert this materials combination in an appealing diode for applications.

6.2 Magnetic interaction with Phthalocyanine Molecules

The magnetic properties of molecules, as well as their interaction with substrates, have been widely studied due to their potential application in the field of spintronics, such as data storage and processing [161]. An interesting case is the interface between magnetic molecules and inorganic magnets, which act as spin injection materials and serve as electrodes [162].

Phthalocyanine (Pc) is an aromatic, organic molecule with an atomic formula $(C_8H_4N_2)_4H_2$, which center can be occupied by a metallic atom, as represented in Fig. 6.2. The magnetic properties of metal phthalocyanines are determined by the metal ion at the center of the molecule. In general, phthalocyanines containing transition metal with unpaired electrons exhibit paramagnetic behavior, while those with paired electrons exhibit diamagnetic behavior. The presence of unpaired electrons in the transition metal ion can lead to a magnetic moment, which can interact with external magnetic fields.

The magnetic interaction between Mn-phthalocyanine (MnPc) and EuO was shown to be antiferromagnetic [163]. The loop at Mn $L_{2,3}$ edge exhibited an opposite direction of magnetization with respect to the loop measured at the Eu $M_{4,5}$. This antiferromagnetic coupling was also observed in the inversion of the XMCD signal around the Mn $L_{2,3}$ edge. These results, combined with the results of EuS as a spin injector[148, 164], motivated the study of magnetic coupling between phthalocyanine molecules and EuS.

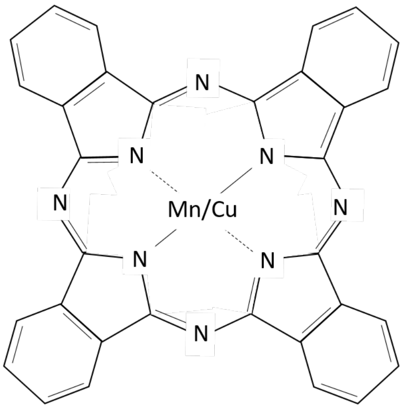

Figure 6.2: Sketch of the structure of the magnetic phthalocyanine

In this study, the central atom was chosen to be Cu or Mn. Both CuPc and MnPc are paramagnetic due to the presence of unpaired electrons in their d-orbitals. Regarding the magnetic anisotropy, CuPc has an in-plane magnetic anisotropy, meaning that its magnetic moments are preferentially oriented within the plane of the molecule. This is because CuPc has a planar structure and the magnetic orbitals are mainly located in the π-system of the molecule, which is oriented parallel to the plane of the molecule. On the other hand, MnPc has an out-of-plane magnetic anisotropy, having its magnetic moments preferentially oriented perpendicular to the plane of the molecule, because MnPc has a distorted structure with a slight wrinkling of the molecule, which results in the magnetic orbitals being oriented perpendicular to the plane of the molecule [165]. The magnetic response of these molecules in the monolayer regime, grown onto different substrates, has been studied via different techniques, as XMCD. To interpret the results from CuPc/EuS and MnPc/EuS, the XMCD results on non-magnetic substrates will serve as a reference for the magnetism of the molecules themselves. The XMCD signal of these molecules on Ag(001) was published by Stepanow and co-authors[166]. They reported a XMCD signal for 1 ML of CuPc on Ag(001) of around 46 % of the XAS signal for normal incidence and $\approx$ 10 % for grazing incidence, indicating an in-plane magnetization, while for MnPc, the ratio XMCD/XAS was 28 % for normal incidence and 37 % for grazing incidence.

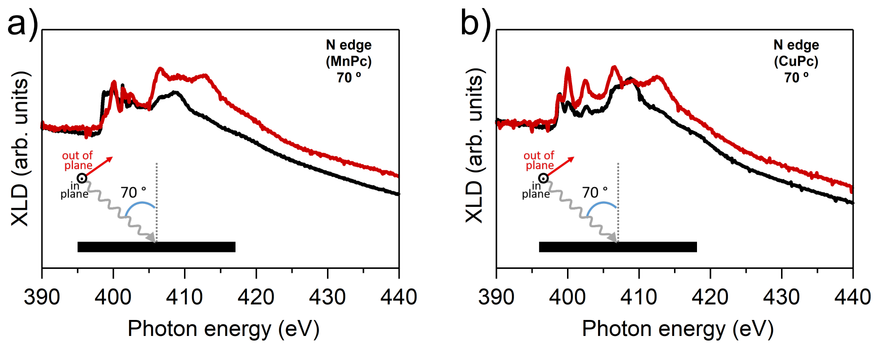

Figure 6.3: XLD of a) MnPc and b) CuPc at N $L_{2,3}$ edge, measured at 2 K in the absence of an applied magnetic field.

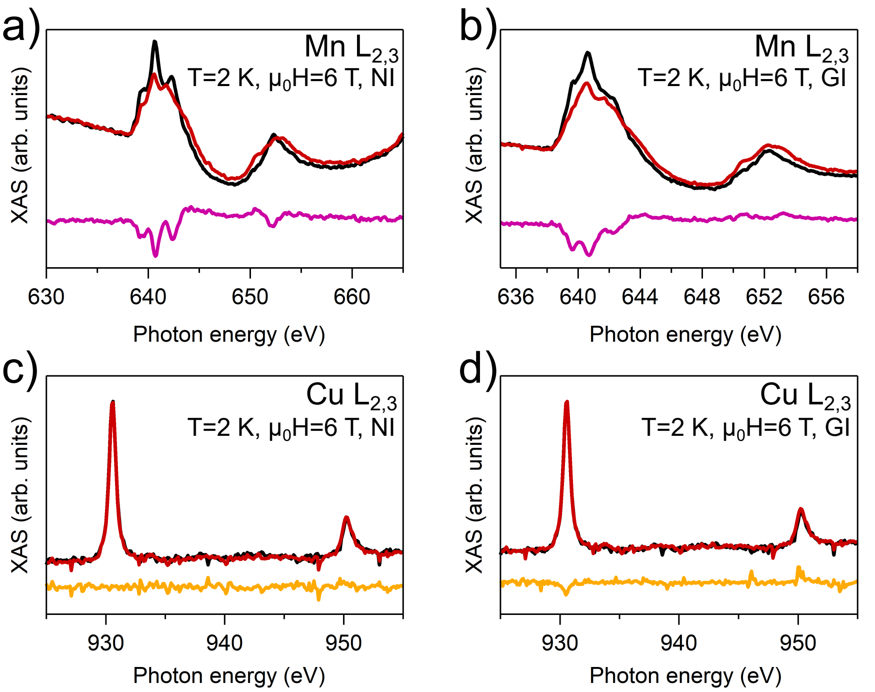

Figure 6.4: XAS and XMCD spectra for MnPc at Mn $L_{2,3}$ edge (top) and CuPc at Cu $L_{2,3}$ edge (bottom), measured at 6 T, 2 K and different geometry: normal incidence (left) and grazing incidence (right).

Experimentally, a ML (or close to a ML) of MPc (M=Mn and Cu) molecules were deposited on top of 5.5 nm of EuS grown on InAs. As it is discussed in Chapter 4, the EuS shows high degree of crystallinity when grown on InAs and therefore it is an ideal surface to do XMCD upon molecular deposition.

Prior to investigate the magnetic interaction of the molecules with the EuS, the possible orientation of the molecules on the surface was checked. To do that X-ray linear dichroism (XLD) spectra were measured at the N $L_{2,3}$ edge. At the microscopic level the dichroism comes from the anisotropy of the charge or the spin. In the absence of applied field, the spins of the MPc are not aligned and the differences in the absorption of the light due to the polarization direction depend only on the charge distribution. In XLD, if the polarization of the light is parallel to the molecular orbital there is absorption while this is not happening if light and orbital are perpendicular. In molecules such as MPc, the σ orbitals are in the plane of the molecule and the π orbitals are perpendicular to the ring. Fig. 6.3 shows the N $L_{2,3}$ edge, measured at grazing incidence, with horizontal and vertical polarization of the light, at 2 K and in the absence of applied field. In this geometry, with the sample normal forming an angle of 70deg with the incident beam, the vertical polarization corresponds to in plane polarization and the horizontal, with almost out of plane polarization. The two spectra of each sample have a different shape, however, the differences are subtle and no preferred orientation for the molecules on EuS can be determined.

In Fig. 6.4, the XAS and XMCD of 1 ML of CuPc (MnPc) on EuS/InAs, measured at the Cu (Mn) $L_{2,3}$ edge, at 2 K and applying an external magnetic field of 6 T is displayed. The red and black curves correspond to the absorption with right and left circular polarization, respectively. And the purple and orange curves are the differences between both.

For the case of the MnPc molecules (purple curve), there is XMCD signal, with same sign than reported for non-magnetic substrates [166], opposite to the reported data for MnPc/EuO, where an inversion of the XMCD spectra was observed, revealing an antiferromagnetic interaction [163]. On the contrary, the XMCD spectra of CuPc (yellow curves) do not show any peak. The quenching of the magnetic moment of CuPc would be attributed to the hybridization of the molecular and surface states. This is the mixing of the electronic states of the molecules and the surface they are in contact with, CuPc and EuS in this case. These hybridized states can have different spin orientations than the original molecular states, changing the magnetic response. The degree of hybridization depends on various factors, such as the chemistry of the molecule, the properties of the surface, and the orientation of the molecule relative to the surface.

Comparing the magnetization loops at the Eu $M_{4,5}$ edge before and after the deposition of the phthalocyanine molecules it is possible to determine whether the hybridization affects the magnetic response of EuS. In Fig. 6.5, the magnetization loops of EuS before the deposition of molecules are represented in grey, while the loops for EuS covered with molecules are plotted in purple/orange. Some differences can be observed in the magnetization loops, despite they are not drastic, the shapes slightly change. Note that the change in the magnetic response of EuS can be less noticeable since the EuS layer is thicker than the ML of molecules.

Moreover, the magnetization loops of the 1 ML MnPc/EuS sample were measured at normal and grazing incidence, at 2 K and under a sweeping magnetic field ±6 T, at the Mn $L_{2,3}$ edge and the Eu $M_{4,5}$ edge, as displayed in Fig. 6.6. Note that the curves are normalized to the saturation magnetic moment obtained from the sum-rules of the XMCD data, to ease the comparison between the loops. Since XMCD gives element-specific magnetization loops, it is an useful technique to identify the origin of the magnetic response in heterostructures. In this case, while the EuS (grey curve) behave as a ferromagnetic material, as expected, the MnPc (purple dots) does not exhibit magnetic response (linear dependence with the field and small signal almost comparable with the noise). These results do not coincide with the experiment performed in the MnPc/EuO system [163], where an antiferromagnetic coupling

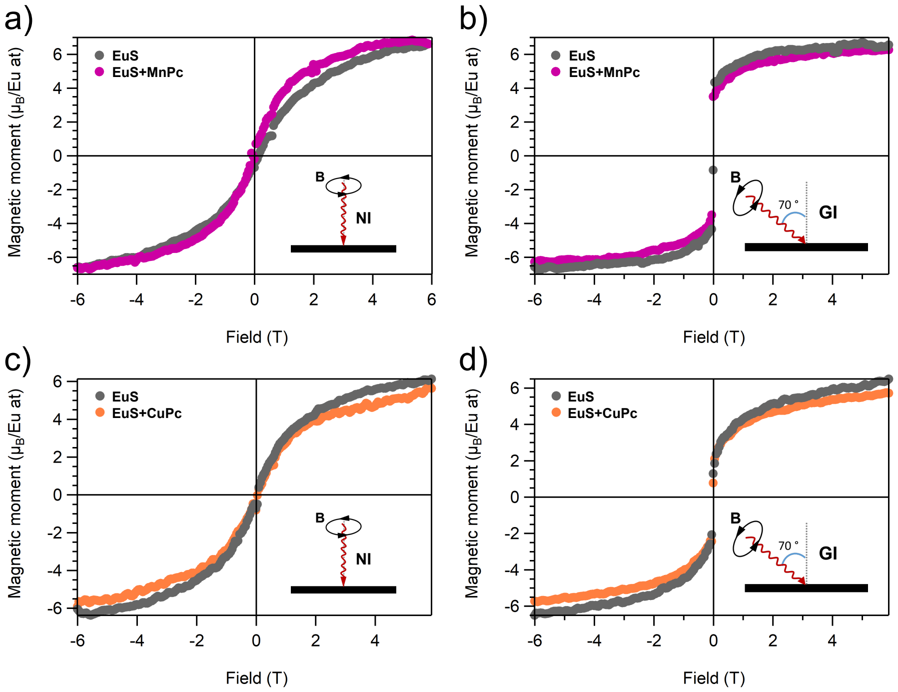

Figure 6.5: Magnetization loops at the Eu $M_{4,5}$ edge measured at 2 K before (grey) and after of the deposition of MnPc (up, purple) and CuPc (bottom, orange) at normal incidence (left) and grazing incidence (right).

was observed. There are multiple reasons that could explain this difference in the behaviour of both systems. One of them is that the different chemical environment in EuO and EuS changes the energy levels, impeding the coupling between these ferromagnetic insulators and the MnPc. Another reason is the orientation of the molecules on the FI substrate, which has been reported to be flatter in the case of EuO. Since the magnetism in EuS and EuO is due to the indirect exchange, it extremely depends on the bonds and angles between them, thus, a change in the geometry could modify the magnetism. Anyway, further studies on this MnPc/EuS system is required, to find an explanation of the magnetic response, accompanied by theoretical calculations.

For the case of CuPc, since this sample did not show XMCD signal at the Cu $L_{2,3}$, it made no sense to measure the magnetization loops.

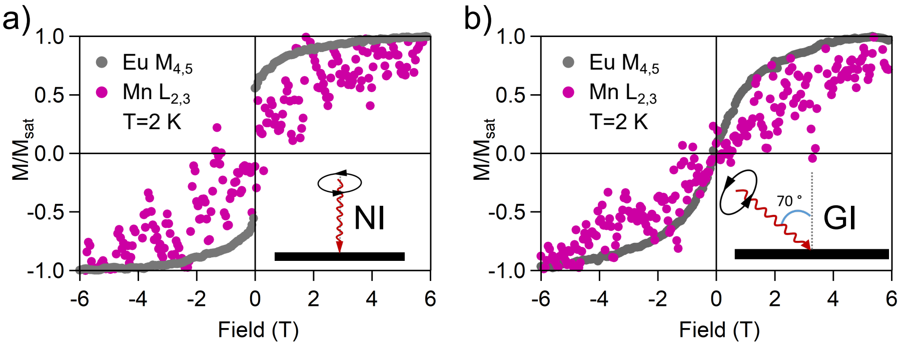

Figure 6.6: Magnetization loops of 1 ML of MnPc on EuS, measured at Eu $M_{4,5}$ edge (grey), and Mn $L_{2,3}$ edge (purple), under an applied magnetic field ranging ± 6 T, at 2 K, at NI (a) and GI (b).

6.3 Ferromagnetic resonance of EuS

Recent theoretical and experimental studies suggest that the spin transport in thin film superconductors can be probed via spin pumping, which is a technique that allows for the transfer of the spin angular momentum from a ferromagnetic thin film adjacent to a superconducting thin film via ferromagnetic resonance (FMR) [167, 168]. The efficiency of spin pumping is linked to a parameter of the ferromagnet called the Gilbert damping (α) in the phenomenological Landau-Lifshitz-Gilbert. Experimentally, it can be extracted from the frequency dependence of the FMR linewidths [167, 169]. The Gilbert damping describes how much the system is damped under FMR. The superconducting transition will excite the quasiparticle density of states, which acts as an additional spin carrier to the system [167].

This work has been performed in two different systems, both based in EuS thin films, in collaboration with two research groups. On the one hand, the ferromagnetic resonance was measured on Nb/EuS bilayers grown on InAs, as part of the Master Thesis of Hisakazu Matsuki[170], under the supervision of Dr Chiara Ciccarelli from the group of Microelectronics at the University of Cambridge. These heterostructures consist on 20 nm of EuS grown on InAs and covered by a Nb film of (i) 5 nm or (ii) 30 nm thick. The spin transport of the superconducting Nb was measured in this systems, as a function of the frequency, at 8.6 K (above the critical temperature of Nb), as represented in Fig. 6.7. In these plots, the Gilbert damping parameter, α is extracted from the linear fitting of the FMR linewith, i.e. the field where the maximum is located at vs the applied frequency. The values for α are 5.4 10^{-2} and 4.5 10^{-2}, for 5 nm and 30 nm of Nb, respectively.

On the other hand, in collaboration with the group of Dr Fèlix Casanova and Dr Luis Hueso in nanoGUNE, a similar experiment was carried out. FMR measurements were performed on EuS thin films grown on pyrex, which is an amorphous substrate, and a value of α=4 10^{-2} was found [171]. This result indicates that the crystallinity of the EuS does not play an important role on the Gilbert damping.

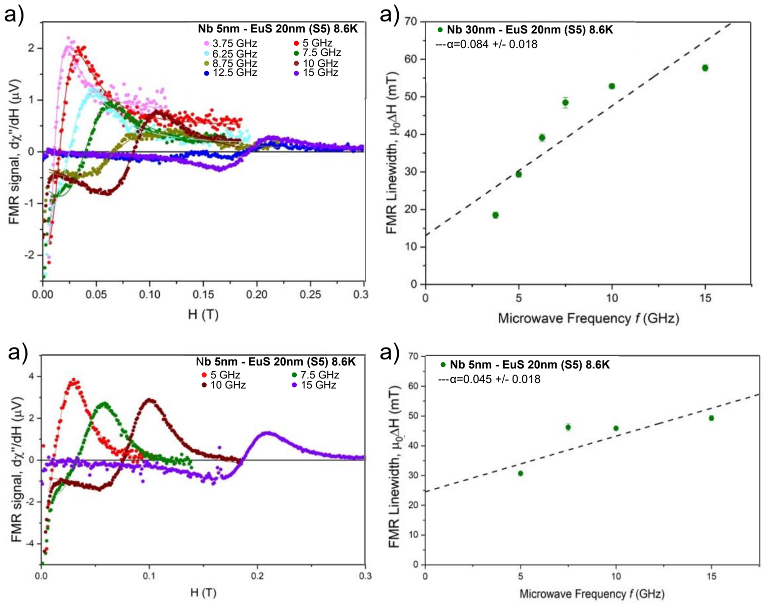

Figure 6.7: FMR measurements of the Nb/EuS bilayers on InAs at 8.6 K [170].

6.4 Magnon currents in Pt/EuS bilayers

Magnons are collective bosonic excitations in systems with magnetic order that allow the transport of spin angular momentum, even in insulators. The transport of spin information by exploiting magnon currents is a promising approach for developing spin-based information devices. In this context, magnetic insulators are an ideal platform for propagating spin information. The transport of the magnons has been mainly reported through $Y_3Fe_5O_{12}$ (YIG) and a few other ferri-and antiferromagnetic insulators [172]. However, not previous works studied magnon propagation on pure ferromagnets.

As part of the PhD thesis of Monsterrat Xochitl Aguilar-Pujol, under the supervision of Dr. Fèlix Casanova, in nanoGUNE, we studied the magnon currents in Pt/EuS bilayers grown on pyrex. The Pt layer was patterned to use them as electrodes (injectors and detectors), with variable distance between them. The measurements were performed at a temperature in the range of 2-30 K (below and above the Curie temperature of EuS) and under a magnetic field up to 9 T. Several tests were performed, depositing EuS with variable sublimation temperature and finding that the biggest magnon diffusion length was obtained for those samples grown at the highest sublimation temperatures.

By performing both local and non-local transport measurements in 18-nm-thick films of EuS using Pt electrodes, we detected magnon currents arising from thermal generation by the spin Seebeck effect. By comparing the dependence of the local and non-local signals with the temperature and magnetic field, we confirmed the magnon transport origin of the non-local signal. Finally, we extract the magnon diffusion length in the EuS film of ≈140 nm. Although this value is lower compared with Pt/YIG bilayers (probably due to the lower Curie temperature and Gilbert damping in EuS), this results are the first demonstration of incoherent magnon transport in a pure ferromagnetic insulator.

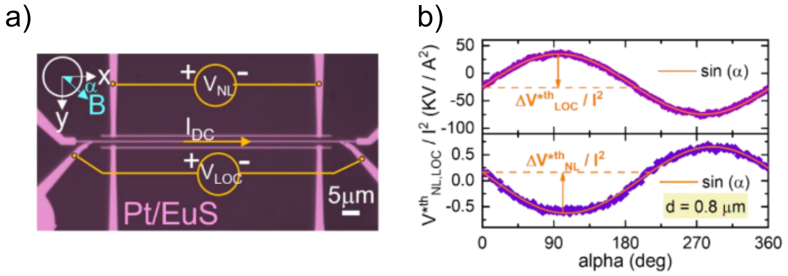

Figure 6.8: a) Optical microscope image of a device showing the measurement configuration. b) Representative LOC and NL angular dependent signal detected for thermally excited magnons at 2 K and 0.3 T.

6.5 Spin Hall Effect in Pt/EuS bilayers

One of the key challenges in spintronics is to efficiently transfer spin-polarized electrons between a ferromagnetic material (FM) and a non-magnetic material (NM) in a device. For that purpose, a strong exchange interaction at the interface is required, which can be characterized by the spin-mixing conductance (G). This G factor determines the efficiency of spin transfer and is influenced by the spin Hall effect (SHE) and the anomalous Hall effect (AHE). Recent studies have shown that the G factor can be quantified via the spin Hall magnetoresistance (SMR), in a variety of materials. In particular, the interface between a FM and a topological insulator (TI) has been shown to exhibit a large G factor, making it a promising candidate for spintronic devices. However, the use of TIs is limited by their small Curie temperature, which hinders their practical implementation in spintronic devices.

In this context, the use of ferromagnetic insulators with large Curie temperature has been proposed as an alternative to TIs. As aforesaid, the Curie temperature of EuS thin films is around 17 K, which together with the high magnetic moment, makes it an ideal candidate for spintronic devices. However, little was known about the interface between EuS and a NM. Thus, our aim was to investigate the SMR in a Pt/EuS heterostructure.

Bilayers consisting also on Pt/EuS, as in previous section, with a different patterning were employed to measure the spin Hall magnetoresistance (SMR) [173], in collaboration with Dr Juan Manuel Gómez Pérez, from the group of Dr. Fèlix Casanova. The experimental results were fitted by a microscopic model. We found that the G factor at the interface is dominated by the spin-mixing conductance (G_i) rather than the spin-mixing resistance (G_r), as is typically observed in heterostructures consisting in ferromagnets and topological insulators. The study also quantified the exchange interaction between the conduction electrons of Pt and the localized moments of Eu and determined the values of G_s, G_r, and G_i as a function of the temperature. These findings provide valuable insights into the interfacial exchange field in ferromagnet insulators, which has important implications for the development of spintronic devices.

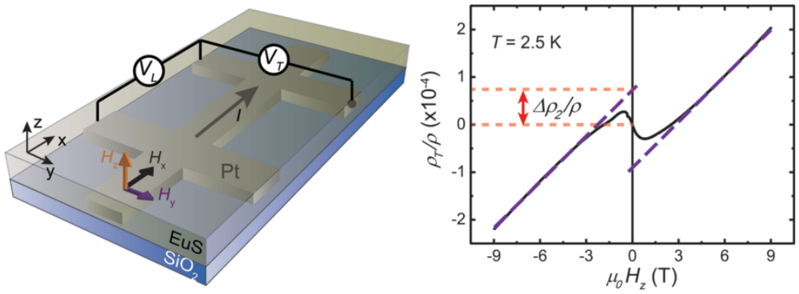

Figure 6.9: a) Sketch of the Pt/EuS device and configuration for the measurements. b) Transverse resistivity measurement in Hall configuration. Dash purple lines correspond to the linear fit performed at large magnetic fields and extrapolated to zero. The red arrow shows the amplitude corresponding to $\Delta\rho_2/\rho$.

These results are the first measurements of SMR of Pt on a purely ferromagnetic insulator. Again, the EuS layers that produced the best results were deposited at a high sublimation temperature, finding no interfacial exchange field between Pt and EuS in layers grown at lower sublimation temperatures. Furthermore, this work provides an easy method to quantify this interfacial spin-splitting field, which plays a key role in emerging fields such as superconducting spintronics.

In summary, this study highlights the potential of EuS as a promising material for spintronic applications and paves the way for further research in this area.

Summary

The detailed study of the properties of EuS thin films and the imapct that the preparation conditions have on them motivated the implementation of this ferromagnetic insulator in different systems. Thanks to the control of the magnetic response, it is possible to obtain EuS thin films with ”on demand” behaviour, adapted to the requirements of each experiment. This expertise opened up the door to several collaborations, which have been presented in this chapter. Each of them combines EuS with other materials (magnetic molecules, other superconductors and metals), being a motivation to study the interface of this FI with other materials, beyond superconducting Al. Moreover, it has been demonstrated that devices can be fabricated via a combination of techniques, such as lithography or deposition in ultra high vacuum, being totally compatible.

Chapter 7

Epitaxial bidimensional transition metal dihalides

Although EuS has been proven as a material that can be implemented in devices, where its magnetic properties can be tuned via the preparation conditions, this dependence of the properties on the conditions of the experiment make this ferromagnetic insulator a material difficult to work with. Thus, a new class of bidimensional materials which in the bulk form exhibit magnetic properties was explored.

In this chapter, a detailed study on thin films of layered, bidimensional van der Waals magnetic materials is presented. The epitaxial growth of $NiBr_2$ is confirmed onto two substrates: Au(111) and $NbSe_2$. The chemical and magnetic properties down to the monolayer regime are studied. In addition, another material of this class ($FeBr_2$) is introduced as a comparison.

7.1 Epitaxial growth of $NiBr_2$

Thin films of NiBr2 were grown by sublimating a stoichiometric powder from a Knudsen Cell at a temperature of approximately 400 ℃. A Knudsen cell is an effusion evaporator, commonly used in Molecular Beam Epitaxy (MBE) due to the easy control of the temperature. The thickness of the layers was monitored by a quartz microbalance before and after every deposition.

7.1.1 Deposition on a metal, Au(111)

The first chosen substrate to grow the 2D-TMDH was gold. First of all, to avoid effects derived from the interaction between the ferromagnetic insulators and superconducting substrate and attribute the results from magnetic characterization only to the magnetic response of the material. Second, because gold is a well-known metal, extensively studied and employed as a substrate, with an easy cleaning routine that allows for the subsequent experiments. Moreover, gold is usually employed as a contact in devices.

The growth of $NiBr_2$ was followed *in-situ* via a combination of UHV techniques such as LEED, XPS and LT-STM. The dependance of the structure and chemical composition with thickness was extracted, by measuring various thicknesses of $NiBr_2$ on Au (111), ranging from submonolayered (0.5 ML) to multilayered (2.5 ML) films.

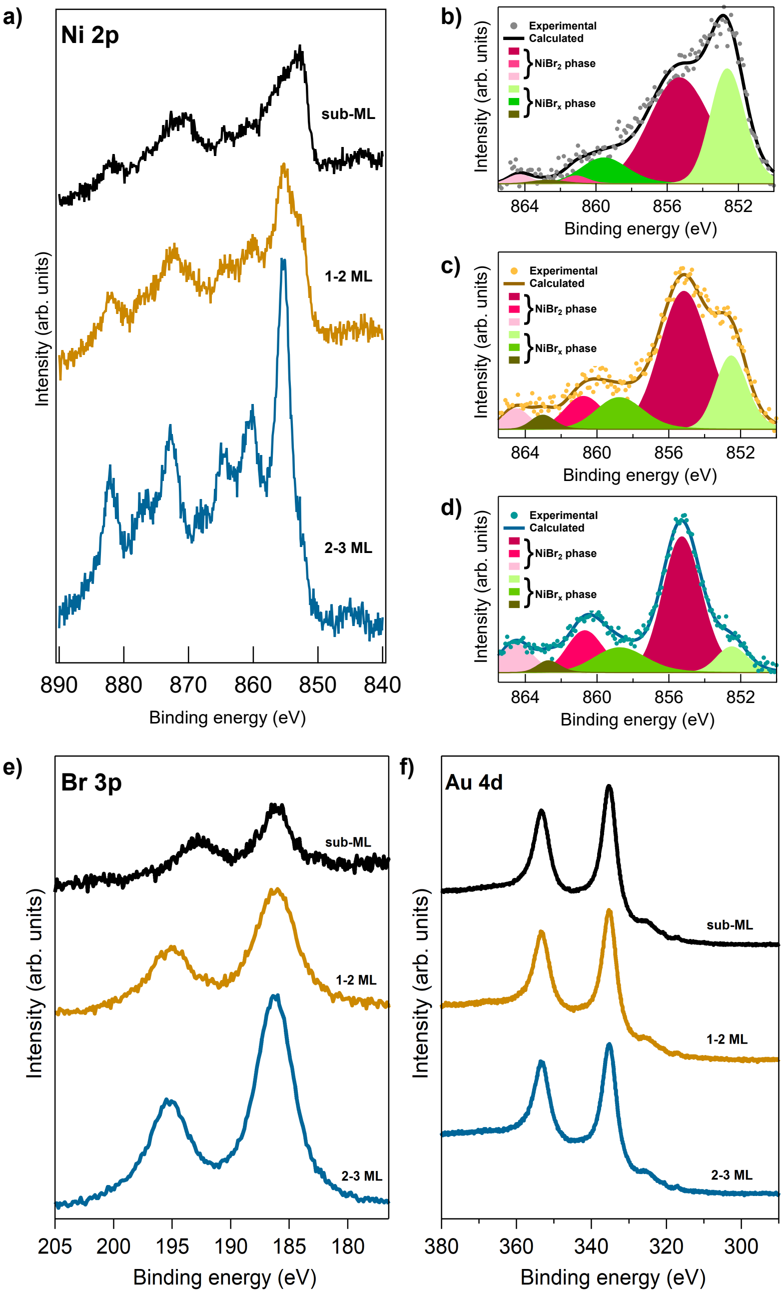

Figure 7.1: XPS spectra for different coverages of $NiBr_2$ on Au (111) at (a-d) Ni 2p, e) Br 3p $_{3/2}$ and f) Au 4d core levels. All the spectra were normalized to Au 4d.

The chemical composition was explored by XPS, as represented in Fig. 7.1, where a comparison of the spectra at Ni 2p core level for three different coverages can be observed. The energy shift of the spectra was corrected to the energy of Au 4d, and the spectra were normalized to the area of Au 4d. All of the spectra show the spin-orbit components, Ni 2p $_{1/2}$ and Ni $2p_{3/2}$, separated by an energy of $\Delta \approx 17.3$ eV. Moreover, the complex structure consisting in eight peaks coming from the different core-hole final states and plasmon resonances is observed[174]. The comparison of the XPS spectra in Fig. 7.1a highlights the changes in the shape and position of the peaks while the amount of material increases.

The detailed analysis of the spectra at the energy of Ni 2p $_{3/2}$ was performed first by sustracting a Shirley background from the spectra and then, deconvoluting the peaks according to [174], resulting in three peaks located at 864.6, 860.7 and 855 eV, as shown in Fig. 7.1 b-d, in pink. However, a second phase appears, shifted 2.5 eV towards lower binding energies. In this phase (represented in green in Fig. 7.1 b-d) Ni exhibits lower oxidation state. This more metallic-like Ni phase, that will be called $\mathrm{NiBr_x}$ hereafter, consists in a debrominated phase. As the coverage increases, less debrominated phase is obtained, corroborating that the $\mathrm{NiBr_x}$ phase exists only in the interface, meanwhile a stoichiometric $\mathrm{NiBr_2}$ is grown from the second layer. According to thermochemical investigations, sublimation of $\mathrm{NiBr_2}$ produces a gas of monomers and dimers of stoichiometric $\mathrm{NiBr_2}$, while a thermal decomposition of the precursor is negligible[175]. However, the Au (111) acts as a catalyst in the dehalogenation reaction, leading to the decrease of the energy barriers for dissociation of halogen atoms[176]. Therefore, the presence of residual Br atoms is most probably a result of the dissociative adsorption of some part of the $\mathrm{NiBr_2}$ molecules[177].

To study the structural differences in the $\mathrm{NiBr_2}$ and $\mathrm{NiBr_x}$ phases, LT-STM and LEED experiments were carried out. In Fig. 7.2, low-temperature STM images for different $\mathrm{NiBr_2}$ coverages on Au (111) are shown, as an overview (Fig. 7.2 a-c) and more in detail (Fig. 7.2 d-g). In the sub-monolayer regime, with a nominal coverage of ≈0.1 ML (Fig. 7.2 a), bidimensional islands exhibiting high order, coexist together with atomic chains on the Au (111) surface. Comparing this result with the XPS spectrum in 7.1 b, we attribute these to residual Br atoms forming a mesh on the gold surface[178]. Moreover, the Au(111) reconstruction seems to be slightly modified, suggesting a chemical interaction of the $\mathrm{NiBr_x}$ with the substrate.

This result is confirmed also by the LEED patterns. Fig. 7.3 contains patterns of Au (111) and $\mathrm{NiBr_2}$ thin films grown onto it. As expected from a clean Au (111) surface, an hexagonal pattern is obtained (marked in Fig. 7.3 a), which nominal unit cell is 2.87 Å. The LEED pattern of $\mathrm{NiBr_2}$ consists in 4 x 4 superstructure, with an unit cell 4/3 times larger than Au (111). The nominal value reported for $\mathrm{NiBr_2}$ bulk is 3.68 Å, which is close to 4/3 of 2.87 Å. Therefore, we claim that $\mathrm{NiBr_2}$ is composed of a Ni plane that is Au-commensurate with Br atoms chemically bounded onto it.

The internal layer structure of the $\mathrm{NiBr_x}$ island, depicted in Fig. 7.2 d, presents a complex chiral structure, with atomic periodicity of $\approx 3.6\ \AA$, and an additional superstructure of $\approx 11.9\ \AA$, calculated from the fast Fourier transformation (FFT), in Fig. **??** b. The Fourier Transformation consists in four sets of hexagonal patterns: the inner hexagons (green, yellow and blue circles), and the outmost hexagon (red). The inner hexagons are slightly rotated with respect to the red hexagon, suggesting a chiral structure of $\mathrm{NiBr_x}$. The periodicity of the red hexagon is $\approx 3.6\ \AA$

It is worth to say that with exception of the rotation of the two inner hexagons in the FFT, the LEED pattern for $\mathrm{NiBr_x}$ in Fig. 7.3 b resembles very much. Since the LEED image was acquired at room temperature and the STM at 7 K, the chirality in the STM image may be a consequence of a phase transition of the $\mathrm{NiBr_x}$ phase,

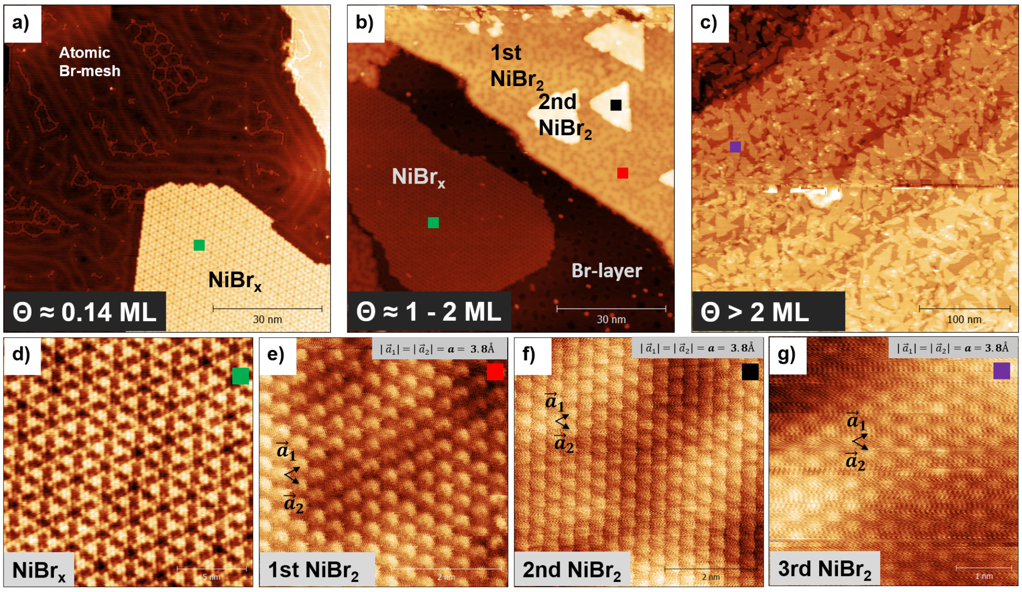

Figure 7.2: LT-STM images of different coverages of NiBr2 on Au(111) and the corresponding layer structure. a) Submonolayer regime: islands of $NiBr_x$ (labeled with a green rectangle) and Br atoms distributed on the surface. I=60 pA, U=1 V. b) Coexistence of three different types of first layer (green, yellow and red rectangles) and islands from the second layer (blakc rectangle). I=100 pA, U=1V. c) $NiBr_2$ multilayer. I=30 pA, U=1 V. d) Atomic layer structure of $NiBr_x$ (green rectangle), second (black rectangle), and third (violet rectangle) pristine layer of $NiBr_2$, showing the same lattice parameters: e) I=4.7 nA, U=0.01 V, scale bar:2 nm; f) I=1.8 nA, U=0.05 V, scale bar:2 nm; g) I=100 pA, U=-1.6 V, scale bar:1 nm.

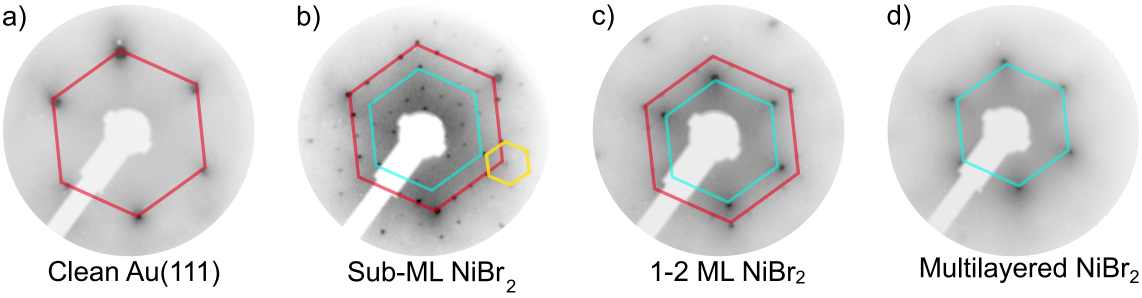

Clean Au(111)　Sub-ML NiBr$_2$　1-2 ML NiBr$_2$　Multilayered NiBr$_2$

Figure 7.3: Evolution of the LEED patterns with the coverage of $NiBr_2$ on Au (111). All images were taken at 137 eV: a) clean Au (111), b) submonolayered $NiBr_2$, c) 1.5 ML of $NiBr_2$ and d) multilayered $NiBr_2$.

taking place at low temperatures.

The stoichiometic $NiBr_2$ layers on the Au(111) surface, beyond the monolayer regime, leads to the appearance of additional hexagonal regions (red square in Fig. 7.2 b) with a lattice constant of 3.8 $\mathring{A}$ (Fig. 7.2 e). We attribute this layer to intact $NiBr_2$ domains, since their structure and lattice periodicity coincide with that of the nominal value for a free two-dimensional $NiBr_2$ layer (with lattice constant 3.7 $\mathring{A}$, according to DFT simulations[**lu2019**, 179]). Note that the first $NiBr_2$ layer appears with some contrast formed by brighter and darker patches, probably caused by interaction with the underlying substrate. The STM images for this coverage also show some nucleation of the second layer onto the first $NiBr_2$ layer, with the same periodicity as the $NiBr_2$ bulk (black rectangle, see Fig. 7.2 b,f. The second layer does not show any prominent bright-dark superstructure. Fig. 7.3 c represents a LEED pattern for the 1.5 ML case. It is similar to the pattern in Fig. 7.3 b. However, the spots forming the blue hexagon are more prominent, suggesting the coexistance of both phases, $NiBr_x$ and $NiBr_2$, with higher proportion of the latter. STM images of thicker $NiBr_2$ films, with an estimated coverage above 2 ML, show the nucleation of the third $NiBr_2$ layer on top of a complete second one (Fig. 7.2 c), also with the bulk lattice structure (Fig 7.2 g), confirming a layer-by-layer growth mode. The LEED pattern of the multilayer film displays only the diffuse hexagonal pattern and has no traces of the bare Au(111) pattern. The dimension of the hexagonal cell in Fig. 7.3 d, fits well with the unit cell of the bulk NiBr2 (3.8 $\mathring{A}$). The absence of additional spots characteristic of the 4 × 4 superstructure emphasizes the growth of exclusively stoichiometric $NiBr_2$ layers for higher coverages.

The layer by layer growth was also confirmed in the mesoscopic scale via LEEM and XPEEM in CIRCE beamline, at ALBA synchrotron. A sample with more than one monolayer was grown at room temperature, following the same procedure as done in our the laboratory. However, in the micrometer scale, nearly no contrast is observed, as represented in Fig. 7.4 confirming, thus, that the size of the islands is smaller than 1 μm.

In order to obtain bigger islands, we tried to anneal the sample up to 100 , taking images every second, but the $NiBr_2$ desorbed from the Au (111), obtaining a clean gold surface. Therefore, a sample with ≈1.5 ML was grown at 100 . In Fig. 7.5 b, a μ-LEED pattern is presented. This pattern is similar to the pattern acquired in our chamber for the same coverage (in Fig. 7.3 c), despite the fact that the μ-LEED (Fig. 7.5 b) is distorted, since the experiment was performed with the microscope working at 10 kV, energy for which the lenses were not completely aligned in the diffraction mode. The image formed at the (00) spot of the μ-LEED, i.e the bright field image, in Fig. 7.5 a, despicts bright islands on the order of the micrometer on a dark substrate, while the image formed at the (01) spot of the $NiBr_x$ reconstruction (dark field image in Fig. 7.5 c) presents the opposite constrast. For a deeper study, x-peem experiment was carried out, taking an image at the Ni L_3 edge of the XAS spectrum. The brighter areas in this image correspond to the Ni-richer areas in the sample, confirming thus that the 4x4 reconstruction from the $NiBr_x$ is only present in the first layer (where there is less Ni), and that the second layer consists in islands of $NiBr_2$.

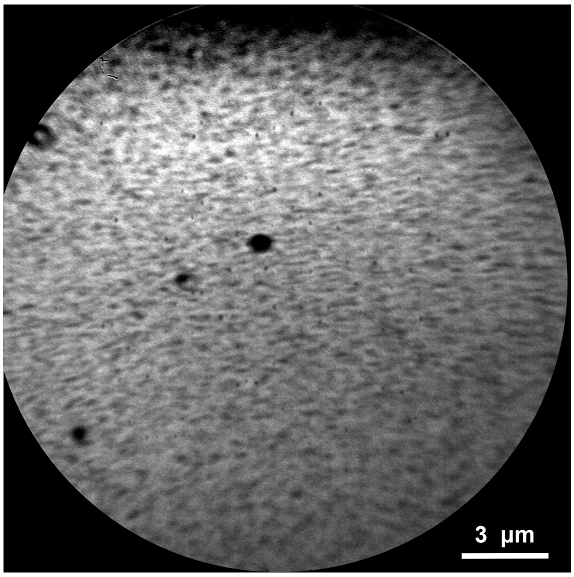

Figure 7.4: LEEM image of > 1 ML of $NiBr_2$ grown on Au (111) at room temperature.

7.1.2 Deposition on superconducting $NbSe_2$

Once the growth was explored on Au (111), the next chosen substrate was superconducting $NbSe_2$. This layered material was cleaved in UHV before the deposition of the 2D-TMDH. A similar procedure was followed to study the growth of $NiBr_2$ on $NbSe_2$. The chemical composition was examined via XPS, in the Swiss Light Source, at the PEARL beamline. The spectra are represented in Fig. 7.6. Due to the high resolution obtained in the synchrotron, it was possible to deconvolute the peaks into the reported X contributions. Since the composition remained stable with the coverage, only the deconvolution of 1.5 ML is represented. For futher information, the area percentage of each contribution for the three thicknesses is collected in Table 7.1.

Table 7.1: Area percentage of the peaks

Cov/peak (eV)	**868.2**	**867**	**864.6**	**863**	**860.6**	**859.7**	**855.4**	**854.7**	**852.5**
0.5 ML	0.8	2.7	11.7	8.2	8.2	12	26.6	28.8	1
1 ML	0.6	2.5	12.1	10.1	8.4	14.6	22.4	27.2	2.1
1.5 ML	1.2	2.5	10.7	7.3	8.6	17.9	23	27.5	1.3

LT-STM measurements were carried out, as well as LEED, to study the structure of the van der Waals thin films. The low temperature STM images of a submonolayer of $NiBr_2$ on $NbSe_2$ are presented in Fig. 7.7. The deposition at room-temperature leads to stoichiometric $NiBr_2$ islands distributed along the surface (Fig. 7.7a). The atomic resolution image in Fig. 7.7 b reveals a periodicity of ≈ 3.7 Å, as expected from the theoretical results, as well as from experiments of Refs. [64, 65] and coincides with the lattice constant observed for $NiBr_2$ on Au(111). In Fig. 7.7 b, in the bottom left corner, the structure of the $NbSe_2$ surface can be observed, showing the reported 3x3 charge density wave (CDW) superlattice [180, 181]. Note that there

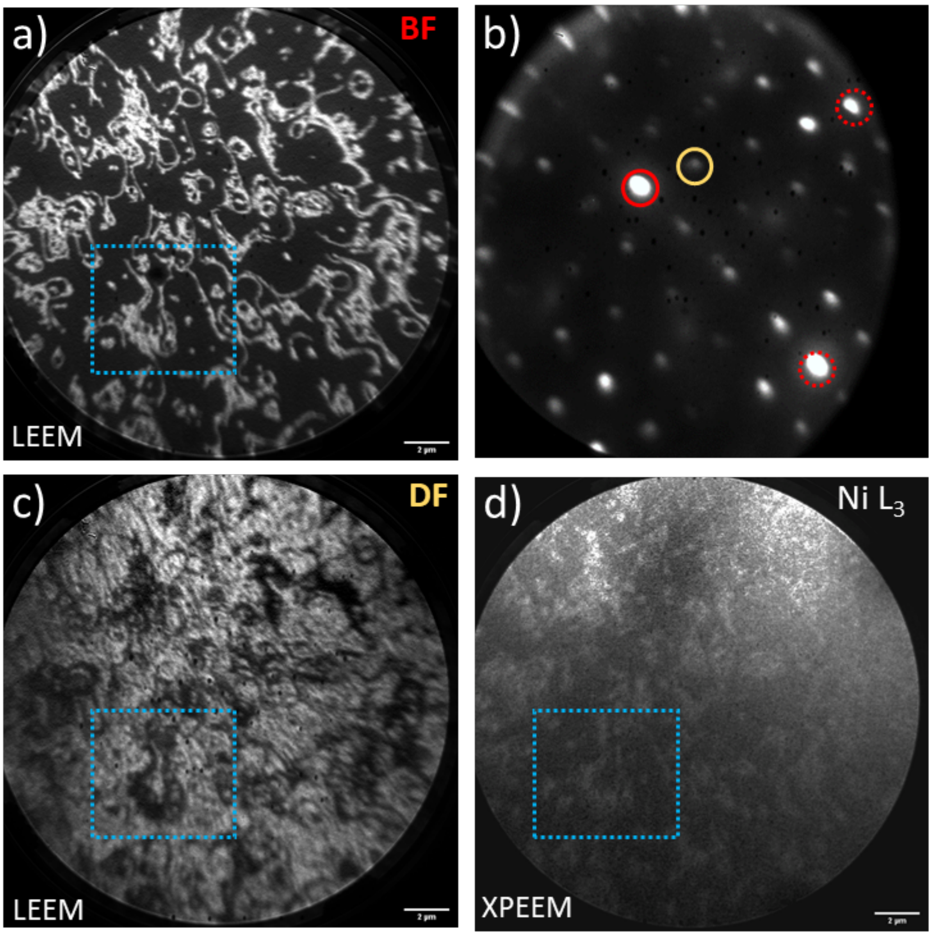

Figure 7.5: (a) Bright-field LEEM image of ≈1.5 ML $NiBr_2$ grown on Au(111) at 400 K. (b) Corresponding LEED pattern, where the red circle highlights the (00) spot used for the bright-field (BF) images and the yellow circle indicates the spot characteristic of the 4 × 4 superstructure employed for the dark-field (DF) imaging. Dashed red circles show (10) and (01) spots that belong to the pattern of the Au(111) hexagonal crystal structure. (c) Dark-field LEEM image. (d) XPEEM image showing the contrast in the absorption of the X-rays with the energy of the beam tuned to the peak of the L_3 edge of Ni. As indicated by a dotted blue rectangle, all images were taken in the same area. LEEM images were acquired at STV=8 V.

are bright features at the edges of the islands (observable at Fig. 7.8 b). These attached materials seem to be fractions of $NiBr_2$ adsorbed on the surface and stuck to the islands. However, the shape of the islands is not as sharp and well defined as reported for similar materials grown on $NbSe_2$, as in the case of $CdBr_3$ [182]. For that reason, the growth was repeated, increasing the temperature of the substrate during the deposition, to around 200 ℃. The images of the islands of $NiBr_2$ for sub-monolayer and >1 ML are displayed in Fig. 7.8.

The size of the $NiBr_2$ islands deposited with the substrate at 100 ℃(Fig. 7.8 (a, d)) is bigger, with sharper edges. However, there is some additional material adsorbed to the surface, next to the islands (Fig. 7.8a) that could be attributed

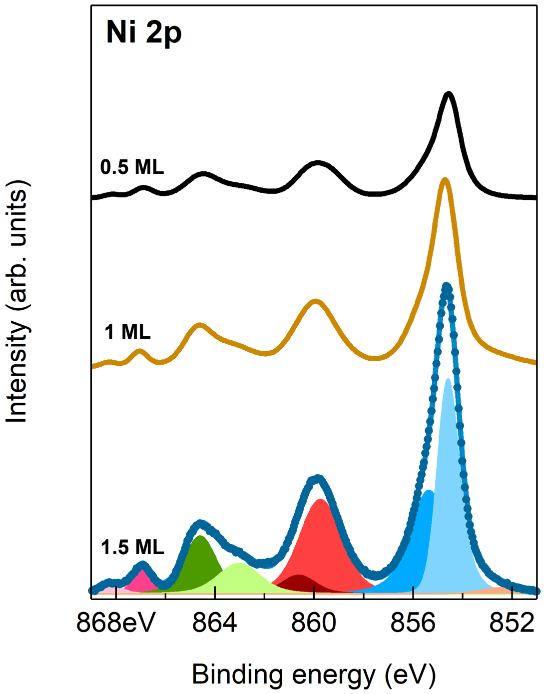

Figure 7.6: XPS spectra at the Ni 2p core level for three different coverages (0.5 ML, 1 ML and 1.5 ML) of $NiBr_2$ on $NbSe_2$

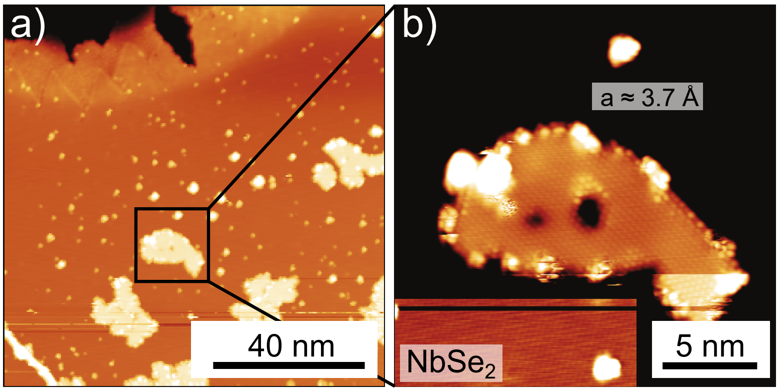

Figure 7.7: LT-STM images of <1 ML of $NiBr_2$ on $NbSe_2$ grown at room temperature. Atomic resolution of $NiBr_2$ and $NbSe_2$, the latter showing the charge density wave.

to the decomposition of the $NiBr_2$, but, as aforesaid, the high resolution XPS data show the proper, stoichiometric $NiBr_2$ phase. A closer look of one island reveals a Moiré structure with a periodicity of ≈ 6.2 nm (Fig. 7.8 b. This Moiré pattern is produced by the slight rotation angle and periodic mismatch between the $NiBr_2$ and $NbSe_2$ lattices. Its Fast Fourier Transform (FFT) is presented in Fig. 7.8 c and matches the LEED pattern in Fig. 7.9, which is hexagonal.

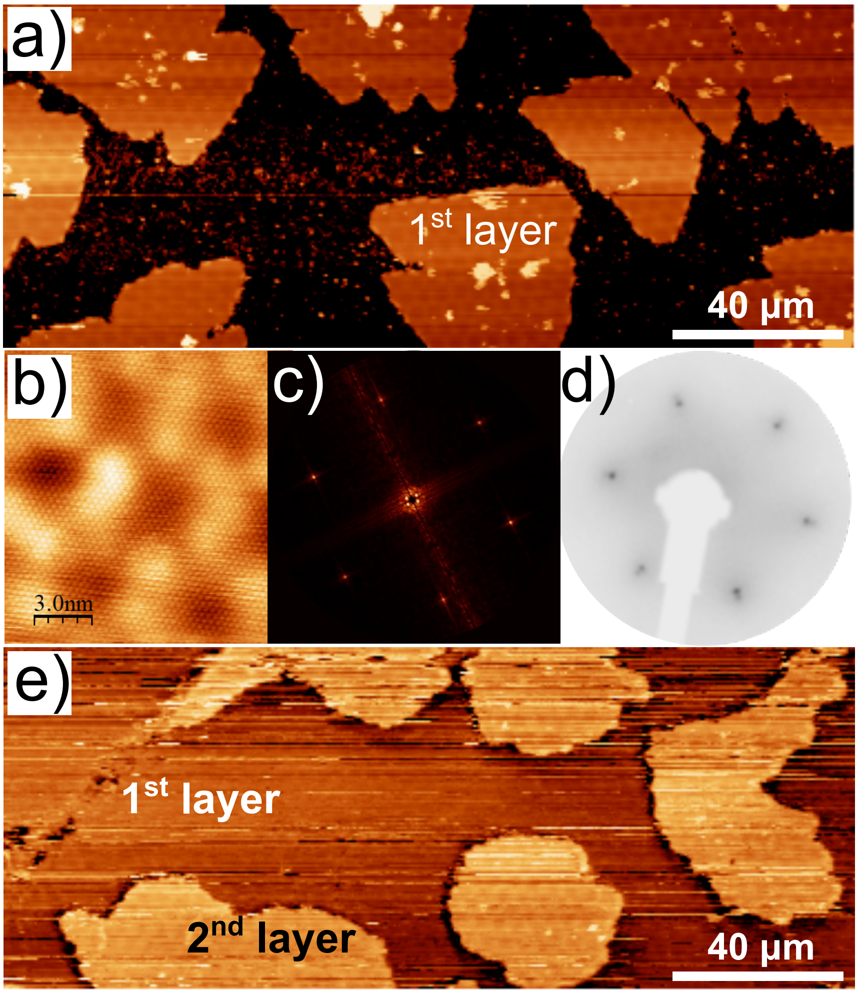

Figure 7.8: a) LT-STM image of the growth of $NiBr_2$ on $NbSe_2$ of the first layer of $NiBr_2$ on $NbSe_2$. b) Moiré. c) FFT of image. d) LEED pattern of >1 ML. e) LT-STM image of >1 ML of $NiBr_2$ on $NbSe_2$. All the samples were grown at 100 ℃.

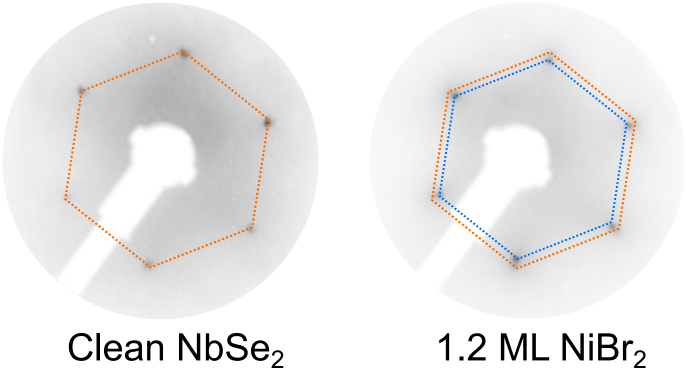

Figure 7.9: LEED pattern of bare $NbSe_2$ and >1 ML of $NiBr_2$ acquired at 137 eV. Orange hexagon indicates the pattern of $NbSe_2$ and blue hexagon, the $NiBr_2$ pattern.

7.2 Magnetic properties

The magnetic behaviour of thin films of $NiBr_2$ on both substrates (Au (111) and $NbSe_2$) was studied via XMCD. In the case of Au (111), three different coverages were explored: two submonolayered samples and a complete monolayer. Each of these two submonolayered samples is rich in one of the phases discovered via XPS (Fig. 7.1): $NiBr_x$ and the proper $NiBr_2$. The absorption spectra (XAS) and the dichroism (XMCD) signals are presented separately for each sample in Fig. 7.10 (a-c). Moreover, a comparison of the XMCD signal of the three samples is shown in Fig. 7.10 d. The shape and height of the peaks for XAS and XMCD is different for each phase, as in the XPS experiment (Fig. 7.1). The sample with the highest content in $NiBr_x$ phase has a prominent XMCD peak at ∼849.5 eV, while the submonolayered $NiBr_2$ phase-rich sample presents its main XMCD peak at ∼852 eV and a small contribution from the $NiBr_x$ phase. The thickest sample (>1 ML) only presents a XMCD peak at the same energy as the stoichiometric phase.

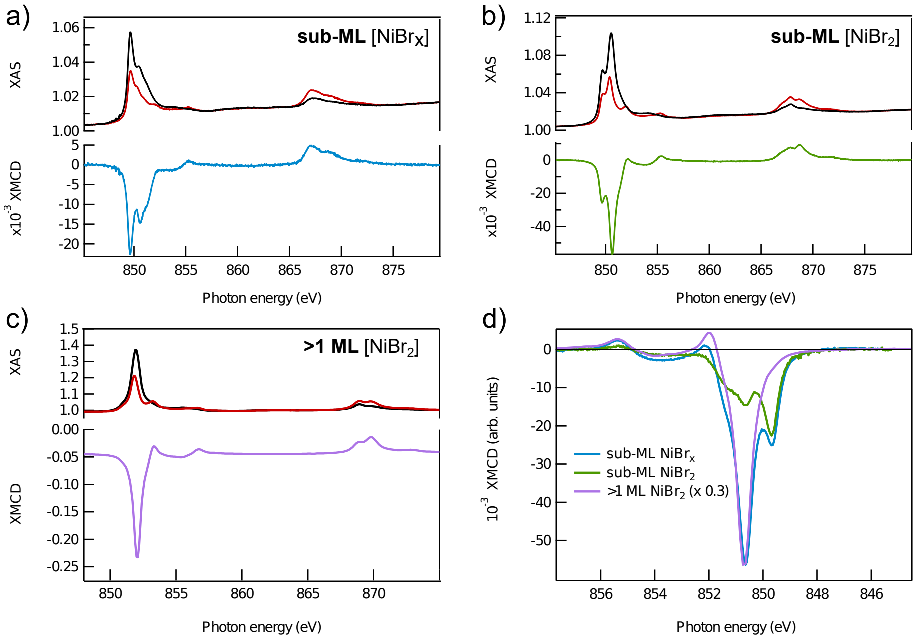

Figure 7.10: XAS and XMCD spectra at Ni $L_{2,3}$ energy for three different samples of $NiBr_2$ on Au (111): a) sub-monolayered $NiBr_2$ with the $NiBr_x$ phase, b) sub-monolayer of stoichiometric $NiBr_2$, c) more than a monolayer of $NiBr_2$ and d) comparison of the three XMCD spectra. All the samples were measured at GI, 2K and 6.5 T.

The estimated value of the spin and orbital magnetic moments was calculated from the XMCD results via sum-rules analysis, for each phase, as shown in Fig. 7.10 (a-b). Fig. 7.11 contains the curves, their integrals and the coefficients (r, p and q) needed for the calculation of the moments. The values of the moments are collected in Table 7.4

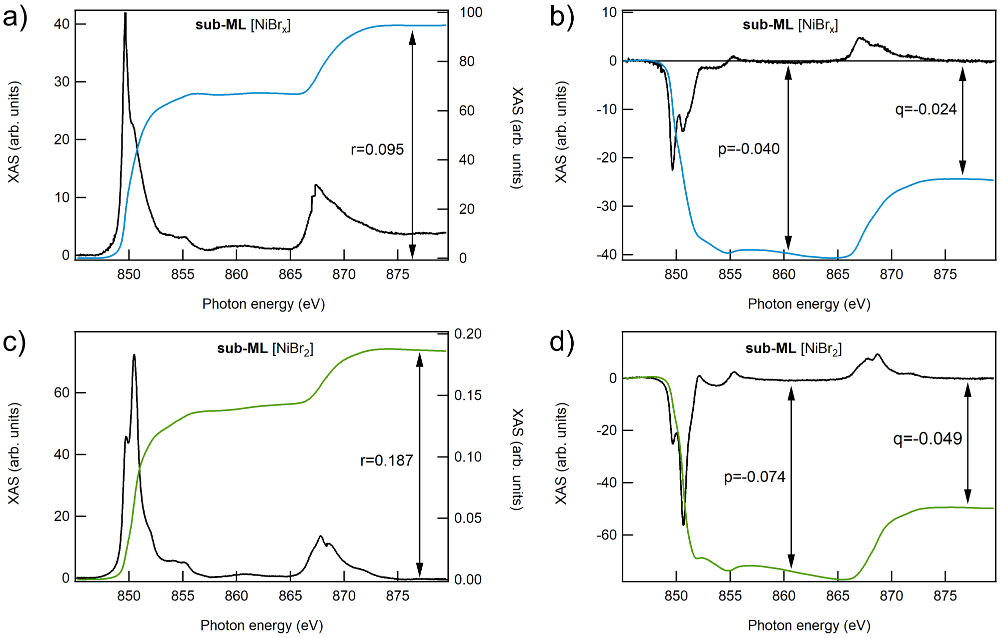

Figure 7.11: Sum-rules analysis of the XAS and XMCD spectra of the two submonolayer samples at GI measured at 2K and 6.5 T.

Table 7.2: Magnetic orbital and spin moments of $NiBr_2$ submonolayer on Au (111), measured at 6 T, 2 K and grazing incidence (70 deg).

Phase	**Magnetic moment (μ_B/Ni at)**		
	Orbital moment	**Spin moment**	**Total moment**
$NiBr_x$	0.337	1.453	1.789
$NiBr_2$	0.357	1.272	1.629

The magnetization loops were measured by sweeping the applied magnetic field ±6.5 T while measuring the x-ray absorption at the highest peak of the Ni L_3 edge (≈849.5 eV for $NiBr_x$ and ≈852 eV for $NiBr_2$). These curves were normalized to the total magnetic moment in Table 7.4.

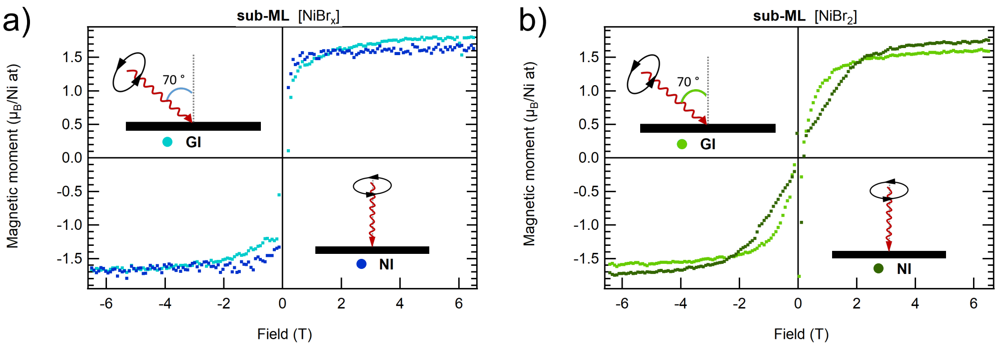

Figure 7.12: Magnetization loops for the two different phases of $NiBr_2$ grown on Au (111): a) $NiBr_x$ and b) $NiBr_2$, at two different geometries (GI and NI).

Fig. 7.12 presents the magnetization loops for both phases measured at normal and grazing incidence, at 3 K. The $\mathrm{NiBr_x}$-phase rich sample (Fig. 7.12 a) exhibits magnetic behaviour, with an almost constant remanence for NI configuration. Note that the measurements of this kind are not capable of assessing the magnetic moment close to zero field, with artifacts appearing within ±0.1 T, and therefore, a hysteresis with a coercive force in this range is not observable. However, the value of the remanence (magnetization at zero internal field) can be estimated from the XMCD experimental data. Since the $\mathrm{NiBr_x}$ phase has out-of-plane (OOP) magnetic anisotropy, the internal magnetic field is lower than the applied field by demagnetization field of the infinite plane $4\pi M$[183]. The magnetization of $\mathrm{NiBr_x}$ can be estimated using the calculated magnetic moment m= 1.8 μ_B of the Ni atom listed in the Table 7.4 and the average atomic volume of the $\mathrm{NiBr_2}$ structure[184] $\nu \approx 24\ \mathring{A}^3$. With these assumptions, demagnetization field can be calculated as:

$$4\pi M = \frac{4\pi m}{3\nu} = \frac{12 \cdot 1.8 \cdot 9.3 \cdot 10^{-21}}{3 \cdot 24 \cdot 10^{-24}} \approx 2.6 \cdot 10^3\ G = 0.26\ T \tag{7.1}$$

It must be taken into account that the $9.3 \cdot 10^{-21}$ factor appears as a consequence of converting the 1.8 μ_B to erg/G.

It means that internal field is zero when the external field is lower than 0.26 T and therefore the remanence is equal to the magnetization at 0.26 T, which is clearly visible in Fig. 7.12 a, in dark blue. Furthermore, it is easy to demonstrate that non-zero remanence does not originate from magnetic anisotropy as, for example, in the molecular magnets. Indeed, Fig. 7.12 a (light blue) allows us to estimate the value of field that saturates the magnetization in the hard magnetization direction $H_A \approx 2$ T, the so-called anisotropy field. With this value, the anisotropy energy, E_A per Ni atom can be found as[183]:

$$E_A = \frac{mH_A}{2} = \frac{1.7 \cdot 5.8 \cdot 10^{-5} \cdot 2}{2} \approx 9.9 \cdot 10^{-5}\ eV \approx 0.1\ meV \tag{7.2}$$

Using the definition $25{=}E_A/k_BT_B$[185], the superparamagnetic blocking temperature per Ni atom is:

$$T_B = \frac{E_A}{25 \cdot k_B} = \frac{1 \cdot 10^{-4}}{25 \cdot 8.6 \cdot 10^{-5}} \approx \frac{1}{20}\ K = 0.005\ K \tag{7.3}$$

This value is much lower than the temperature of measurements (≈3 K) and therefore, the magnetic anisotropy is too weak to provide a non-zero remanence as observed in Fig. 7.12a (light blue curve). As a conclussion, islands of $\mathrm{NiBr_x}$, possess a non-zero magnetic moment in zero internal magnetic field that does not increase further when an external field up to 6.5 T is applied along the out-of-plane direction at 3 K.

On the other hand, the $\mathrm{NiBr_2}$ phase shows an almost zero magnetic moment at low magnetic fields for both orientations. The nonhysteretic magnetization loop and the lack of remanent magnetization lead to discard a collinear ferromagnetic order down to 3 K in the submonolayer-thick $\mathrm{NiBr_2}$. However, the loops do not resemble the Curie-Weiss shape expected from a paramagnetic material. Indeed, the saturation field for NI is almost twice as high as for the GI geometry. The loops don't present the characteristic S-shape, but, instead, an almost linear trend of the magnetization with respect to the field until the saturation is observed. The small nonlinear contribution around zero can come from the minor amount of $NiBr_x$ phase in this sample.

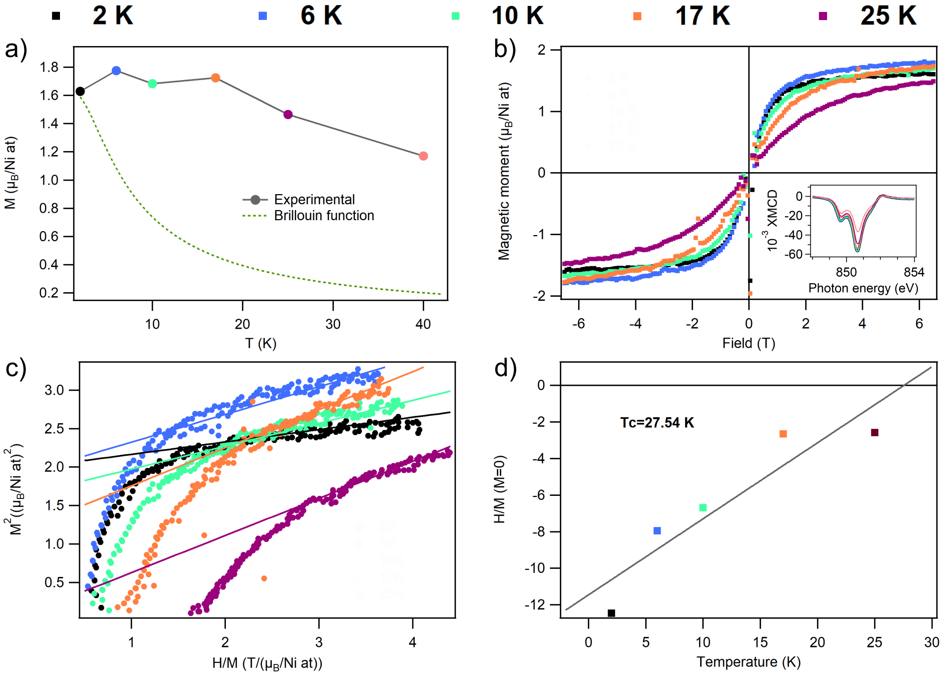

Figure 7.13: Arrott plot of the proper $NiBr_2$ phase showing a Curie temperature of about 27 K.

To further study this magnetic behaviour of $NiBr_2$, XMCD measurements at variable temperature (ranging from 2 to 25 K) were performed and displayed in Fig. 7.13 in the almost in-plane configuration (30 º off). From the sum-rules analysis, the magnetic moment of $NiBr_2$ was calculated for each temperature, and represented as a function of the temperature in Fig. 7.13 a. The decay of magnetic moment with temperature for $NiBr_2$ phase differs from the quick decay predicted by the Brillouin function for a paramagnetic material[183], discarding the paramagnetic behaviour and thus, indicating magnetic ordering of $NiBr_2$. Therefore, the Arrott plot analysis was performed to the XMCD magnetization loops at different temperatures. This is a well-defined tool that has been widely used to define the magnetic ordering of materials from their magnetization loops acquired by different techniques, including XMCD [183, 185–187], and also to estimate the transition temperature. This technique is based on the power series expansion of the thermodynamic potential close to the phase transition temperature.

$$E = MH \tag{7.4}$$

And its partial derivative:

$$\frac{\partial E}{\partial M} = H \tag{7.5}$$

Assuming that the energy close to the transition from ferromagnetic state to paramagnetic state is small, the energy can be expressed as a power series expansion of magnetic moment:

$$E \sim \frac{a}{2}M^2 + \frac{b}{4}M^4 + ... \tag{7.6}$$

Taking the partial derivative:

$$\frac{\partial E}{\partial M} \sim aM + bM^3 + ... = 0 \tag{7.7}$$

Making Eqs. 7.5 and 7.7, the result is:

$$aM + bM^3 = H \tag{7.8}$$

$$a + bM^2 = H$$

$$M^2 = \frac{1}{b}\left(\frac{H}{M} - a\right) \tag{7.9}$$

It was shown analytically that the temperature-dependent factor of the M^2 term in the expansion (a) has to be zero at the transition point. This factor is equal to the zero-field inverse magnetic susceptibility (χ). The mean field theory predicts that in the paramagnetic state, the interception will be at a positive value of H/M, while for a ferromagnetic (ordered) material this occurs at a negative value of the H/M axis. From the XMCD magnetization loops for different temperatures, a M^2 vs H/M plot can be built. The linear (high-field) part of this plot is extrapolated to the low-field region and the sign of cross with the H/M axis (hereafter, "a" factor) is extracted, as shown in Fig. 7.13 c. The a factor is represented in Fig. 7.13d, where the cross interception with the x axis determines the Curie temperature.

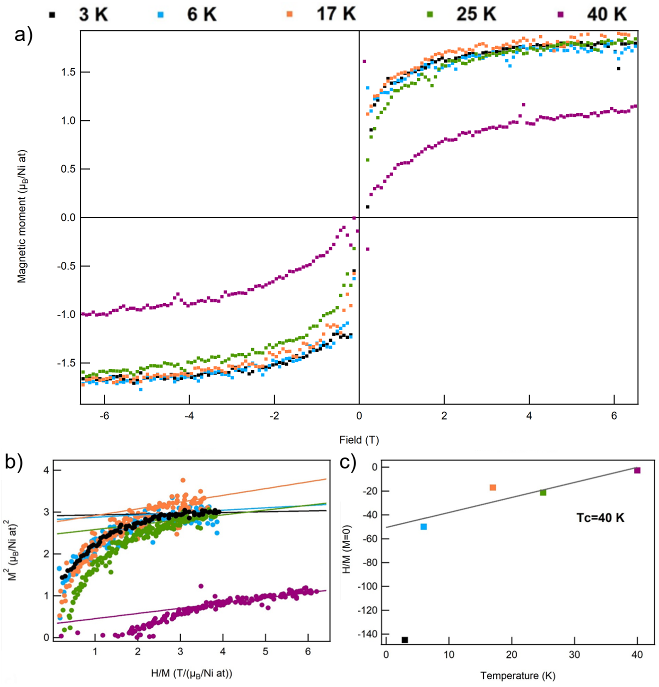

Figure 7.14: Arrott plot of the NiBr$_x$ phase showing a Curie temperature of about 40 K.

In the case of the sub-monolayered $NiBr_2$ sample, the negative intercept values prove the existence of magnetic order, whereas the linear fit of the H/M(M=0) vs T (Fig. 7.13 d) yields ≈27 K as an estimation of the Curie temperature. Modified Arrott plot technique could be also used to find the critical exponents fitting $M^{1/\beta}$ vs $(H/M)^{\gamma}$, but the presence of two phases ($NiBr_2$ and $NiBr_x$) with different Curie temperatures would undermine the precision of these data[188].

The Curie temperature of the $NiBr_x$ phase was calculated also via the Arrott plot. Fig. 7.14a displays the magnetization loops at different temperatures (3-40 K). As in the previous case, the a factor was estimated from the linear fitting of the M^2 vs H/M plot (Fig. 7.14b). The linear fitting of the a factor vs temperature plot crosses the x axis at ∼40 T, as represented in Fig. 7.14c.

The magnetic response of $NiBr_2$ deposited onto $NbSe_2$ at the sub-monolayer regime depends on the coverage, with a magnetic moment that increases from 0.46 to 1.7 μ_B/Ni atom, when the amount of $NiBr_2$ is duplicated (from 0.4 to 0.8 ML) at grazing incidence. The shape of the magnetization loops also changes with the coverage, from a more S-shaped curve to a more ferromagnetic behaviour. This can be observed in Fig. 7.15, where the magnetization loops are represented for 0.4, 0.5 and 0.8 ML.

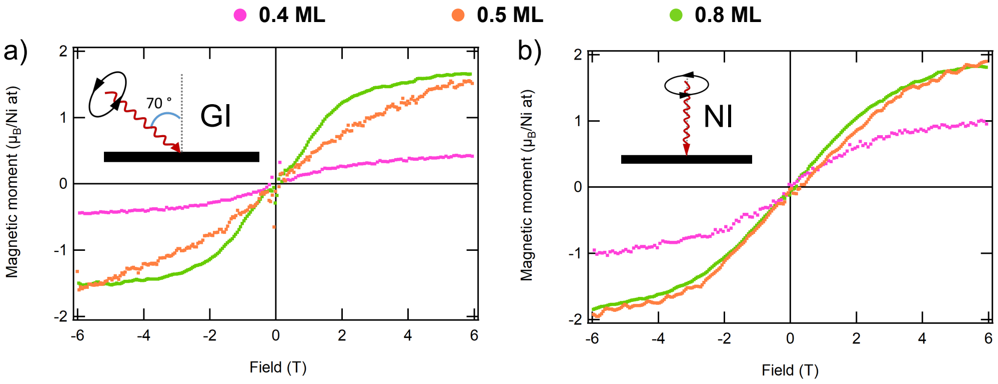

Figure 7.15: Magnetization loops of submonolayered $NiBr_2$ films on $NbSe_2$, measured at 3 K at a) grazing incidence (70 deg) and b) normal incidence (0 deg.

Moreover, taking a look at the magnetization loops at different temperatures for the sub-monolayer samples, for example for the 0.8 ML coverage (without loss of generality), a special behaviour can be observed (Fig. 7.16): the magnetic moment of $NiBr_2$ on $NbSe_2$ is lower at 3 K than at 7 K. The reason is the interaction between the magnetism of $NiBr_2$ and the superconductivity of $NbSe_2$, which lowers the magnetic moment. It is well known that $NbSe_2$ has its transition to normal state around 6 K, so above this temperature $NbSe_2$ does not interact with $NiBr_2$ and the magnetism is preserved.

The magnetic behaviour of a complete monolayer of $NiBr_2$ on $NbSe_2$ was studied in detail. The X-ray absorption spectra were measured at 6.5 T at the Ni $L_{2,3}$ edge, at 3 K, with circular polarization and represented in Fig. 7.17, as well as the whiteline and dichroism. Their integrals with the coefficients needed for the sum-rules analysis are also represented in the figure, and listed in Table 7.3.

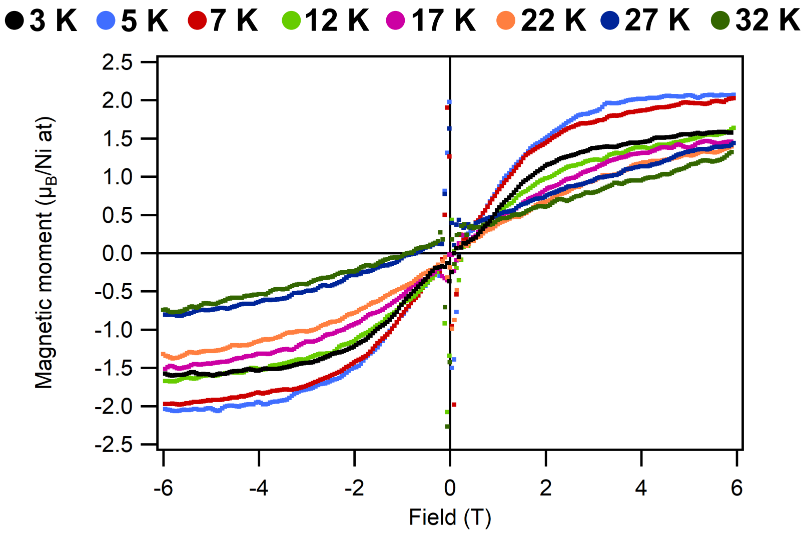

Figure 7.16: Magnetization loops of 0.8 ML of $NiBr_2$ on $NbSe_2$ measured at GI, at the Ni $L_{2,3}$ edge, for a temperature in the range of 3 to 32 K.

Table 7.3: Magnetic moments of a monolayer of $NiBr_2$ on $NbSe_2$ at 3K, 6.5 T and GI.

Magnetic moment (μ_B/Ni at)		
Orbital moment	**Spin moment**	**Total moment**
0.342	1.354	1.696

In this case, a unique $NiBr_2$ phase is obtained, with a XMCD spectrum that coincides with the $NiBr_2$ phase grown on Au (111), confirming the XPS results.

The magnetization loops, measured under a magnetic field of ±6.5 T, at 3 K, at grazing and normal incidence are displayed in Fig. 7.18. These loops resemble the curves for the $NiBr_2$ phase in Au (111) presented in Fig. 7.12 b: magnetization loops exhibiting a linear trend at low values of magnetic field, with no remanence or hysteretic behaviour in any orientation. Also, with the saturation of the moment at normal incidence at double field than for grazing incidence. The only change between the $NiBr_2$ phase in Au (111) and in $NbSe_2$ is that the former presented a small contribution from the $NiBr_x$ phase, as a non-linear response at low fields, while in $NbSe_2$ the trend is fully linear.

In order to calculate the Curie temperature of this phase and compare with the case in Au (111), the Arrott plot analysis was performed at grazing incidence as represented in Fig. 7.19. The estimated value of the Curie temperature is ≈ 20 K, while for $NiBr_2$/Au (111) was 27 K. This difference is attributed to the already mentioned contribution of $NiBr_x$ phase in Au (111).

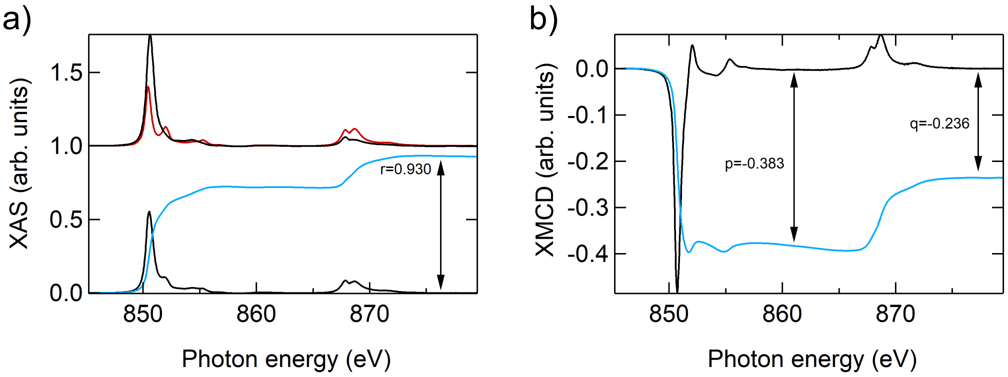

Figure 7.17: Sum-rules calculation for 1.2 ML of $NiBr_2$ on $NbSe_2$ measured at 2 K, 6.5 T and GI.

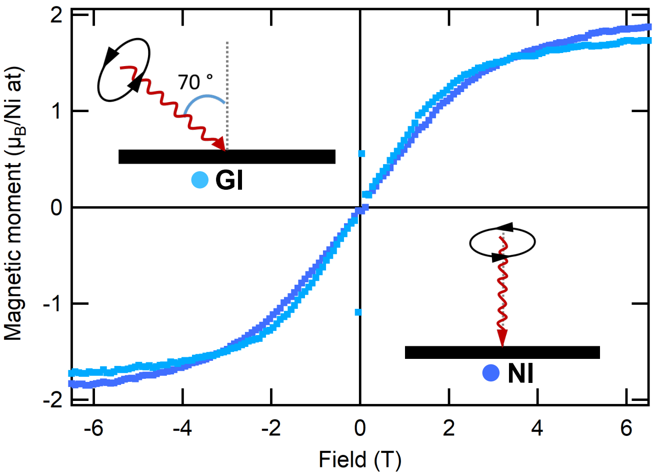

Figure 7.18: Hysteresis loops of 1 ML of $NiBr_2$ on $NbSe_2$ for the two different geometries (GI and NI).

7.3 Comparison with a different transition metal dihalide, $FeBr_2$

As introduced in Chapter 3, $FeBr_2$ is a layered van de Waals transition metal dihalide, with a predicted magnetic moment of 4 μ_B/Fe at, and preferred orientation of the magnetic moments along out of plane axis.

The growth of $FeBr_2$ on Au (111) has been studied in detail in [189], via a combination of surface science techniques such as LEED, LT-STM, XPS, PEEM or LEEM. $FeBr_2$ exhibits a reconstruction in LEED for the first layer (Fig. 7.20 a-b), as happened for $NiBr_2$. However, the islands of $FeBr_2$ grow directly on the Au surface, without any decomposed phase between the island and the substrate, as shown via LT-STM in Fig. 7.20 c, where the Herringbone reconstruction of Au (111) is observed between the islands. The second layer of $FeBr_2$ (Fig. 7.20 d) grows flat, on top of the first. This result is corroborated by the XPS spectra, which demonstrate that in $FeBr_2$, Fe is in the 2+ oxidation state, and a stoichiometric phase (proportion

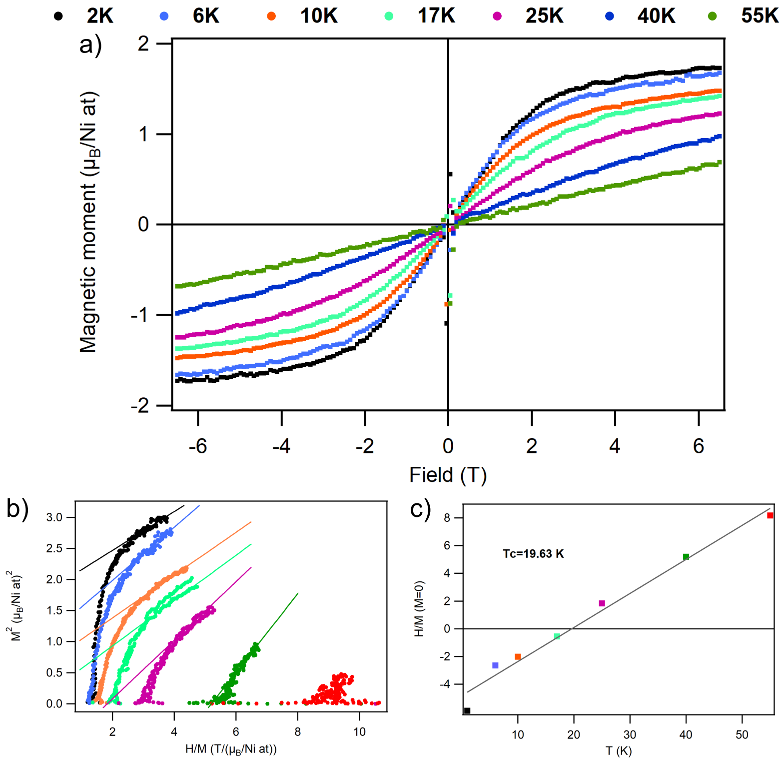

Figure 7.19: Hysteresis loops for 1 ML of $NiBr_2$ on $NbSe_2$ at different temperatures (ranging from 2 to 55 K), measured at GI. Arrott plot and procedure to estimate the Curie temperature.

Fe:Br close to 0.5) is calculated. In the PEEM/LEEM experiment, islands on the micrometer scale were observed, with the substrate at room temperature during the deposition, while in $NiBr_2$/Au(111) the islands at room temperature were too small and the temperature had to be increased to 100 °C.

When $FeBr_2$ is deposited on $NbSe_2$, a Moiré pattern is observed, as expected from a bidimensional material growing on top of another with a slight mismatch in their lattices. The STM images in Fig. 7.21 (a-b) show this Moiré, together with the atomic resolution, displaying an atomic distance of $\approx$3.9 nm. In the XPS spectrum acquired at the Fe $2p$ core level (Fig. 7.21 c), Fe exhibits the proper 2+ oxidation state.

To establish a comparison between the magnetic behaviour of $NiBr_2$ and $FeBr_2$, XMCD measurements were performed. The XAS signal was acquired at the Fe $L_{2,3}$ edge, using circular polarization, at 2 K and under an applied magnetic field of 6 T, for $FeBr_2$ deposited onto the two different substrates. The whiteline (average signal between right and left circular polarizations) and the XMCD (difference between the spectra) are displayed in Fig. 7.23, as well as their integrals. The coefficients needed for the sum rules analysis are also included in the figure. The magnetic moments calculated from the integrals are collected in Table 7.4.

These magnetic moments differ from the expected 4 μ_B/Fe atom for bulk $FeBr_2$, being lower for the case of $FeBr_2$/Au (111). This is explained in [189], where the reduced magnetic moment of the sub-monolayered $FeBr_2$ was attributed to a spin

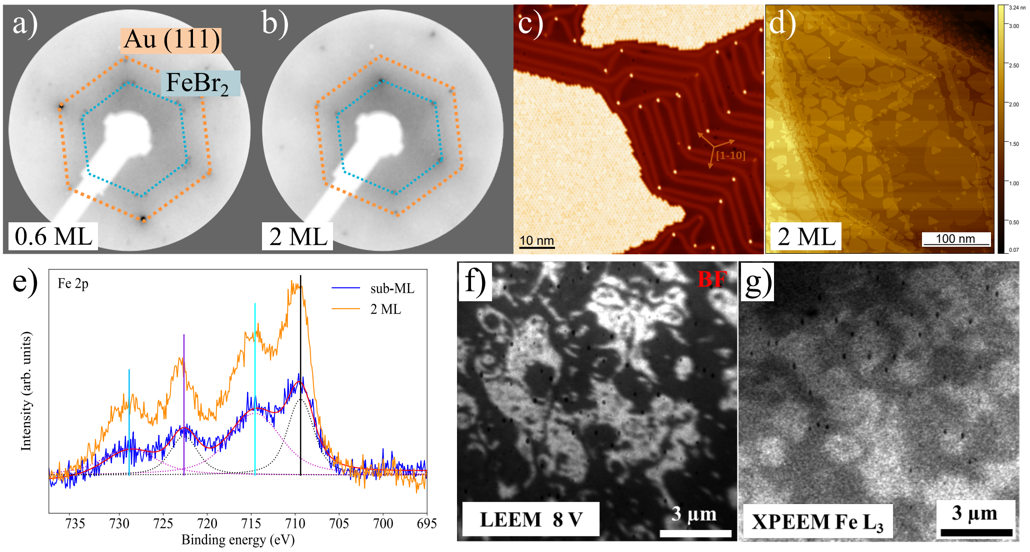

Figure 7.20: The growth of FeBr$_2$ on Au (111): from submonolayer to multilayer: (a-b) LEED patterns at 137 eV. (c-d) Low temperature STM. e) XPS spectra at Fe 2p core level. f) LEEM image at bright field. g) XPEEM image at the Fe L$_{2,3}$ edge.

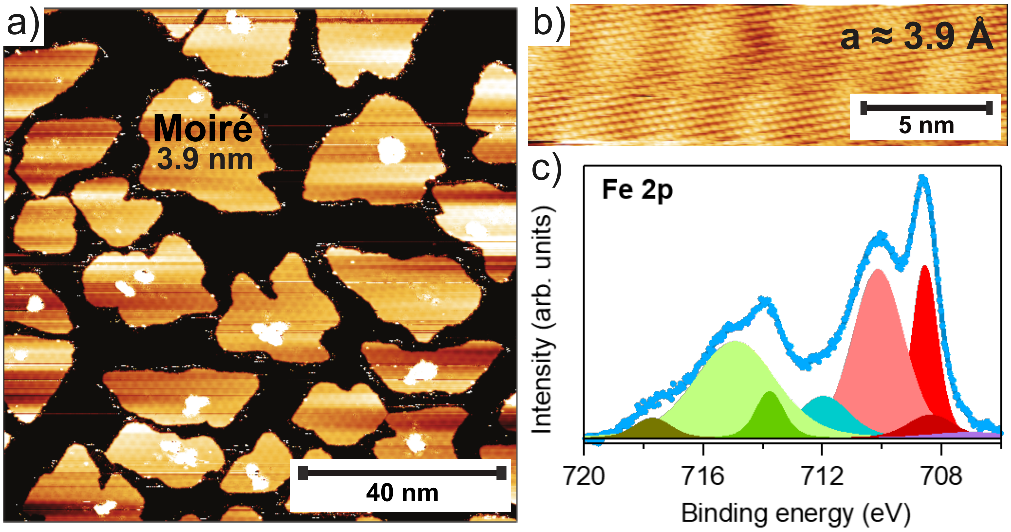

Figure 7.21: The growth of FeBr$_2$ on NbSe$_2$: (a-b) Low temperature STM images of submonolayered coverage. c) XPS spectrum at the Fe 2p core level, showing an unique phase.

frustration. The magnetic moment for thicker samples (above 1 ML) was shown to be higher, demonstrating that the first layer contributed to the decrease of the magnetic moment while the second layer has a magnetic moment of $\sim$3.3 μ_B/Fe atom.

The magnetization loops of FeBr$_2$ on Au (111) and NbSe$_2$ at the monolayer regime are presented in Fig. 7.22 a and b, respectively. The loops are normalized to the magnetic moments in Tab. 7.4. As aforementioned, the saturation magnetic moments are lower than expected. Moreover, the loops for FeBr$_2$/Au (111) have

Table 7.4: Magnetic orbital and spin moments of $FeBr_2$ monolayers on Au (111) and $NbSe_2$ substrates.

Substrate	**Orientation**	**Magnetic moment (μ_B/Fe at)**		
		Orbital moment	**Spin moment**	**Total moment**
Au (111)	NI	0.53	2.07	2.61
	GI	0.46	2.12	2.58
NbSe2	NI	0.76	2.47	3.23
	GI	0.53	2.10	2.62

a similar shape for both geometries, while in the case of $FeBr_2/NbSe_2$ the curve saturates at lower field in the NI configuration than in the GI. Again, this material exhibits an almost zero magnetic moment at low field for the two orientations, thus discarding the collinear ferromagnetic ordering.

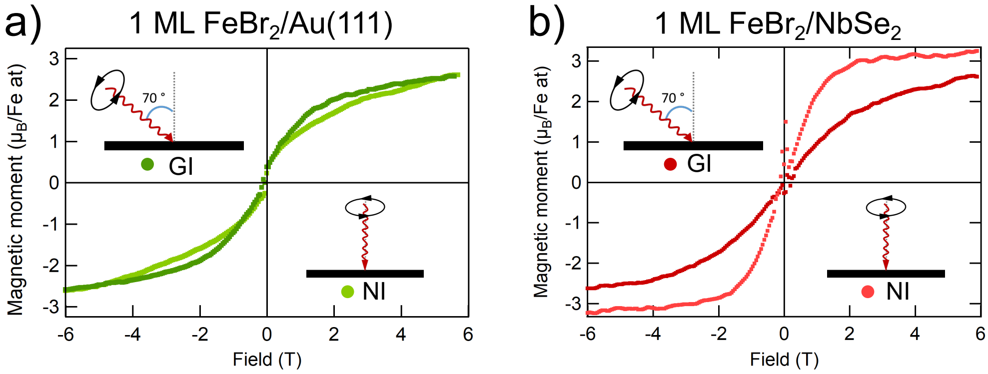

Figure 7.22: Magnetization loops of $FeBr_2$ on a) Au (111) and b) $NbSe_2$. The curves were acquired at the Fe $L_{2,3}$ edge, at 2 K and different geometries (normal and grazing incidence).

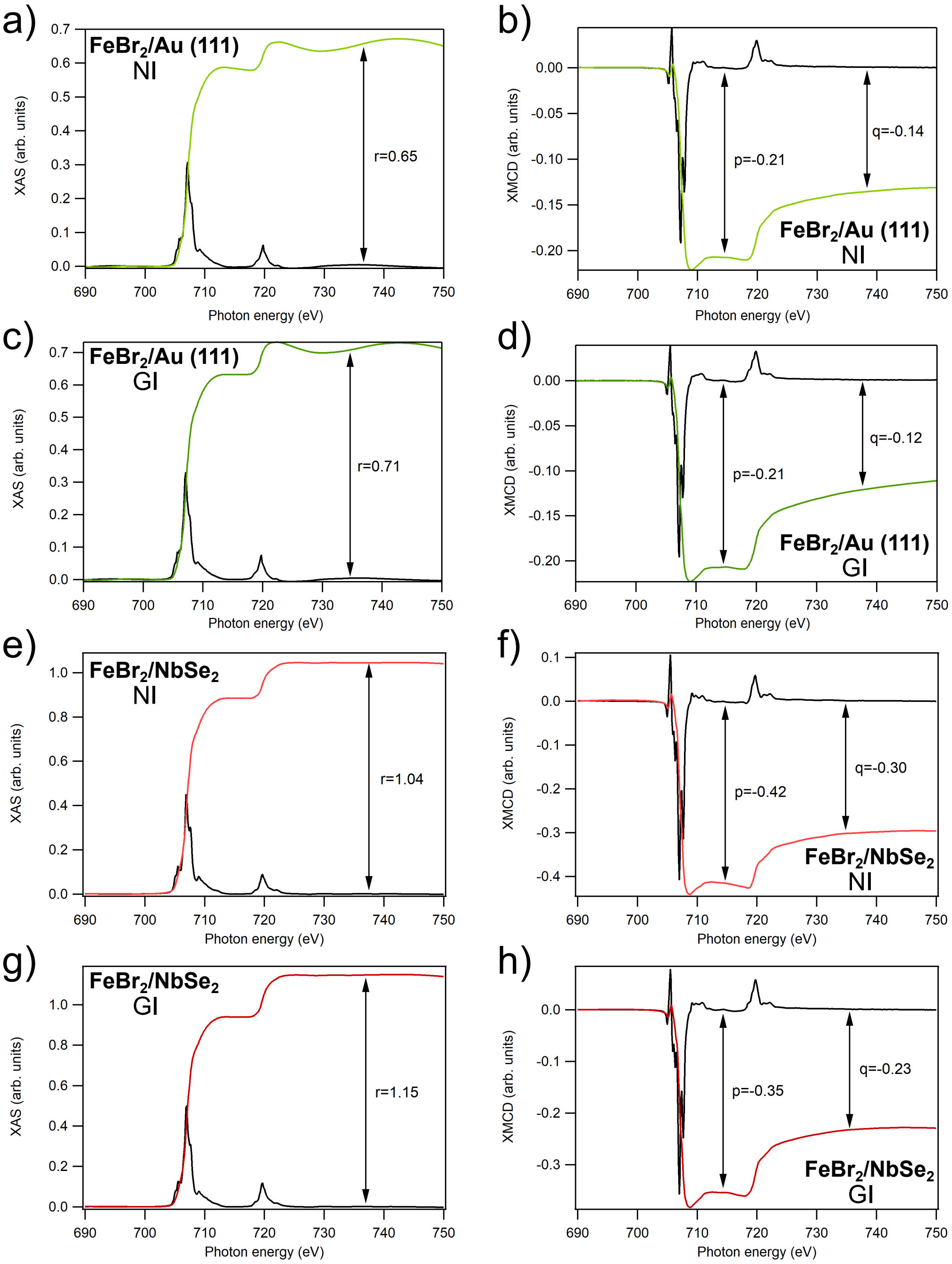

Figure 7.23: XAS and XMCD spectra of 1 ML of $FeBr_2$ on Au (111) (green) and $NbSe_2$ (red), measured at 6 T, 2K at normal and grazing incidence.

7.4 Implementation in devices: the supercurrent diode

As aforesaid, the work presented in this chapter is mainly focused on the characterization of this new class of materials, however, in this section, the first implementation in a device will be presented. This work was done in collaboration with the group of Dr. F. Giazzoto and Dr. E. Strambini, as the Master Thesis of T. Angeloni [190], from Scuola Normale Superiore di Pisa. The aim was to demonstrate a superconducting diode behaviour.

A conventional superconductor is characterized by a zero resistance state, where the current (called supercurrent) does not dissipate. This supercurrent is usually reciprocal, meaning that the maximal amount of supercurrent can be sustained both in the forward and in the backward direction. Recently, research is focused to create a non-reciprocal superconducting device, named supercurrent diode. This device ideally sustains supercurrent in one direction and transitions to the normal state for the opposite direction. The aim of this work is to achieve diode properties in a superconducting Al wire, by inducing a magnetochiral anisotropy when placed in contact with $NiBr_2$, which was demonstrated to exhibit non-collinear magnetic order [191].

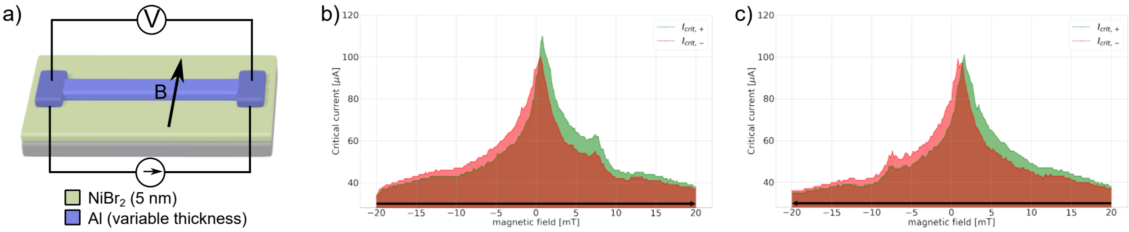

Figure 7.24: a) Sketch of the supercurrent diode. b-c) Absolute value of the positive (green) and negative (red) critical currents measured for an Al/$NiBr_2$ bilayer, in orthogonal magnetic field at 100 mK. The external field was swept: b) from -20 mT to 20 mT, c) from 20 mT to -20 mT.

In the experiment, the critical current of each sample was measured, as a function of the applied magnetic field and the temperature in the cryostat. The current was injected in the aluminium strip, ramping the source from zero to an increasing current. Simultaneously, the voltage drop across the strip was measured, as displayed in Fig. 7.24 a. The critical current is the minimum value of the current on the ramp at which a meaningful voltage drop is measured.

When an external magnetic field is applied, a clear diode effect is visible, as represented in Fig. 7.24 (b-c). For instance, applying 6 mT of orthogonal in plane field (as in the sketch of Fig. 7.24 a), the negative critical current is greater (in magnitude) with respect to the positive one, demonstrating the non reciprocity of the supercurrent, while reversing the field swaps the role of the positive and negative critical currents, $I_{C,+}$ and $I_{C,-}$, as expected from the time reversal symmetry $I_{C,+}(B) = I_{C,-}(-B)$. The observed asymmetry is around 15 %. In [190], more details about the dependence of the effect on the temperature and thickness of the Al strip can be found.

Summary

The growth of bidimensional transition metal dihalides, down to the submonolayer regime was followed via a combination of ultra high vacuum techniques such as XPS, LEED, LT-STM and LEEM/PEEM. The magnetism has been explored *in situ* by XMCD.

The first layer of $NiBr_2$ has shown to grow onto Au (111) in two different phases: the proper, stoichiometric $NiBr_2$ and a debrominated phase, $NiBr_x$. The first of them exhibits a non-collinear magnetic ordering, while the second is ferromagnetic. The Curie temperature of both phases was measured via the Arrott plot analysis, estimating a value of 27 K and 40 K for $NiBr_2$ and $NiBr_x$, respectively. For thicker coverages, only the proper $NiBr_2$ phase is deposited.

On the superconducting $NbSe_2$ substrate, $NiBr_2$ presents the stoichiometric phase from the submonolayer, with the saturation magnetic moments increasing with the coverage. The interaction between superconductivity and magnetism is observed in the $NiBr_2/NbSe_2$ bilayers, as a lower magnetic moment below the transition temperature of $NbSe_2$. When more than a layer is deposited, the same non-collinear magnetic ordering as in Au (111) is exhibited.

Moreover, another material of the same class was studied: $FeBr_2$, onto the same two substrates (Au (111) and $NbSe_2$). This material does not present the debrominated phase when it is grown on Au (111) nor on $NbSe_2$. However, the magnetic measurements do not show a collinear ferromagnetic ordering.

In summary, the transition metal dihalides are a promising class of materials that exhibit magnetic behaviour down to the submonolayer regime, with reproducible results, independent of the preparation conditions, with an easy method to be deposited onto different substrates. These materials still need to be explored when implemented in different devices.

Chapter 8

Concluding remarks and outlook

As aforementioned, the emergence of new quantum technologies is closely linked to the development of new materials to fulfill the requirements of the applications. To develop these materials, an exhaustive study of their production and properties is needed. For that purpose, surface science techniques are a powerful tool, leading to a controlled growth and characterization of materials at the nanoscale. However, there seems to be a gap between materials science and nanotechnology, being only few works relating the properties of the materials and the performance of the devices where they are implemented, resulting in a lack of reproducibility of the results and a poor understanding of the effects that take place.

This thesis establishes a link between surface science and the fabrication and characterization of devices, remarking the importance of controlling the materials and their interfaces at the nanoscale. By means of a combination of *in situ* and *ex situ* characterization techniques, accompanied by the measurement of the electrical response of the tunnel junctions, the impact of the preparation conditions on the properties of the materials and interfaces and, in turn, on the performance of these junctions has been proven.

Throughout this work, the ability to tune the properties of the materials via the preparation conditions, understanding how each condition affect the properties and how each property has, in turn, an impact on the performance of the device has been highlighted. This control at the nano- and mesoscale has demonstrated a positive impact enhancing the performance of the devices, together with a higher reproducibility of results.

Concerning the results from the chapters about EuS, thanks to the tuning of the properties of this ferromagnetic insulator via the preparation conditions, the giant thermoelectric effect has been demonstrated, together with the rectification effect, even in the absence of an applied magnetic field, understanding why sometimes devices do not work or show a lowered spin-splitting of the density of states. Moreover, the applicability of EuS has been demonstrated in various experiments, by collaborating with other groups, experts in spintronics, which needed a ferromagnetic insulator. In addition to this, from a more technical point of view, the implementation of the manipulator and the shadow masks, the integration of the plasma chamber to produce oxides and the improvement of the preparation chamber to fabricate the tunnel junctions opens up the door to fabricate other junctions, consisting in different materials, which can be characterized *in situ*, without breaking the vacuum. The expertise gained by the members of the group during my phD, leaded them to start new collaborations and projects, even buying a dilution fridge to perform tunnel spectroscopy measurements in junctions.

Therefore, the research does not finish after this thesis, but starts in several different paths that will be shortly discussed next.

The superted radiation sensor for imaging and spectroscopy

The first proof of concept of the thermoelectric effect in the junctions based in Al/EuS bilayer is the first step to obtain the radiation sensor. However, further research on this detector has to be performed. On the one hand, the sensitivity of the detector has to be improved, by carrying out more experiments on the implementation of the tunnel junctions in both, the THz and X-ray detector. On the other hand, the multiplexing has to be explored. The multiplexing is the capability to be operated as a sensor-array with readout-multiplexing. For that purpose, the continuation of superted project, extending the collaboration with Pisa, Jyväskylä and Grenoble is needed.

The development of materials for quantum technologies

The expertise in fabricating Al/EuS/InAs heterostructures, demonstrated in this thesis, will be exploited to fabricate spin qubits consisting in InAs nanowires partially covered by Al and EuS. These qubits will be measured in the new dilution fridge, recently bought to perform electric measurements at very low temperatures, as the tunneling measurements presented in chapter 5.

As aforesaid, magnons are important for quantum technologies, since they can be used for quantum information processing and communication. They could be used in qubits because they possess long coherence times and it is possible to manipulate, as well as have the potential to be used in quantum sensing, where they can be used to measure magnetic fields with high precision. Concerning the results of the magnon transport in EuS, a possible application is to measure very small magnetic fields in combination with SQUIDs (Superconducting Quantum Interference Devices). These could potentially lead to improved quantum sensing and measurement capabilities and are commonly used in a variety of applications, such as medical imaging and geophysical exploration. This research line already started, in collaboration with the group of Q-MAD of Universidad de Zaragoza.

The growth and characterization of bidimensional magnetic materials

The bidimensional transition metal dihalides have demonstrated a big potential, with intringuing physical properties down to the submonolayer regime. The easy deposition method to grow these materials, accompanied by the proven magnetic behaviour at the monolayer make this class of materials interesting to study via surface science. Therefore, the research on different materials of this class such as diclorides or dibromides of Co or Mn will be followed by different students of our group. Moreover, the electronic properties will be explored via ARPES and calculations to understand these properties will be performed by another student of the group.

The applications of bidimensional magnetic semiconductors

Given the good results on the first implementation of $NiBr_2$ in a device (the supercurrent diode), this material, together with the rest of the family are potential candidates to build up new devices which need flat surfaces and non-collinear magnetic ordering. Although the EuS/Al bilayer has been demonstrated to exhibit the proximity effect, the exhaustive control of the preparation conditions necessary to deposit the EuS to fabricate the junctions make this process difficult to follow and scale up to the industry, motivating the possible implementation of these bidimensional magnetic materials in the tunneling junctions explored throughout this thesis.

Therefore, this thesis has been the first of a big saga of works related with the research on materials for quantum technologies, establishing the first steps to grow and characterize materials of these classes, producing the first tunnel junctions and starting collaborations that will be very fruitful for the group.

List of publications

1. C González-Orellana, M Peña-Díaz, M Gobbi, P Gargiani, M Ipatov, A Chuvilin, C Munuera, A Larrañaga-Varga, M Ilyn and C Rogero **Fine-tuning Ferromagnetism of EuS nanolayers through growth parameters control.** *In preparation.*

2. C González-Orellana, D Bikaljevic, AJ Thakur, A Weber, D Streiner, P Gargiani, J Dreiser, JI Pascual, C Rogero and M Ilyn. **Single-layer magnetism of epitaxial NiBr2 salt on NbSe2.** *In preparation.*

3. A Aguirre, A Pinar, C González-Orellana, J Ortuzar, O Stesovych, M Peña-Díaz, J Dreiser, M Muntwiler, C Rogero, JI Pascual, P Jelínek, M Ilyn and M Corso. **Tunable ferromagnetic order in 2D layers of Transition Metal Dichlorides.** *In preparation.*

4. SE Hadjadj, C González-Orellana, J Lawrence, D Bikaljević, M Peña-Díaz, P Gargiani, L Aballe, J Naumann, MA Niño, M Foerster, S Ruíz-Gómez, S Thakur, I Kumberg, J Taylor, J Hayes, J Torres, C Luo, F Radu, DG de Oteyza, W Kuch, JI Pascual, C Rogero and M Ilyn. **Epitaxial monolayers of magnetic 2D semiconductor FeBr grown on Au(111).** *arXiv preprint arXiv:2304.11972, April 2023.*

5. MX Aguilar-Pujol, S Catalano, C González-Orellana, W Skowronski, M Gómez-Pérez, M Ilyn, C Rogero, M Gobbi, LE Hueso and F Casanova. **Magnon currents excited by the spin Seebeck effect in ferromagnetic EuS thin films.** *arXiv preprint arXiv:2303.03833, March 2023.*

6. Z Geng, A Hijano, S Ilic, M Ilyn, I J Maasilta, A Monfardini, M Spies, E Strambini, P Virtanen, M Calvo, C González-Orellana, AP Helenius, S Khorshidian, CI Levartoski de Araujo, F Levy-Bertrand, C Rogero, F Giazotto, FS Bergeret and TT Heikkila. **Superconductor-ferromagnet hybrids for non-reciprocal electronics and detectors.** Review article. *arXiv preprint arXiv:2302.12732, February 2023.*

7. E Strambini, M Spies, N Ligato, S Ilić, M Rouco, C González-Orellana, M Ilyn, C Rogero, FS Bergeret, JS Moodera, P Virtanen, TT Heikkilä and F Giazotto. **Superconducting spintronic tunnel diode.** *Nature communications 13 (1), 2431, May 2022.*

8. D Bikaljevic, C González-Orellana, M Peña-Díaz, D Steiner, J Dreiser, P Gargiani, M Foerster, MA Niño, L Aballe, S Ruíz-Gómez, N Friedrich, J Hieulle,

L Jingcheng, M Ilyn, C Rogero and JI Pascual. **Noncollinear Magnetic Order in Two-Dimensional NiBr2 Films Grown on Au(111).** *ACS nano 15 (9), 14985-14995, September 2021.*

9. A Hijano, S Ilic, M Rouco, C González-Orellana, M Ilyn, C Rogero, P Virtanen, TT Heikkilä, S Khorshidian, M Spies, N Ligato, F Giazotto, E Strambini and FS Bergeret **Coexistence of superconductivity and spin-splitting fields in superconductor/ferromagnetic insulator bilayers of arbitrary thickness.** *Physical Review Research 3 (2), 023131, May 2021.*

10. JM Gómez-Pérez, X Zhang, F Calavalle, M Ilyn, C González-Orellana, M Gobbi, C Rogero, A Chuvilin, VN Golovach, LE Hueso, FS Bergeret and F Casanova **Strong interfacial exchange field in a heavy metal/ferromagnetic insulator system determined by spin Hall magnetoresistance.** *Nano Letters 20 (9), 6815-6823, July 2020.*

11. AO Fumega, M Gobbi, P Dreher, W Wan, C González-Orellana, M Peña-Díaz, C Rogero, J Herrero-Martín, P Gargiani, M Ilin, MM Ugeda, V Pardo and S Blanco-Canosa. **Absence of ferromagnetism in VSe caused by its charge density wave phase.** *Journal of Physical Chemistry C 2019, 123, 45, 27802–27810, July 2019*

Bibliography

[1] G. J. Ferreira et al., “Magnetically defined qubits on 3d topological insulators”, Physical review letters **111**, 106802 (2013).

[2] S. Kawabata et al., “Macroscopic quantum dynamics of π junctions with ferromagnetic insulators”, Phys. Rev. B **74**, 180502 (2006).

[3] M. Tsang, “Quantum transition-edge detectors”, Phys. Rev. A **88**, 021801 (2013).

[4] J. Baselmans, “Kinetic inductance detectors”, Journal of Low Temperature Physics **167**, 292–304 (2012).

[5] *Thermoelectric detector based on superconductor-ferromagnet heterostructures*, 2018.

[6] A. Ozaeta et al., “Predicted very large thermoelectric effect in ferromagnet-superconductor junctions in the presence of a spin-splitting magnetic field”, Phys. Rev. Lett. **112**, 057001 (2014).

[7] S. Kolenda et al., “Observation of thermoelectric currents in high-field superconductor-ferromagnet tunnel junctions”, Physical review letters **116**, 097001 (2016).

[8] T. Chang, “Proximity effect in electron-beam lithography”, Journal of vacuum science and technology **12**, 1271–1275 (1975).

[9] A. I. Buzdin, “Proximity effects in superconductor-ferromagnet heterostructures”, Reviews of modern physics **77**, 935 (2005).

[10] F. Bergeret et al., “Odd triplet superconductivity and related phenomena in superconductor-ferromagnet structures”, Reviews of modern physics **77**, 1321 (2005).

[11] J. Linder et al., “Superconducting spintronics”, Nature Physics **11**, 307–315 (2015).

[12] E. Strambini et al., “Revealing the magnetic proximity effect in eus/al bilayers through superconducting tunneling spectroscopy”, Phys. Rev. Materials **1**, 054402 (2017).

[13] S. M. Rossnagel, “Thin film deposition with physical vapor deposition and related technologies”, Journal of Vacuum Science & Technology A **21**, S74–S87 (2003).

[14] *Mbe komponenten cold lip effusion cell.*

[15] C. Fadley, “Basic concepts of x-ray photoelectron spectroscopy”, Electron spectroscopy: theory, techniques and applications **2**, 1–156 (1978).

[16] A. Grosvenor et al., “The influence of final-state effects on xps spectra from first-row transition-metals”, in , Vol. 59 (Jan. 2016), pp. 217–262.

[17] T. Shirasawa, "Surface analysis — low-energy electron diffraction", in *Encyclopedia of analytical science (third edition)*, edited by P. Worsfold et al., Third Edition (Academic Press, Oxford, 2019), pp. 365–373.

[18] F. Jona et al., "Low-energy electron diffraction for surface structure analysis", Reports on Progress in Physics **45**, 527–585 (1982).

[19] H. Rohrer et al., "Scanning tunneling microscopy", IBM Journal of Research and Development **30.4**, 335 (1986).

[20] M. Schmid, *Skecth of a scanning tunneling microscope.*

[21] F. De Groot, "Multiplet effects in x-ray spectroscopy", Coordination Chemistry Reviews **249**, 31–63 (2005).

[22] J. Lang, "X-ray magnetic circular dichroism", in *Characterization of materials* (John Wiley & Sons, Ltd, 2002).

[23] C. T. Chen et al., "Experimental confirmation of the x-ray magnetic circular dichroism sum rules for iron and cobalt", Phys. Rev. Lett. **75**, 152–155 (1995).

[24] C. Mainka et al., "Linear dichroism in x-ray absorption spectroscopy of strongly chemisorbed planar molecules: role of adsorption induced rehybridisations", Surface science **341**, L1055–L1060 (1995).

[25] T. O. Menteş et al., "Angle-resolved x-ray photoemission electron microscopy", Journal of Electron Spectroscopy and Related Phenomena **185**, 323–329 (2012).

[26] A. Sala et al., "Defects and inhomogeneities in fe 3 o 4 (111) thin film growth on pt (111)", Physical Review B **86**, 155430 (2012).

[27] E. Bauer, "Low energy electron microscopy", Reports on Progress in Physics **57**, 895–938 (1994).

[28] B. P. Tonner et al., "Photoelectron microscopy with synchrotron radiation", Review of Scientific Instruments **59**, 853–858 (1988).

[29] E. Bauer, *Surface microscopy with low energy electrons*, Vol. 23 (Springer, 2014).

[30] P. Eaton et al., *Atomic force microscopy* (Oxford university press, 2010).

[31] D. Rugar et al., "Atomic force microscopy", Physics Today **43**, 23–30 (1990).

[32] *Skecth of an atomic force microscope.*

[33] *Lake shore cryotonics.*

[34] A. Niazi et al., "A precision, low-cost vibrating sample magnetometer", Current Science-Bangalore **79**, 99–109 (2000).

[35] J. K. Krause et al., "Understanding magnetic measurement techniques", Superconductor Industry **3**, 2326 (1990).

[36] J. K. Krause, "Extraction magnetometry in an ac susceptometer", IEEE transactions on magnetics **28**, 3066–3071 (1992).

[37] H. Wang et al., "Electronic structure and magnetic ordering of the semiconducting chromium trihalides crcl3, crbr3, and cri3", Journal of physics. Condensed matter : an Institute of Physics journal **23**, 116003 (2011).

[38] L. J. Cornelissen et al., “Magnon spin transport driven by the magnon chemical potential in a magnetic insulator”, Physical Review B **94**, 014412 (2016).

[39] E. Villamor et al., “Modulation of pure spin currents with a ferromagnetic insulator”, Physical Review B **91**, 020403 (2015).

[40] L. López-Mir et al., “Anisotropic sensor and memory device with a ferromagnetic tunnel barrier as the only magnetic element”, Scientific Reports **8**, 861 (2018).

[41] K. Mizunuma et al., “Mgo barrier-perpendicular magnetic tunnel junctions with cofe/pd multilayers and ferromagnetic insertion layers”, Applied Physics Letters **95**, 232516 (2009).

[42] S. Yuasa et al., “Giant tunnel magnetoresistance in magnetic tunnel junctions with a crystalline mgo (0 0 1) barrier”, Journal of Physics D: Applied Physics **40**, R337 (2007).

[43] C. Y. Guo et al., “Magnon valves based on yig/nio/yig all-insulating magnon junctions”, Phys. Rev. B **98**, 134426 (2018).

[44] B. Matthias, “Rm bozorth and jh van vleck”, Phys. Rev. Lett **7**, 160 (1961).

[45] S. V. Houten, “Magnetic interaction in eus, euse, and eute”, Phys. Letters **2**, `10.1016/0031-9163(62)90231-7` (1962).

[46] K. S. Novoselov et al., “Electric field effect in atomically thin carbon films”, science **306**, 666–669 (2004).

[47] M. Lu et al., “Mechanical, electronic, and magnetic properties of nix2 (x = cl, br, i) layers”, ACS omega **4**, 5714–5721 (2019).

[48] M. Mushtaq et al., “Nix 2 (x = cl and br) sheets as promising spin materials: a first-principles study”, RSC Advances **7**, 22541–22547 (2017).

[49] B. L. Chittari et al., “Electronic and magnetic properties of single-layer mpx3 metal phosphorous trichalcogenides”, Physical Review B **94**, 184428 (2016).

[50] N. Sivadas et al., “Magnetic ground state of semiconducting transition-metal trichalcogenide monolayers”, Physical Review B **91**, 235425 (2015).

[51] W.-B. Zhang et al., “Robust intrinsic ferromagnetism and half semiconductivity in stable two-dimensional single-layer chromium trihalides”, Journal of Materials Chemistry C **3**, 12457–12468 (2015).

[52] S. Lebègue et al., “Two-dimensional materials from data filtering and ab initio calculations”, Physical Review X **3**, 031002 (2013).

[53] X. Li et al., “Coupling the valley degree of freedom to antiferromagnetic order”, Proceedings of the National Academy of Sciences of the United States of America **110**, 3738–3742 (2013).

[54] B. Huang et al., “Layer-dependent ferromagnetism in a van der waals crystal down to the monolayer limit”, Nature **546**, 270–273 (2017).

[55] C. Gong et al., “Discovery of intrinsic ferromagnetism in two-dimensional van der waals crystals”, Nature **546**, 265–269 (2017).

[56]W. Chen et al., “Direct observation of van der waals stacking-dependent interlayer magnetism”, Science (New York, N.Y.) **366**, 983–987 (2019).

[57]Shawulienu Kezilebieke et al., “Topological superconductivity in a van der waals heterostructure”, Nature **588**, 424–428 (2020).

[58]B. Huang et al., “Electrical control of 2d magnetism in bilayer cri3”, Nature nanotechnology **13**, 544–548 (2018).

[59]M. Bonilla et al., “Strong room-temperature ferromagnetism in vse2 monolayers on van der waals substrates”, Nature nanotechnology **13**, 289–293 (2018).

[60]M. Kan et al., “The intrinsic ferromagnetism in a mno2 monolayer”, The journal of physical chemistry letters **4**, 3382–3386 (2013).

[61]D. J. O’Hara et al., “Room temperature intrinsic ferromagnetism in epitaxial manganese selenide films in the monolayer limit”, Nano letters **18**, 3125–3131 (2018).

[62]X. Wang et al., “Raman spectroscopy of atomically thin two-dimensional magnetic iron phosphorus trisulfide (feps 3) crystals”, 2D Materials **3**, 031009 (2016).

[63]H. Liu et al., “Vapor deposition of magnetic van der waals nii2 crystals”, ACS nano **14**, 10544–10551 (2020).

[64]M. Mushtaq et al., “Nix 2 (x= cl and br) sheets as promising spin materials: a first-principles study”, RSC advances **7**, 22541–22547 (2017).

[65]M. Lu et al., “Mechanical, Electronic, and Magnetic Properties of NiX2 (X = Cl, Br, I) Layers”, ACS omega **4**, 5714–5721 (2019).

[66]S. Kezilebieke et al., “Topological superconductivity in a van der waals heterostructure”, Nature **588**, 424–428 (2020).

[67]M. A. McGuire, “Crystal and magnetic structures in layered, transition metal dihalides and trihalides”, Crystals **7**, 121 (2017).

[68]H. Bergeron et al., “Polymorphism in post-dichalcogenide two-dimensional materials”, Chemical Reviews **121**, 2713–2775 (2021).

[69]S. Smoes et al., “Thermodynamic study of the vaporization of europium monosulfide by knudsen-cell mass spectrometry atomization energies of eus(g), eu2s(g), eus2(g), eu2o(g), eu2o2(g), eu2os(g), and eu2s2(g)”, The Journal of Chemical Thermodynamics **9**, 275–292 (1977).

[70]C. Chen et al., “Epitaxy in thin films of eus”, Journal of Applied Physics **36**, 669–670 (1965).

[71]K. Reichelt et al., “Epitaxial growth of high-vacuum evaporated eus on mica”, Journal of Applied Physics **44**, 4242–4242 (1973).

[72]M. Mirabal-Garcia et al., “Magneto-optical studies of epitaxial eus films on silicon”, Journal of Magnetism and Magnetic Materials **28**, 313–318 (1982).

[73]B. Saftić et al., “Molecular beam epitaxy and magnetic properties of eus films on silicon”, Journal of Magnetism and Magnetic Materials **28**, 305–312 (1982).

[74] W. Zinn et al., “Eus ferromagnetic semiconductor films grown epitaxially on silicon”, Journal of Magnetism and Magnetic Materials **35**, 329–336 (1983).

[75] C. Smits et al., “Magnetic and structural properties of eus for magnetic tunnel junction barriers”, Journal of applied Physics **95**, 7405–7407 (2004).

[76] S. Senba et al., “Characterization of epitaxial eus (111) thin films on baf 2 (111) and srf 2 (111) substrates grown by molecular beam epitaxy”, Journal of the Korean Physical Society **62**, 2109–2112 (2013).

[77] A. Goschew et al., “Epitaxial growth of eus on inas (100) and inp (100)”, Thin Solid Films **625**, 106–110 (2017).

[78] S. Vaitiekėnas et al., “Zero-bias peaks at zero magnetic field in ferromagnetic hybrid nanowires”, Nature Physics **17**, 43–47 (2021).

[79] C. Kendrick et al., “Bias-dependent imaging of the in-terminated inas (001)(4× 2) c (8× 2) surface by stm: reconstruction and transitional defect”, Physical Review B **54**, 17877 (1996).

[80] P. Tischer, “Ferromagnetic domains in eus investigated by low-temperature lorentz microscopy”, IEEE Transactions on Magnetics **9**, 9–12 (1973).

[81] A. Mariscal et al., “Highly oriented euo nanocrystalline films via reduction process-nir optical response”, arXiv preprint arXiv:1706.08291 (2017).

[82] M. Yagoub et al., “The effects of eu-concentrations on the luminescent properties of srf2:eu nanophosphor”, Journal of Luminescence **156**, 150–156 (2014).

[83] J.-S. Kang et al., “Observation of mediated cascade energy transfer in europium-doped zno nanowalls by 1,10-phenanthroline”, The Journal of Physical Chemistry C **119**, 2142–2147 (2015).

[84] A. H. Reshak et al., “Exploration of the electronic structure of monoclinic -eu2(moo4)3: dft-based study and x-ray photoelectron spectroscopy”, The Journal of Physical Chemistry C **120**, 10559–10568 (2016).

[85] *X-ray photoelectron spectroscopy (xps) reference pages.*

[86] G.-X. Miao et al., “Controlling magnetic switching properties of eus for constructing double spin filter magnetic tunnel junctions”, Applied Physics Letters **94**, 182504 (2009).

[87] F. S. Bergeret et al., “Odd triplet superconductivity in superconductor–ferromagnet hybrid structures”, Comptes Rendus Physique **7**, 128–135 (2006).

[88] J. S. Moodera et al., “Exchange-induced spin polarization of conduction electrons in paramagnetic metals”, Phys. Rev. B **40**, 11980–11982 (1989).

[89] J. S. Moodera et al., “Frontiers in spin-polarized tunneling”, Physics Today **63**, 46–51 (2010).

[90] R. Meservey et al., “Magnetic field splitting of the quasiparticle states in superconducting aluminum films”, Phys. Rev. Lett. **25**, 1270–1272 (1970).

[91] X. Hao et al., “Spin-filter effect of ferromagnetic europium sulfide tunnel barriers”, Phys. Rev. B **42**, 8235–8243 (1990).

[92]G. De Simoni et al., "Toward the absolute spin-valve effect in superconducting tunnel junctions", Nano Letters **18**, PMID: 30248266, 6369–6374 (2018).

[93]P. M. Tedrow et al., "Spin-polarized electron tunneling study of an artificially layered superconductor with internal magnetic field: euo-al", Phys. Rev. Lett. **56**, 1746–1749 (1986).

[94]Y. M. Xiong et al., "Spin-resolved tunneling studies of the exchange field in EuS/Al bilayers", Phys. Rev. Lett. **106**, 247001 (2011).

[95]M. J. Wolf et al., "Spin-polarized quasiparticle transport in exchange-split superconducting aluminum on europium sulfide", Phys. Rev. B **90**, 144509 (2014).

[96]T. A. Palomaki et al., "Initializing the flux state of multiwell inductively isolated josephson junction qubits", Phys. Rev. B **73**, 014520 (2006).

[97]R. W. Simmonds et al., "Decoherence in josephson phase qubits from junction resonators", Phys. Rev. Lett. **93**, 077003 (2004).

[98]A. Ozaeta et al., "Predicted very large thermoelectric effect in ferromagnet-superconductor junctions in the presence of a spin-splitting magnetic field", Phys. Rev. Lett. **112**, 057001 (2014).

[99]T. Dao et al., "Infrared Perfect Absorbers Fabricated by Colloidal Mask Etching of Al Al 2 O 3 Al Trilayers", ACS Photonics **2**, 964–970 (2015).

[100]I. Elenskiy et al., "Fabrication and properties of josephson junction cantilevers for terahertz applications", IEEE Transactions on Applied Superconductivity **29**, 1–5 (2019).

[101]V. V. Ryazanov et al., "Magnetic josephson junction technology for digital and memory applications", Physics Procedia **36**, SUPERCONDUCTIVITY CENTENNIAL Conference 2011, 35–41 (2012).

[102]K. Tsunekawa et al., "Giant tunneling magnetoresistance effect in low-resistance cofebmgo(001)cofeb magnetic tunnel junctions for read-head applications", Applied Physics Letters **87**, 072503 (2005).

[103]S. Ikeda et al., "Magnetic tunnel junctions for spintronic memories and beyond", IEEE Transactions on Electron Devices **54**, 991–1002 (2007).

[104]T. Dao et al., "Infrared Perfect Absorbers Fabricated by Colloidal Mask Etching of Al Al 2 O 3 Al Trilayers", ACS Photonics **2**, 964–970 (2015).

[105]W. Kang et al., "Spintronic logic design methodology based on spin hall effect–driven magnetic tunnel junctions", Journal of Physics D: Applied Physics **49**, 065008 (2016).

[106]P. Tyagi et al., "Large resistance change on magnetic tunnel junction based molecular spintronics devices", Journal of Magnetism and Magnetic Materials **453**, 186–192 (2018).

[107]B. R. Strohmeier, "An ESCA Method for Determining the Oxide Thickness on Aluminum Alloys", Surface and Interface Analysis **15**, 51–56 (1990).

[108]R. S. Timsit et al., "Structure of the al/al2o3 interface", Applied Physics Letters **46**, 830–832 (1985).

[109] J. Toofan et al., "The termination of the -al2o3 (0001) surface: a leed crystallography determination", Surface Science **401**, 162–172 (1998).

[110] D. L. U. Medlin et al., "Orientation relationships in heteroepitaxial aluminum films on sapphire", Thin Solid Films **299**, 110–114 (1997).

[111] Y. Ando et al., "Growth mechanism of thin insulating layer in ferromagnetic tunnel junctions prepared using various oxidation methods", Journal of Physics D: Applied Physics **35**, 2415 (2002).

[112] W. H. Rippard et al., "Ultrathin Aluminum Oxide Tunnel Barriers", Physical Review Letters **88**, `10.1103/PhysRevLett.88.046805` (2002).

[113] L. Zeng et al., "Atomic structure and oxygen deficiency of the ultrathin aluminium oxide barrier in Al / AlO x / Al Josephson junctions", Science Reports **6**, `10.1038/srep29679` (2016).

[114] L. J. Zeng et al., "Direct observation of the thickness distribution of ultra thin AlOxbarriers in al/AlOx/al josephson junctions", Journal of Physics D: Applied Physics **48**, 395308 (2015).

[115] H. Jung et al., "Potential barrier modification and interface states formation in metal-oxide-metal tunnel junctions", Phys. Rev. B **80**, 125413 (2009).

[116] S. Dandan et al., "Character and fabrication of Al / Al 2 O 3 / Al tunnel junctions for qubit application", Chinese Science Bulletin **57**, 409–412 (2012).

[117] S. Fritz et al., "Correlating the nanostructure of Al-oxide with deposition conditions and dielectric contributions of two- level systems in perspective of superconducting quantum circuits", Science Reports **8**, `10.1038/s41598-018-26066-4` (2018).

[118] T. Greibe et al., "Are "pinholes" the cause of excess current in superconducting tunnel junctions? a study of andreev current in highly resistive junctions", Phys. Rev. Lett. **106**, 097001 (2011).

[119] N. Alimardani et al., "Impact of electrode roughness on metal-insulator-metal tunnel diodes with atomic layer deposited Al2O3 tunnel barriers", Journal of Vacuum Science & Technology A **30**, `10.1116/1.3658380` (2012).

[120] H. Kohlstedt et al., "The role of surface roughness in the fabrication of stacked nb/al–alox/nb tunnel junctions", Journal of Applied Physics **80**, 5512–5514 (1996).

[121] T.-s. Shih et al., "Thermally-Formed Oxide on Aluminum and Magnesium", Materials Today **47**, 1347–1353 (2006).

[122] J. D. Baran et al., "Mechanism for limiting thickness of thin oxide films on aluminum", Phys. Rev. Lett. **112**, 146103 (2014).

[123] A. E. T. Kuiper et al., "Plasma oxidation of thin aluminum layers for magnetic spin-tunnel junctions", Journal of Applied Physics **89**, 1965–1972 (2001).

[124] J. Wilt et al., "In situ atomic layer deposition and electron tunneling characterization of monolayer al2o3 on fe for magnetic tunnel junctions", AIP Advances **8**, 125218 (2018).

[125] M. Leskelä et al., “Atomic layer deposition (ALD) : from precursors to thin film structures”, Thin Solid Films **409**, 138–146 (2002).

[126] D. V. Szabó et al., “Microwave Plasma Synthesis of Materials—From Physics and Chemistry to Nanoparticles: A Materials Scientist’s Viewpoint”, Inorganics **2**, 468–507 (2014).

[127] G. P. Gakis et al., “Investigation of the initial deposition steps and the interfacial layer of atomic layer deposited (ald) al2o3 on si”, Applied Surface Science **492**, 245–254 (2019).

[128] E. Tan et al., “Oxygen stoichiometry and instability in aluminum oxide tunnel barrier layers”, Physical Review B **71**, 161401 (2005).

[129] J.-C. Dupin et al., “Systematic xps studies of metal oxides, hydroxides and peroxides”, Phys. Chem. Chem. Phys. **2**, 1319–1324 (2000).

[130] D. R. Baer et al., “Xps guide: charge neutralization and binding energy referencing for insulating samples”, Journal of Vacuum Science & Technology A: Vacuum, Surfaces, and Films **38**, 031204 (2020).

[131] S. Tanuma et al., “Proposed Formula for Electron Inelastic Mean Free Paths based on Calculations for 31 Materials”, Surface Science Letters **192**, 849–857 (1987).

[132] N. F. M. N. Cabrera, “Theory of the oxidation of metals”, Reports on Progress in Physics **12(1)**, 163–184 (1949).

[133] J. G. Simmons, “Generalized Thermal JV Characteristic for the Electric Tunnel Effect”, Journal of Applied Physics **35**, `10.1063/1.1713820` (1964).

[134] J. G. Simmons, “Generalized formula for the electric tunnel effect between similar electrodes separated by a thin insulating film”, Journal of applied physics **34**, 1793–1803 (1963).

[135] T. E. Hartman et al., “Electron tunneling through thin aluminum oxide films”, Physical Review **134**, A1094 (1964).

[136] V. Da Costa et al., “Tunneling phenomena as a probe to investigate atomic scale fluctuations in metal/oxide/metal magnetic tunnel junctions”, Physical review letters **85**, 876 (2000).

[137] T. Aref et al., “Characterization of aluminum oxide tunnel barriers by combining transport measurements and transmission electron microscopy imaging”, Journal of Applied Physics **116**, 073702 (2014).

[138] E. Luo et al., “Tunneling current and thickness inhomogeneities of ultrathin aluminum oxide films in magnetic tunneling junctions”, Journal of Applied Physics **90**, 5202–5207 (2001).

[139] J. C. Lee et al., “Modeling and characterization of gate oxide reliability”, IEEE Transactions on Electron Devices **35**, 2268–2278 (1988).

[140] E. J. Patiño et al., “Experimental determination of tunneling characteristics and dwell times from temperature dependence of Al/Al2O3/Al junctions”, Applied Physics Letters **107**, `10.1063/1.4938209` (2015).

[141]S. Mitani et al., “Fe/mgo/feco (100) epitaxial magnetic tunnel junctions prepared by using in situ plasma oxidation”, Journal of Applied Physics **93**, 8041–8043 (2003).

[142]P. De Gennes, “Coupling between ferromagnets through a superconducting layer”, Physics Letters **23**, 10–11 (1966).

[143]B. Li et al., “Superconducting spin switch with infinite magnetoresistance induced by an internal exchange field”, Phys. Rev. Lett. **110**, 097001 (2013).

[144]T. C. Rödel et al., “High-density two-dimensional electron system induced by oxygen vacancies in zno”, Phys. Rev. Mater. **2**, 051601 (2018).

[145]P. F. Smet et al., “Blue electroluminescence from multilayered bas:eu/al2s3 thin films”, Journal of Applied Physics **95**, 184–190 (2004).

[146]A. Hijano et al., “Coexistence of superconductivity and spin-splitting fields in superconductor/ferromagnetic insulator bilayers of arbitrary thickness”, Phys. Rev. Research **3**, 023131 (2021).

[147]E. Strambini et al., “Superconducting spintronic tunnel diode”, Nature Communications **13**, `10.1038/s41467-022-29990-2` (2022).

[148]J. S. Moodera et al., “Electron-spin polarization in tunnel junctions in zero applied field with ferromagnetic eus barriers”, Phys. Rev. Lett. **61**, 637–640 (1988).

[149]J. S. Moodera et al., “Variation of the electron-spin polarization in euse tunnel junctions from zero to near 100% in a magnetic field”, Phys. Rev. Lett. **70**, 853–856 (1993).

[150]T. S. Santos et al., “Observation of spin filtering with a ferromagnetic EuO tunnel barrier”, Phys. Rev. B **69**, 241203 (2004).

[151]G.-X. Miao et al., “Magnetoresistance in double spin filter tunnel junctions with nonmagnetic electrodes and its unconventional bias dependence”, Phys. Rev. Lett. **102**, 076601 (2009).

[152]M. Müller et al., “Exchange splitting and bias-dependent transport in euo spin filter tunnel barriers”, Europhysics Letters **88**, 47006 (2009).

[153]A. Thomas et al., “Evidence for positive spin polarization in co with srtio3 barriers”, Journal of Applied Physics **97**, 10C908 (2005).

[154]B. Li et al., “Observation of tunnel magnetoresistance in a superconducting junction with zeeman-split energy bands”, Physical Review B **88**, 161105 (2013).

[155]F. MadarakaMwema et al., “Effect of substrate temperature on aluminium thin films prepared byrf-magnetron sputtering”, Materials Today: Proceedings **5**, 20464–20473 (2018).

[156]D.-Y. Moon et al., “Effects of the substrate temperature on the cu seed layer formed using atomic layer deposition”, Thin Solid Films **519**, 3636–3640 (2011).

[157]Z. Geng et al., “Superconductor-ferromagnet hybrids for non-reciprocal electronics and detectors”, arXiv preprint arXiv:2302.12732 (2023).

[158]K. Ono et al., “Current rectification by pauli exclusion in a weakly coupled double quantum dot system”, Science **297**, 1313–1317 (2002).

[159]L. DiCarlo et al., “Photocurrent, rectification, and magnetic field symmetry of induced current through quantum dots”, Physical review letters **91**, 246804 (2003).

[160]F. Giazotto et al., “Ferromagnetic-insulator-based superconducting junctions as sensitive electron thermometers”, Physical Review Applied **4**, 044016 (2015).

[161]S. J. v. d. der Molen et al., “Visions for a molecular future”, Nature nanotechnology **8**, 385–389 (2013).

[162]M. Cinchetti et al., “Determination of spin injection and transport in a ferromagnet/organic semiconductor heterojunction by two-photon photoemission”, Nature materials **8**, 115–119 (2009).

[163]C. Wäckerlin et al., “Strong antiferromagnetic exchange between manganese phthalocyanine and ferromagnetic europium oxide”, Chemical Communications **51**, 12958–12961 (2015).

[164]A. Filip et al., “Spin-injection device based on eus magnetic tunnel barriers”, Applied physics letters **81**, 1815–1817 (2002).

[165]E. Coronado et al., *Molecular magnetism: from molecular assemblies to the devices*, Vol. 321 (Springer Science & Business Media, 2013).

[166]S. Stepanow et al., “Spin tuning of electron-doped metal–phthalocyanine layers”, Journal of the American Chemical Society **136**, PMID: 24635343, 5451–5459 (2014).

[167]M. Inoue et al., “Spin pumping into superconductors: a new probe of spin dynamics in a superconducting thin film”, Physical Review B **96**, 024414 (2017).

[168]Y. Yao et al., “Probe of spin dynamics in superconducting nbn thin films via spin pumping”, Physical Review B **97**, 224414 (2018).

[169]Y. Tserkovnyak et al., “Enhanced gilbert damping in thin ferromagnetic films”, Physical review letters **88**, 117601 (2002).

[170]H. Matsuki, “Electrical switching by spin-orbit torque - a study of ferromagnetic resonance of eus–nb thin film bilayers towards superconducting spintronics”, MA thesis (University of Cambridge, 2019).

[171]M. X. Aguilar-Pujol et al., *Magnon currents excited by the spin seebeck effect in ferromagnetic eus thin films*, 2023.

[172]A. Brataas et al., “Spin insulatronics”, Physics Reports **885**, 1–27 (2020).

[173]J. M. Gomez-Perez et al., “Strong interfacial exchange field in a heavy metal/ferromagnetic insulator system determined by spin hall magnetoresistance”, Nano Letters **20**, 6815–6823 (2020).

[174]M. C. Biesinger et al., “The role of the auger parameter in xps studies of nickel metal, halides and oxides”, Physical Chemistry Chemical Physics **14**, 2434–2442 (2012).

[175]J. R. McCreary et al., “Heat and entropy of sublimation of nickel dichloride, dibromide, and di-iodide; dissociation energies of gaseous nicl2 and nibr2”, The Journal of Chemical Physics **48**, 3290–3297 (1968).

[176]J. Björk et al., “Mechanisms of halogen-based covalent self-assembly on metal surfaces”, Journal of the American Chemical Society **135**, PMID: 23506285, 5768–5775 (2013).

[177]B. Andryushechkin et al., “Adsorption of halogens on metal surfaces”, Surface Science Reports **73**, 83–115 (2018).

[178]N. Merino-Díez et al., “Hierarchy in the halogen activation during surface-promoted ullmann coupling”, ChemPhysChem **20**, 2305–2310 (2019).

[179]M. Mushtaq et al., “Nix 2 (x= cl and br) sheets as promising spin materials: a first-principles study”, RSC advances **7**, 22541–22547 (2017).

[180]A. Soumyanarayanan et al., “Quantum phase transition from triangular to stripe charge order in NbSe2”, Proceedings of the National Academy of Sciences **110**, 1623–1627 (2013).

[181]M. M. Ugeda et al., “Characterization of collective ground states in single-layer NbSe2”, Nature Physics **12**, 92–97 (2016).

[182]S. Kezilebieke et al., “Electronic and magnetic characterization of epitaxial crbr3 monolayers on a superconducting substrate”, Advanced Materials **33**, 2006850 (2021).

[183]R. C. O’Handley, *Modern magnetic materials: principles and applications* (Wiley, 2000).

[184]B. K. Rai et al., “Influence of cobalt substitution on the magnetism of nibr 2”, Physical Review Materials **3**, 034005 (2019).

[185]N. J. Darton et al., *Magnetic nanoparticles in biosensing and medicine* (Cambridge University Press, 2019).

[186]A. Arrott, “Criterion for ferromagnetism from observations of magnetic isotherms”, Physical Review **108**, 1394 (1957).

[187]A. Bedoya-Pinto et al., “Intrinsic 2d-xy ferromagnetism in a van der waals monolayer”, Science **374**, 616–620 (2021).

[188]A. Arrott et al., “Approximate equation of state for nickel near its critical temperature”, Physical Review Letters **19**, 786 (1967).

[189]S. Hadjadj et al., “Epitaxial monolayers of magnetic 2d semiconductor febr2 grown on au (111)”, arXiv preprint arXiv:2304.11972 (2023).

[190]T. T. Angeloni, “Non-reciprocal supercurrent induced by a van der waals semiconductor”, MA thesis (Scuola Normale Superiore Pisa, 2022).

[191]D. Bikaljević et al., “Noncollinear magnetic order in two-dimensional nibr2 films grown on au (111)”, ACS nano **15**, 14985–14995 (2021).